VRIJE UNIVERSITEIT AMSTERDAM
IN COLLABORATION WITH AMOLF
AND IMPERIAL COLLEGE LONDON

MASTER THESIS

Factors impacting the Kramers-Kronig compliance of impedance spectra from perovskite solar cells and the influence on equivalent circuit modelling

---

Author:
Mischa Benjamin HILLENIUS BSc.

Supervisor:
Dr. Elizabeth VON HAUFF
Second supervisor:
Dr. Bruno Ehrler

A thesis submitted in fulfillment of the requirements for the degree of Master of Science (MSc)

in the

Hybrid Solar Energy Conversion Group
Vrije Universiteit Amsterdam

and

Hybrid Solar Cells
AMOLF

November 10, 2020

"What you give attention grows."
"Think in solutions, not in problems."

My parents

"Work with what is instead of what is not."

Edwin Selij

"Keep your eye on the prize"

Sportteacher Etmo Smith

VRIJE UNIVERSITEIT AMSTERDAM
IN COLLABORATION WITH AMOLF
AND IMPERIAL COLLEGE LONDON

Abstract

Faculteit der Bètawetenschappen (VU)
Faculteit der Natuurwetenschappen, Wiskunde en Informatica (UvA)

Master of Science (MSc)

Factors impacting the Kramers-Kronig compliance of impedance spectra from perovskite solar cells and the influence on equivalent circuit modelling

by Mischa Benjamin HILLENIUS BSc.

Perovskite solar cells are a novel type promising high Power Conversion Efficiency (PCE) combined with low manufacturing cost. Perovskite solar cells (PSC's) show time-dependent electrical properties leading to hysteresis in the current-voltage characteristics. This results in dependence of the device performance on previous exposure to external stress factors, resulting in temporary or irreversible changes in performance. In-situ characterisation of the device during operation can be done by Impedance Spectroscopy (IS), to probe transient processes in the solar cell. IS data needs to be validated by testing the self-consistency, which is hardly ever done in the field of IS on perovskite solar cells. In this research, IS data on pure $MaPbI_3$ solar cells and mixed cation solar cells $Ma_{0.95}Ga_{0.05}PbI_3$ and $Ma_{0.95}Fa_{0.05}PbI_3$ is validated by the Linear Kramers-Kronig test (Lin-KK) for fast assessment of spectra. Factors which may influence KK-(in)compliance were investigated. The KK-compliant spectra are modelled with Equivalent Circuit Modelling (ECM) to extract device parameters relating to transient processes present in the solar cell under operating conditions. It is found that most IS data in this research is KK-incompliant and not fit for ECM. Factors influencing KK-(in)compliance were found to be sample dependent. The data suggests KK-(in)compliance is independent from DC bias voltage and dependent on illumination and frequency range looked at. It is demonstrated that KK-incompliant spectra can in some cases be fit with ECM, leading to unreliable or faulty device parameters. This research demonstrates the usefulness of the Lin-KK test to extract information about transient processes from IS on PSC during operation.

Acknowledgements

Thank you, Dr. Elizabeth von Hauff for guiding me through this project. Your help to conduct research, to do data analysis and to write the thesis was indispensable. The open communication we had I see as enormously helpful and I was glad we had this type of supervisor-student relationship. It meant a lot to me. Thank you Prof. Dr. Bruno Ehrler for your guidance at AMOLF, for devising plans for sample fabrication and for your role as second supervisor. Many thanks to Dr. Moritz Futscher from AMOLF, who taught me to do lab work and to be a critical scientist. Asking - and daring to ask - the right questions in science and in life is extremely important and a valuable skill. Then I would like to thank Dr. Thomas Macdonald and Mr. Richard Pacalaj from Imperial College London for extensive (experimental) collaboration. It was a pleasure. Both of you showed you were available and there for me if I was stuck in the research, and made me feel welcome to ask questions. This did wonders to my moral. Thanks to the technicians Martin Slaman at the VU and Mark Duursma at AMOLF for working on custom-made material for the project. A collaboration project between the VU and AMOLF will now be easier in the future. Also I would like to express my gratitude to PhD student Lucie McGovern who worked with me in the lab and made samples for the project as well. Thanks to Dr. Raoul Frese and Mw. Drs. Anja Zoomer for their support on the process. Lastly, I would like to express my gratitude towards Science Park for being a second home to me for many many years and the bouldergym (and sauna!) at the University Sportcenter (USC) for keeping me sane and healthy. You are accommodating a wonderful community.

On a personal note I would like to thank all the members from the Hybrid Solar Energy Conversion Group at the VU, and especially Laura Schleeper, Alba Fonseca Topp, Ivo Jak, Rhea Lambregts, Luuk Wagenaar, David Schreuder and Lotte Tjin-a Cheong. We shared wonderful times in our office. Special thanks to Laura and Alba with whom I shared many coffees and had productive working hours. Thanks to Mees Dieperink, with whom, apart from my supervisor, I could talk about my specific research area. At AMOLF I would like to thank Weiyi Ding and Loreta Muscarella, both of whom are spirited people. Many thanks to Hania Kaufmann from the thesis support group and all the members, you played a huge role during this thesis time. Special thanks to Eli de Smet and Fokel Ellen. You brought Student Meditation in my life, with countless new friends, sustained productivity during the Corona lockdown with Deep Work, and meditation courses. Especially the Metta course was important for me personally to cultivate gratefulness and to cultivate more kindness towards myself and others. MAY YOU BE HAPPY!!

Lastly I would like to express my gratitude to the people most important to me. My housemates Sophie van der Woerdt, Cor Neefjes and Zazo Meijs who are simply the best. You were - and are - always there for me through my best and my most difficult times with hugs, conversations or coffee. Special thanks to Renate de Kok for your support and your trust in me. You are a free spirit and an amazing person. I would like to thank Dominique van Poorten, Danni Wiebes and Rien Vanneste for being true friends who I can ask for help when I need it most. That means more to me than I can say. Lastly I want to thank my family. Ruben Hillenius, Thimo Hillenius, Rennie Minzinga-Zijlstra, Ginny, and Eppo and Leny Hillenius. You are all incredibly important to me. I feel very grateful to have chosen you as my family.

Samenvatting

Perovskiet is een kristalstructuur met speciale elektrische en optische eigenschappen. Dit maakt het materiaal geschikt voor toepassing in transparante en buigzame zonnepanelen, sensors of LEDs. Dit onderzoek richt zich op het verkrijgen van betrouwbare data om de interne processen in een zonnecel gemaakt van perovskiet materiaal te begrijpen, zodat de stabiliteit en levensduur van de zonnecellen vergroot kan worden.

Zonnecellen van perovskiet materiaal gaan makkelijk kapot. Dit komt onder andere doordat ionen in de kristalstructuur kunnen bewegen onder invloed van licht en lading. Aan de contact grensvlakken hopen de ionen zich op, waardoor ze het functioneren van het zonnepaneel kunnen beinvloeden (hysterese) en chemische reacties kunnen induceren.

De interne processen worden onderzocht met impedantie spectroscopie. Hierbij wordt een kleine wisselstroom door het sample gestuurd. De frequentie van het wisselstroom signaal wordt gevarieerd, waardoor elektrische en ionische processen die op een bepaalde tijdsschaal werken beurtelings worden geactiveerd. Met een 'equivalent circuit model' kunnen daar fysische parameters uit worden verkregen. Impedantie spectra moeten worden gevalideerd door toepassing van de Kramers-Kronig (KK) relaties. In het onderzoeksveld van perovskiet zonnepanelen wordt dit niet of nauwelijks gedaan, waardoor mogelijk veel onderzoeken onbetrouwbare data gebruiken. De Kramers-Kronig relaties zijn een mathematische beschrijving voor hoe twee complentaire delen van de meting bij elkaar horen. De test checkt of de twee complementaire delen die gemeten zijn inderdaad complementair zijn. Dit wordt weergegeven in residuele (procentuele) afwijkingen per frequentie. Bij een systematische afwijking in de residuen is de meting niet betrouwbaar.

Bijna alle metingen aan zonnecellen met bewezen stabiele prestaties bleken niet Kramers-Kronig compatibel (compliant) te zijn. Factoren die invloed hadden op (in)compatibiliteit waren licht en de specifieke frequentie regio waarnaar gekeken werd. Blootstelling aan gelijkstroom voltage bleek geen invloed te hebben op (in)compatibiliteit. Gezien de meetresultaten zowel numeriek als in (in)compatibiliteit niet in voldoende mate gereproduceerd konden worden, moet er gewerkt worden aan een zeer gedetailleerd protocol voor fabricatie en metingen. Met betrouwbare data kan analyse leiden tot meer begrip van de fundamentele processen in de zonnecel die leiden tot instabiliteit, en kan op termijn de levensduur van perovskiet zonnepanelen verlengd worden.

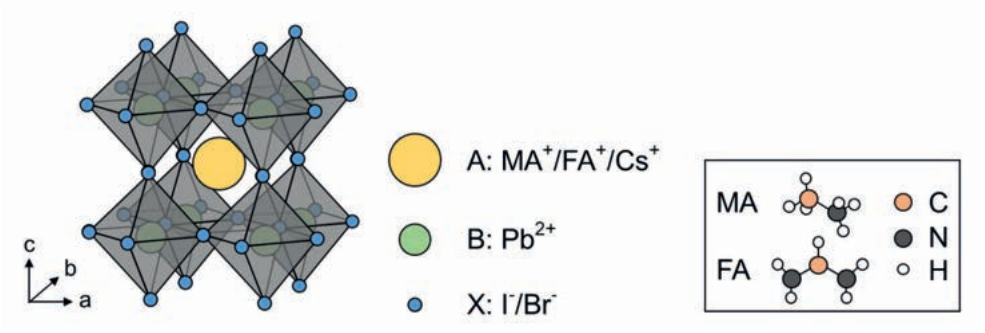

FIGURE 1: **Schematische illustratie van de perovskiet kristalstructuur ABX_3.** De ionen op de A en X positie kunnen door het materiaal migreren en de prestatie en levensduur van de zonnecel beinvloeden. Rechts staan de structuurformules van twee gangbare (organische) moleculen voor de A-positie in de kristalstructuur afgebeeld. Uit: [1].

Contents

Dedicated to Icarus

the inner compass

and

dedicated to dissolving the mind in the body

Chapter 1

Introduction

Since the beginning of the industrial revolution, CO_2 and methane levels are increasing steadily in Earth's atmosphere [2, 3]. This is due to the production, transport and burning of gas, coal and oil [4]. The global warming that is a result of this threatens biodiversity, ecosystems and human society through climate change, increase of droughts, wildfires, floods and food security [5, 6, 7]. The effects of global warming are already noticeable in the recent large scale wildfires in Australia and the increases in frequency of heat waves across the globe [8]. Human society is still largely dependent on fossil fuels to power civilisation, with only 4% constituting renewable energy [9], though the adverse effects of burning fossil fuels affect the planet as whole. To ensure a less carbon-intensive society, sustainable energy technologies need to be developed and implemented.

Solar irradiance strikes the earth's surface in abundance. The theoretical potential of solar energy represents more energy reaching the earth's surface in one and a half hours than global energy consumption in 2001 from all sources combined [10]. Solar energy, in the form of solar electricity, solar thermal and solar fuel, hold together with wind the highest extractable and technical potentials for sustainable energy harvesting [10, 11, 12]. Solar electricity, captured using solar cells, can be employed on both small and large scale and can be developed further to help meet global energy demand.

Perovskite solar cells (PSCs) are a novel type belonging to third generation (emerging) photovoltaics [13]. They combine high Power Conversion Efficiency (PCE) of > 25% [14] with low production cost due to solution-processing [15], low reaction temperatures and cheap precursors. They have a tunable bandgap depending on chemical composition [16]. Furthermore, they are semi-transparent and flexible, leading to extended possibilities for application on bend surfaces or in architecture [17]. Their tunable and semi-transparent nature allows for application as top cell in tandem solar cell constructions, combining PSCs with existing mature Photovoltaic (PV) technologies to achieve efficiencies beyond the Shockley-Queisser limit of a single-junction solar cell [18].

Challenges for commercialisation of PSCs remain, though progress has been made. Limited stability of PSCs due to ion migration [19] and photo- and humidity induced degradation processes [20, 21] has hampered commercialisation due to short cell lifetimes, as have difficulties in upscaling. Small area research cells obtained efficiencies of 25.2%, whereas Pervoskite Solar Modules (PSMs) with large areas reach 16.1% efficiency [22]. Lifetime of PSMs on average is currently in the 500-1000h regime (approximately 0.5-1 year). In some cases, lifetimes of 10,000 hours (approximately 10 years) under 1 sun illumination were reached. Average lifetimes of 10 years of PSCs could thus be expected in the near future. Silicon solar cells have a lifetime of 25 years. However, for PSCs/PSMs to be competitive, this lifetime criterium is not as strict due to lower production costs. The levelised cost of eletricity (LCOE) for a PSM with 19% PCE and a 1% reduction in PCE per year, reaches the same LCOE as for traditional silicon solar cells in only 14.7 years, depending on assumptions of local annual irradiance and electricity prices [23]. Lifetime of PSMs should thus be in the 15-20year regime to be price competitive. Other challenges for PSCs include encapsulation and lead-toxicity of the material [24]. Commercialisation

of PSMs is in reach if those issues, including lifetime and stability, are addressed and improved.

However, the physical (and chemical) mechanisms due to which perovskite solar cells degrade are to a large degree still unknown. PSCs show complex electrical behaviour: they exhibit time-dependent electrical properties leading to hysteresis in the current-voltage (JV) characteristics. This results in device performance which is dependent on previous exposure to external stress conditions. Hysteresis is correlated with stability issues and device degradation [25, 26, 27]. Due to hysteresis, reliably extracting main solar cell performance parameters like the *short-circuit current density* J_{sc}, the *open-circuit voltage* V_{oc}, the *fill factor* FF and the *maximum power point* MPP becomes problematic. These parameters are determined from the illuminated JV curves. For PSCs these prove to be dependent on measurement settings, such as light soaking before the measurement, applied bias voltage, voltage scan speed and scan direction [28]. Therefore, standardised testing protocols are necessary to obtain reliable device characteristics. Additionally, transparency in reporting standards and measurement protocols needs to be improved within the PSC community [18]. Besides hysteresis, PSCs exhibit both reversible and irreversible changes in device performance, of which the factors and processes which are beneficial or detrimental to the device performance are still unclear [29]. Understanding the physical mechanisms occurring in PSCs under operating conditions can shine a light on how to increase perovskite stability and lifetime, whilst slowing or diminishing device degradation.

In-situ research on the device level can be done by Impedance Spectroscopy (IS) [30]. An important advantage of impedance spectroscopy is that it allows for electrical measurements during operating conditions. In IS, various time-dependent (transient) processes in the solar cell are probed using an AC electrical perturbation. Transient processes in PSCs include electron/hole transfer, electron/hole transport, (dis)charging of geometrical and contact layer capacitances, recombination, ion migration, ion accumulation and more [31]. These are described in more detail in the theoretical background. As the transient processes operate on a certain time-scale, the processes can be sequentially probed by sweeping the frequency of the AC perturbation signal. The activation and release of a transient process is also known as a *relaxation*. When the processes operate on distinct time-scales, the transient processes can be differentiated. Superimposing the small AC perturbation signal on a DC voltage makes it possible to observe the device behaviour on different points along the JV characteristic of the solar cell. Impedance data can be analysed using Equivalent Circuit Modelling (ECM), in which the data is fit to a model constituting of basic electrical components resembling physical processes in the device [32]. Composing a model a priori that bears physical relevance, so physical relevant parameters can be extracted, has proven to be the biggest challenge in equivalent circuit modelling of PSCs. Unfortunately, the same impedance data can be fit to multiple models, signalling there is no unique solution and multiple models could describe PSCs [33]. Since many of the actual processes happening in PSCs and the extent to which they are happening are still poorly understood, universal equivalent circuit models describing the physics of PSCs are still lacking in literature (though numerous models have been proposed [30, 31, 34, 35]).

IS data needs to be validated before parameters can be extracted with ECM [33]. Validation of impedance data is necessary to ensure the sample response is only due to the applied perturbation signal (*causality*), to ensure the properties of the sample do not irreversibly change during the measurement (*stability*) and to ensure keeping the requirement of IS to obtain a linear (Ohmic) response of the sample due to the perturbation signal during the measurement (*linearity*). Validation should be done in two ways: by performing cross-checks during measurements and by applying the Kramers-Kronig relations using the Linear Kramers-Kronig (Lin-KK) test. Application of the test is more sensitive to the IS-requirements above. The test is 'linear' due to the linearity of the associated fitting problem in which only one parameter (resistance) is fitted instead of two (resistance and time-constants). Fitting of two parameters simultaneously leads to multiple solutions related to local minima of the cost-function of the fitting, and special care

should be taken. The Lin-KK test allows for obtaining valid test results quickly and easily.

Though impedance data validation using the KK-relations was described in detail by Boukamp in 1995 in the *Lin-KK* test [36], and the test has been improved by Schonleber and Klotz in 2014 [37, 38], the perovskite impedance spectroscopy field is slow to adopt this strategy of data validation. Numerous papers have been published on EIS on various compositions of perovskite solar cells [30, 34, 39, 40, 41, 42, 43], but none perform data validation using the KK-relations. Very recently (2019), to the best of my knowledge, the two first papers with KK-compliant IS spectra were published [44, 45]. This shines a critical light on previous results in this field, and might explain in part why the tremendous effort spend on finding an appropriate equivalent circuit model for perovskite solar cells still has not been helpful to the field yet [44].

Therefore the goal of this research is to investigate transient (relaxation) processes using impedance spectroscopy data validated by the Lin-KK test, demonstrating the use of applying the Lin-KK test for reliable extraction of parameters using ECM of PSC impedance data. During the research, factors impacting the KK-compliance will be investigated. IS data on most studied PSC methyl-ammonium (MA) lead iodide ($MaPbI_3$) and mixed cation solar cells $Ma_{0.95}Ga_{0.05}PbI_3$ and $Ma_{0.95}Fa_{0.05}PbI_3$ is validated by the Lin-KK test. Mixed cation $MaPbI_3$ PSCs containing small amounts of the cations Guanidinium (GA), Formamidinium (FA) or Cesium (Cs) prove to reduce iodide ion transport in PSCs and therefore increase the stability [43]. The KK-compliant spectra are modelled with ECM to extract device parameters relating to transient processes present in the solar cell under operating conditions. The research question is:

Which factors impact the KK-compliance of impedance spectra from perovskite solar cells and what is the influence on equivalent circuit modelling

In the theoretical background, the fundamental working principle of a solar cell will be explained, the structure of PSCs will be described and the various transient processes and their interaction will be illustrated. Then the physical and mathematical background to impedance spectroscopy and Kramers-Kronig compliance testing will be posed. The method section will contain experimental setup to investigate transient processes using impedance spectroscopy. In the results section the outcome of the experiments will be presented for four $MaPbI_3$ cells. The discussion will focus on factors influencing KK-(in)compliance and relating them to the specific KK-requirement violated. The impact of fitting KK-incompliant data is discussed, and suggestions for measurement protocols and analysis methods to promote KK-compliance in the data are formulated. Finally, a conclusion on the investigation of the factors influencing the Kramers-Kronig compliance of impedance spectra and the influence on extracting information on transient processes in PSCs using equivalent circuit modelling is given.

Chapter 2

Fundamental concepts: metal halide perovskites

2.1 Metal halide perovskite solar cells

2.1.1 Perovskite absorber materials

The mineral perovskite, $CaTiO_3$, was discovered in 1839 by Gustav Rose and named after mineralogist L.A. Perovski [46]. The name 'perovskite' is now used to describe the structure of the mineral, denoted by ABX_3, where A and B are cations bearing positive charge and X is an anion bearing negative charge. The use of metal-halide perovskites as light harvester (photoactive layer) in emerging photovoltaic technologies is first reported in 2009 [47]. Efficiencies rose from 3.8% in 2009 [13] to a record high 25.2% in 2019 according to NREL [14], which is the steepest learning curve in device efficiency in the history of photovoltaic research.

Figure 2.1 shows the perovskite structure. The A cation in the middle can be organic (Methylammonium (MA), or Formamidinium (FA)), or inorganic (Cesium). The B cation is a divalent metal cation, Pb^{2+} or Sn^{2+} and is smaller than the A cation. The X anion is a halide (Cl, I, Br), and is in octahedron formation around the B cation [48]. Both the A and X positions in the crystal structure can be compposed of a stoichiometric mixture of different constituents, respectively. Most of perovskite solar cells use lead as divalent cation, however effort is spend to replace this by tin due to the toxicity of lead. Tin based perovskite solar cells are now approaching 10% efficiency [49]. The A cation of $MaPbI_3$, Methylammonium, has no contribution to the formation of the energy bands [48], and the band gap is determined mainly by the B cation and X anion forming the octahedra framework [50]. The formation of the valence band originates from the p-orbitals of I, mixed with 6p and 6s orbitals of Pb, corresponding to an absorption transition at 760nm. The formation of the conduction band originates from the σ-antibonding orbitals 6p of

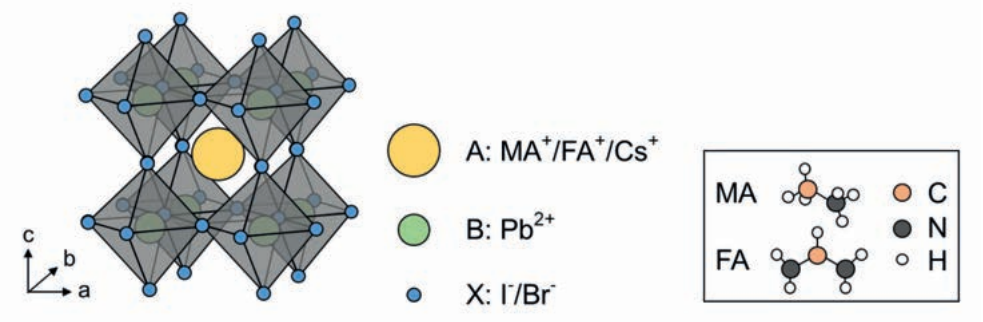

FIGURE 2.1: **Schematic illustration of the perovskite crystal structure ABX_3.** The typical constituents of metal halid perovskites used in optolectronic applications are displayed. Taken from [1].

Pb and 5s of I, and from the π-antibonding orbitals 6p of Pb and 5p of I, corresponding to an absorption transition at 480nm [48].

The bandgap is tunable by varying the chemical constituents of the perovskite using various halides (iodide, bromide, chloride) or cations, with an E_G between 1.5 and 2.5eV (830 - 500nm). Also stability can be increased by varying the chemical constituents. For example, Incorporating a small amount (5%) of the larger A-site cation guanidinium (GA) into $MaPbI_3$, resulting in $Ma_{0.95}Ga_{0.05}PbI_3$, has proven to increase stability [51, 52, 53] by reducing iodide ion transport [43]. Simulations by the same authors indicated that the higher activation energy for iodide ion transport is due to local distortion of the Pb/I cage as a result of the GA mismatch with MA [43]. Also Formamidinium (FA) increases the activation barrier for iodide ion transport. In addition, the activation energy barrier for ion transport for mixed-halide perovskite can be increased as well by compression of the unit cell through incorporation of the smaller cation Cesium into the lattice. Effectively, this prevents phase segregation towards iodide-rich and bromide-rich regions [54]. Iodide-rich regions have a lower band gap, which limits the voltage extractable from the solar cell [55].

Furthermore, the crystal structure of some metal-halide perovskites depends on temperature. From Figure 2.1, it seems that $MaPbI_3$ has a cubic crystal structure. In reality, the crystal structure of perovskite shows phase changes at two distinctive temperatures. $MaPbI_3$ shows a phase change from orthorombic to tetragonal at 162K [56], and a phase change from tetragonal to cubic at 327K [57]. The second phase change, around 327K, happens well within the operative temperature range of a solar cell. This could hinder the application of perovskite in solar cells, considering a phase change could lead to changes in optical properties of the perovskite. However, Quarti et al. showed the absence of dramatic changes in the optical properties of metal halide perovskites across the tetragonal to cubic transition [57]. Generally, perovskite absorber materials are 'defect tolerant' materials, meaning that they are expected to form few structural defects and that the defects that do form have little effect on the lifetime and mobility of charge carriers [58]. More extensive research on various compositions of perovskite is being done to enhance optical properties and stability.

2.1.2 Perovskite solar cells

Solar cells use solar irradiation to generate electric power. Before sunlight reaches the earth, it moves through the atmosphere which absorbs parts of the solar spectrum. The extra-terrestial solar spectrum is called AM0, and the solar irradiance that reaches the earth is called AM1.5g [59]. For quantification and standardisation purposes, all solar cells are tested with a solar simulator having an AM1.5g air mass filter to simulate the solar irradiance at sea level, with light intensity of $100 mW/cm^2$. The solar spectrum AM0 and solar irradiance at sea level AM1.5g are displayed in Figure 2.2.

Perovskite can be used as a light-harvester in solar cells. Since it is an instrinsic semiconductor, it behaves as an insulator for fixed charge and as an conductor for photo-induced charge carriers, excited across the band gap when a photon is absorbed by the perovskite. An excited electron bearing negative charge leaves a hole which bears positive charge. The perovskite material is sandwiched between the electron transport layer (ETL) and the hole transport layer (HTL). The transport layers have different work functions, which causes an electric field across the device (the built-in voltage V_{bi}). This causes the photo-generated charge to drift towards the transport layers, whereas the charges would rely only on diffusion to reach their respective electrode if the V_{bi} would be absent. After the transport layers, charges can be extracted through contacts and provide power. This is the fundamental working principle of a solar cell. The energy band diagram of a perovskite solar cell is in the $p-i-n$ formation, where p is the hole transport layer, i is the perovskite and n is the electron transport layer. The band diagram is shown in Figure 2.3. Take note that, taking band-bending into account, the electrons to be

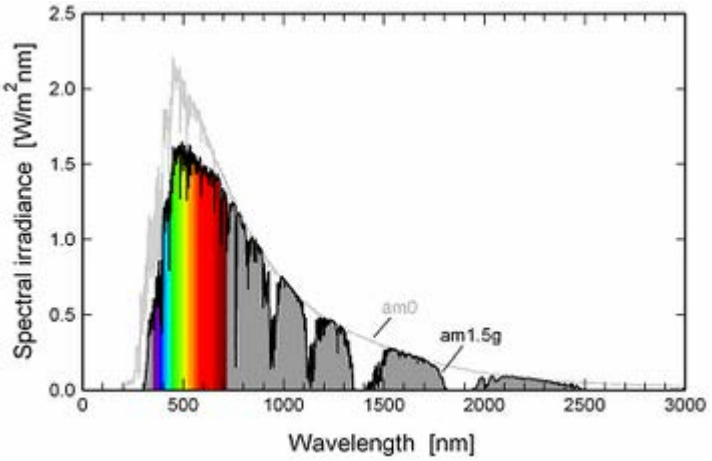

FIGURE 2.2: Spectral irradiance of the AM1.5g spectrum. Taken from [59].

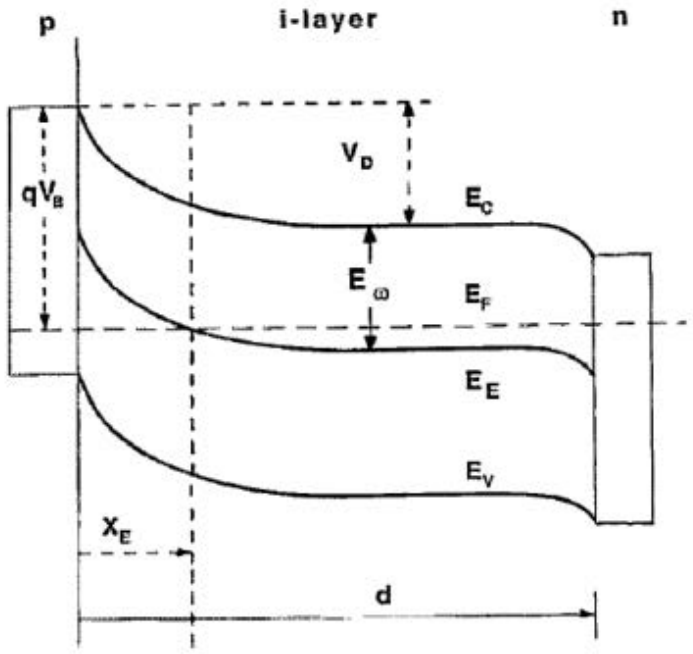

FIGURE 2.3: Energy band diagram of a p-i-n junction of a solar cell. Here p is the hole transport layer, i the perovskite and n the electron transport layer. Indicated in the figure are the built-in field V_b, the energy level of the conduction band E_C, the energy level of the valence band E_V, the Fermi-level E_F, V_D which denotes the band-bending, X_E which denotes the width of the p-i junction, d, which denotes the width of the device and E_E which represents the centre of the trap distribution. Taken from [33].

extracted move down in energy when moving through the different layers, and the holes move up in energy level (this is an energy favourable state since holes (electron vacancies) want to be filled). The potential difference between the energy level difference of the extracted electrons and the extracted holes yields to solar cell potential. In the case of PSCs, the perovskite layer in combination with the various possible electron and hole transport layers and contacts yield complex behaviour, which is discussed in section 2.1.4.

As photons with a lower energy than the band gap of the semi-conductor do not get absorbed, and excess energy of photons with higher energy than the band gap is lost as heat, there is a limit to the efficiency of a (single-junction) solar cell. This fundamental limit in efficiency corresponding to the optical bandgap is dictated by the Shockley-Queisser limit. $MaPbI_3$, the most researched perovskite solar cell, has a direct band gap of between 1.5 and 1.6eV [60]. The estimated theoretical PCE of $MaPbI_3$ is $\sim 31\%$, with $V_{oc} \approx 1.3V$, calculated for a 500nm thick $MaPbI_3$ single junction solar cell [31]). Solar cells are characterised by their illuminated current-voltage (JV) characteristics. The JV-characteristics of a solar cell, including indication of the relevant parameters, is presented in Figure 2.4. The estimated theoretical J_{sc} and FF for the same 500nm $MaPbI_3$ single junction solar cell are $\approx 26 mAcm^{-2}$ and 91%, respectively.

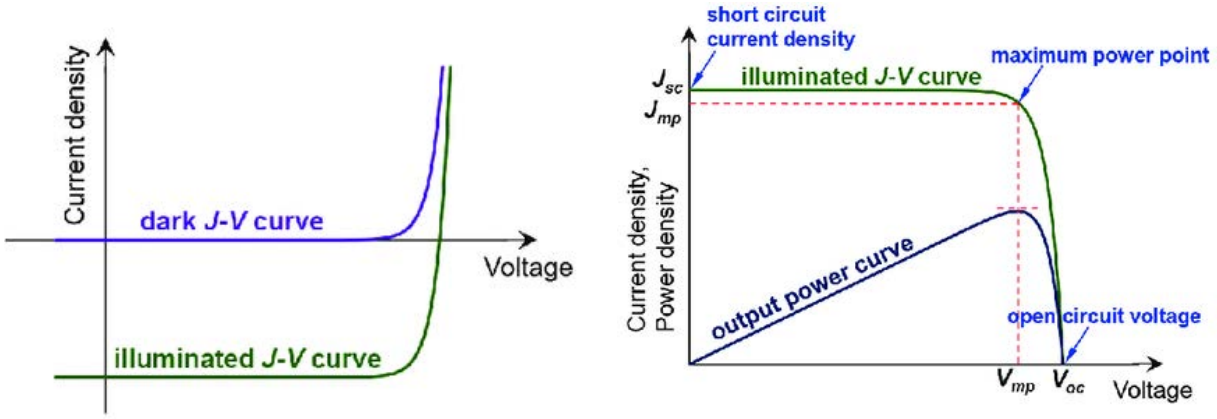

(A) JV characteristics.

(B) Indication of relevant solar cell performance parameters.

FIGURE 2.4: JV-characteristics including indication of relevant solar cell parameters. a) JV-characteristic of a solar cell under dark conditions, displaying diode like behaviour, JV-characteristic of a solar cell under illuminated conditions, shifted down with respect to the dark JV-characteristic. b) Relevant solar cell performance parameters. The *short-circuit current density* J_{sc}, *open-circuit voltage* V_{oc} and *the maximum power point MPP* are indicated. The *Fill Factor* is defined as the area between J_{mp} and V_{mp}. Taken from [61].

2.1.3 Degradation and stability

Whereas perovskite solar cells can be made with remarkable efficiency, the longevity of the device is of great importance as well. PSCs suffer from instability, due to both extrinsic and intrinsic causes. Extrinsically, first of the degradation pathways is exposure to moisture. When $MaPbI_3$ is exposed to humid air, two competing reactions take place: (i) the formation of an $MaPbI_3$ hydrate phase due to H_2O incorporation, and (ii) PbI_2 formation due to the desorption of MaI. Further degradation then takes place by subsequent loss of Ma^+ and I^-, and decomposition into $PbCO_3$, $Pb(OH)_2$, and PbO [31]. $MaPBI_3$ is also unstable against oxygen exposure, primarily due to the large driving force of water formation. The degradation happens rapidly in light conditions, while sluggish in dark conditions due to slow surface reaction kinetics in the dark [62]. Perovskite degrades as well if local temperature increases to 100° Celsius, and at

57° Celsius the phase change of tetragonal to cubic takes place. Although the phase change for $MaPbI_3$ does not induce big changes in the optical properties, the phase change acts as a catalyst for degradation processes in the perovskite crystal [31]. UV light also degrades PSCs, both due to PbI_2 formation and through the presence of UV-photocatalitic TiO_2 as transport layer [63]. An UV-filter placed over the PSC then protects the device against UV photo-induced degradation. Encapsulation of PSC devices helps to prevent humidity and oxygen from degrading the device. Even when perovskite devices have been properly encapsulated, or measured in inert atmosphere, they might still be unstable and prone to degradation for intrinsic thermodynamic reasons such as ion transport and mobile defects due to stoichiometry. The mechanisms leading to degradation of perovskite solar cells are displayed in Figure 2.5.

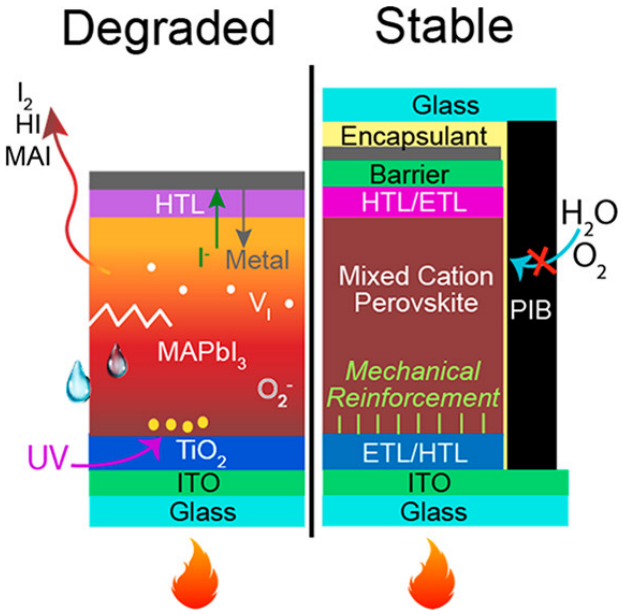

FIGURE 2.5: Degradation in perovskite solar cells. On the right, a stable perovskite solar cell where an encapsulant (PIB) blocks water vapour or oxygen from entering the solar cell. On the left, a degraded perovskite solar cell. Extrinsic degradation pathways are moisture, oxygen, temperature or UV radiation. Intrinsic degradation pathways are ion migration or defects through non-ideal stoichiometry. Taken from [64].

2.1.4 Hysteresis and transient processes

Hysteresis in the JV-scan shows through non-overlapping JV-characteristics for forward and reverse voltage scan direction, or for the same scan direction at different scan speeds. This is displayed in Figure 2.6. In this case, important solar cell performance parameters become dependent on external measurement parameters such as scan direction and scan speed. Apart from problematic extraction of reliable solar cell parameters, hysteresis is also linked to degradation in the long term [25, 26, 27]. Therefore, effort is taken to reduce hysteresis in PSCs.

Hysteresis is the result of multiple interdependent transient processes that are not fully understood at the microscopic scale. The transient processes involved are ion migration, ion accumulation at the transport layers interface, interface dipoles, charge extraction/injection and recombination. Briefly, hysteresis is primarily caused by mobile ions in the perovskite layer and trap assisted and/or surface charge recombination [28]. The next paragraphs deal with a more

inclusive description of how hysteresis is established. Since a PSC is a dynamic system containing both contributions from electronic conduction and ionic conduction, first electronic conduction is described, then ionic conduction, and finally the interaction between the two which causes hysteresis. Hysteresis therefore is an epiphenomenon, composed of both first order processes and their interaction (second order processes).

Electronic conduction in a PSC can be summarised as follows. In the case of photo-generated electrons and holes, the charges are separated due to the built-in voltage formed by the HTL and ETL, and within the depletion region drift towards their respective electrodes. If the perovskite is not completely depleted, the photocharge relies on diffusion to reach their electrode. Transport within one solar cell layer is called *charge transport*. Electrons/holes can also be injected/extracted by the application of an external electric field (bias voltage) across the device. This can reduce or enhance the internal field in the solar cell. After charge separation and transport, charge is transiently *transferred* across various interfaces. Before extraction, charge carriers can *recombine* through traps, defects at any of the interfaces or due to vacancies or interstitials in the perovskite structure. These defects and traps might have formed during the fabrication process, but can be a result of a chemical reaction during degradation processes as well.

Ionic conduction of PSCs happens through the presence of mobile I^- and Ma^+ ions in the perovskite layer, which redistribute under influence of an electric field [19]. This happens due to the built-in voltage, due to light soaking, and can also be induced by the application of an external electric field as well [28]. JV-scans transiently vary the external field, which subsequently transiently modifies the ion distribution in the perovskite. Ions redistribute on a time scale which is dictated by their diffusion coefficient of $\approx 10^{-12} cm^2 s^{-1}$, making their response relatively slow in comparison to much faster electrical conduction. Vacancies in the perovskite structure, formed during perovskite film formation, can encourage ion migration. Apart from perovskite material, also ions from conductive contacts can migrate through the perovskite layer [65]. This can create recombination centers or shunt pathways for electrons, short-circuiting the solar cell.

Ions may accumulate at the transport layer interfaces. Here, they influence charge extraction via two pathways. First, the ionic charge can screen the built-in potential of the solar cell. Then the depletion region becomes smaller, and charges rely more on diffusion than drift to reach their respective electrodes. This facilitates recombination at the wrong electrode and hampers charge extraction [28]. Conversely, when a voltage pre-bias opposite of the built-in voltage is applied, the ions redistribute towards their respective electrodes, which then augments charge extraction. Therefore, ion accumulation can influence charge extraction over time. This adds a time-dependent component to electrical conduction, which can lead to hysteresis in the JV-curves. Apart from influencing charge extraction in this way, ion accumulation seems to change the interface energetics at the contacts. This happens in two ways: a) through the introduction of interface dipoles which shift the electrode work function between conduction and valence band of the perovskite layer [66] and b) by changing local charge carrier densities, affecting trap filling and local doping of interface regions. Depending on the quality of the interface, ion accumulation may exhibit both spatial and a kinetic asymmetry, adding yet another layer of complexity. For both pathways, ion accumulation only affects the performance of devices with deficient interfaces where charge can recombine non-radiatively [28].

Thus, hysteresis is the consequence of mobile ions and their impact on charge extraction and recombination, mostly at the interfaces. The mechanisms explained above are schematically presented in Figure 2.6. The figure depicts how mobile (accumulating) ions in combination with deficient interfaces can lead to hysteretic currents during the JV-scan. A schematic illustration of how the ionic and electronic response in PSCs interact to cause hysteresis is seen in Figure 2.7. Seen on the left is the ionic response and seen on the right is the electronic response (in yellow). The factors defining and influencing the electronic/ionic responses are displayed at the sides (in the indigo boxes). The interaction between the ionic and electronic response is shown

in red. Hysteresis originates through time-dependence in the electronic response, induced by migrating ions influencing the electric field and modifying interface dipoles of the PSC.

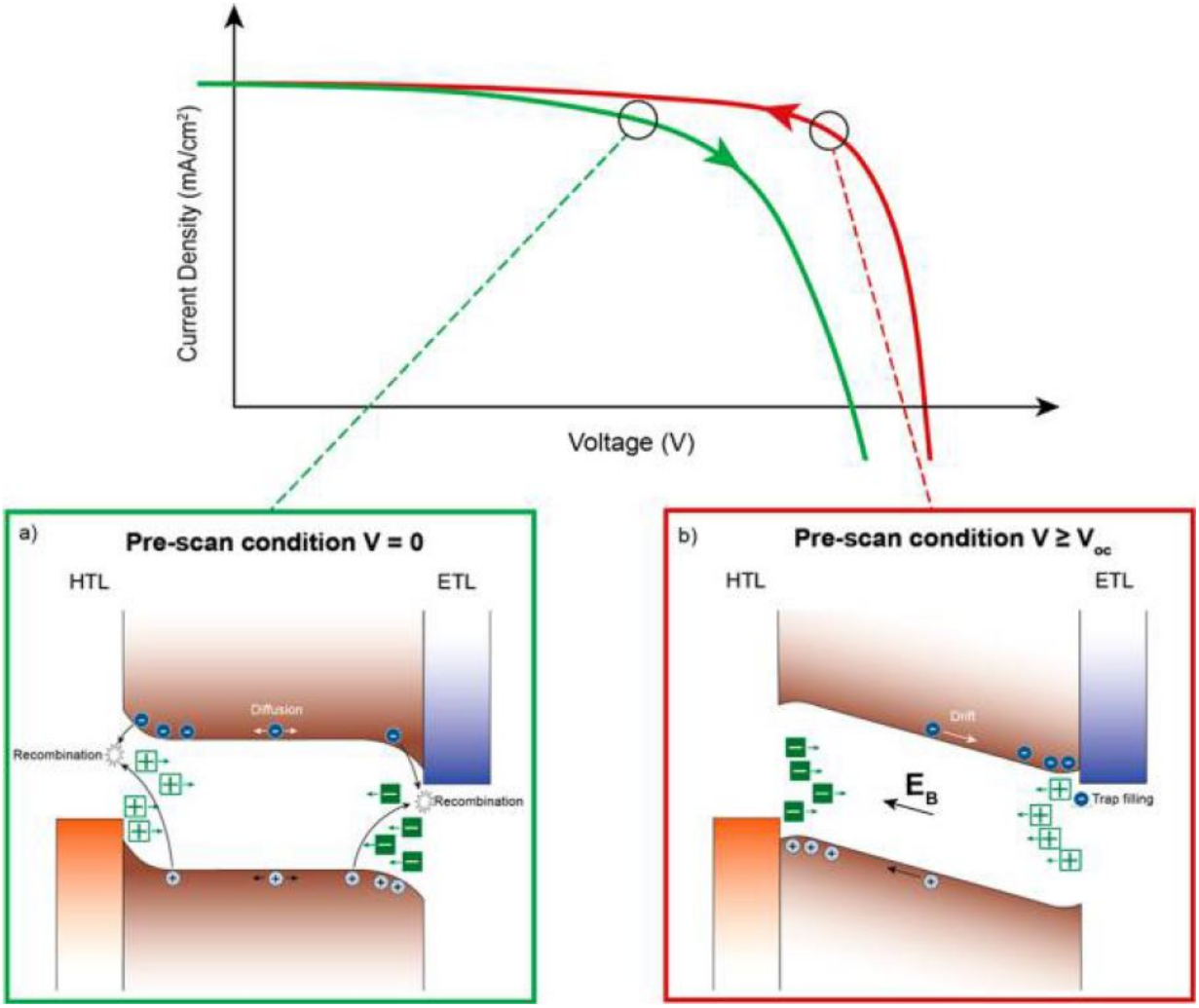

FIGURE 2.6: Hysteresis in perovskite solar cells. For a forward scan (a), ion accumulation at the transport layer interfaces screens the built-in potential. Electrons and holes therefore rely on diffusion to reach their respective electrodes, and may recombine at the wrong electrode. For a reverse scan (b), the voltage pre-bias drives the ions to the opposite transport layer interface, enhancing the built-in potential and beneficially filling trap states. Electrons and holes rely on drift to reach their respective electrodes. This process increases charge extraction, as can be seen from the superior reverse JV-scan. Taken from [28].

Though perovskite cells of good quality without hysteresis exist, those cells might still have mobile ionic species present. Good quality of the cell merely causes almost no surface or bulk recombination, making charge extraction independent from redistribution of ionic charge during JV-scan. This strategy to reduce hysteresis by improving interfaces includes interventions such as (non-exhaustively) modification of the interfacial band alignment, chemical surface modification of the perovskite, defect and trap site passivation, tuning the charge collection layer, removing simple imperfections such as pinholes or electrode penetration, etc. Though these interventions reduce hysteresis, they do not reduce ionic movement throughout the perovskite absorber layer [28].

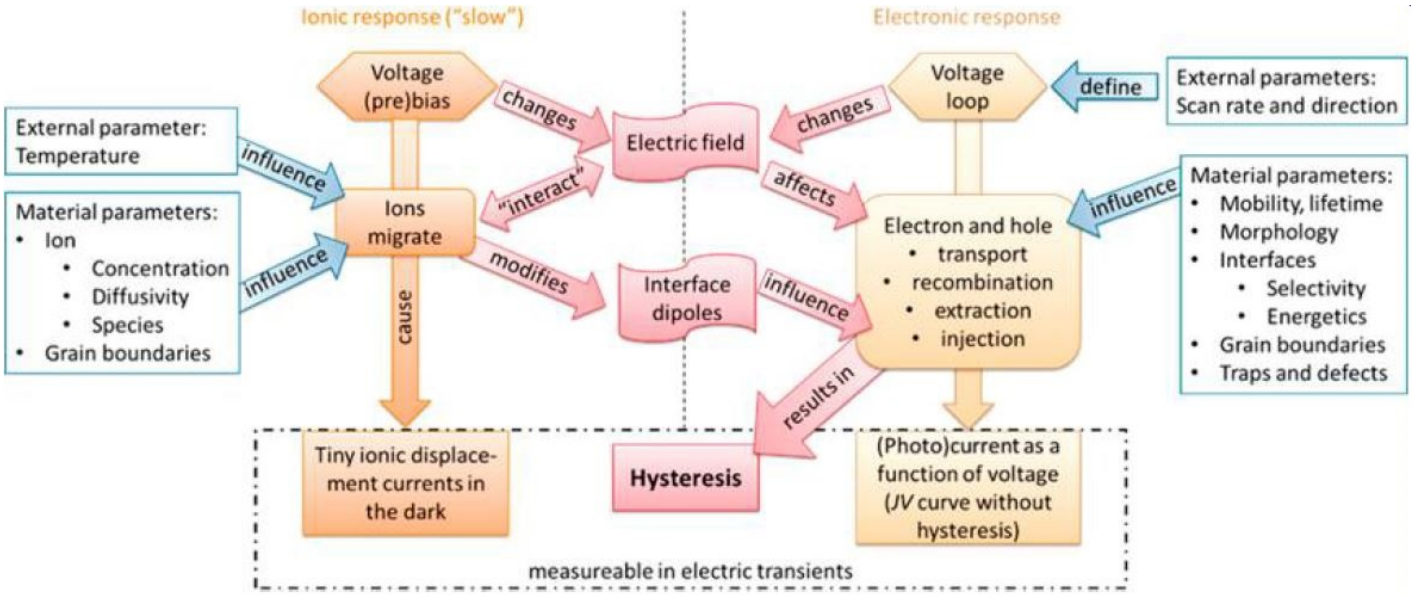

FIGURE 2.7: Complex interdependent behaviour of transient processes in metal halide perovskite solar cells. The figure is split in the ionic and electronic response (yellow), the factors defining and influencing these responses (in indigo) and the interaction between the ionic and electronic response (in red). Hysteresis originates through time-dependence in the electronic response induced by migrating ions influencing the electric field and modifying interface dipoles of the PSC. Taken from [66].

The complex ionic-electronic behaviour originates from both the perovskite absorber layer and the material and quality of the contact layers. Hysteresis relates to many time-dependent (transient) processes in the solar cell. The various transient processes are schematically displayed in Figure 2.8. It also displays the contact layers used for the PSC samples in the experimental section of this research.

The figure is schematically divided into three regions. The most right region contains processes in solar cells in general (electronic processes), the middle region processes specific for perovskite solar cells (ionic processes), and the left region processes induced by application of an external bias voltage across the device (for voltage-dependent measurements). First, electronic processes are described, then ionic processes, and finally the left section containing effects induced by application of an external voltage.

Transient processes in solar cells are generally electronic and entail *electron/hole transport*, *charge transfer*, *trapping/detrapping of charge carriers* and *recombination*. Transport of charge happens within a solar cell layer, charge transfer across interfaces. Since interfaces and materials are not perfect, trap states may exist which can hold charge. Charge can then either recombine or become free charge again (detrapping). Recombination occurs on the microsecond time-scale and may also be dependent on the specific transport layer used [67]. Good power conversion efficiency simply implies charge transport and extraction processes occur on a much faster time-scale than the recombination processes. Experimentally it was verified that charge separation and extraction processes happen on the femto- to nanosecond timescale [67].

Since PSCs contain mobile ions, these ions may redistribute due to electric fields and light soaking. This is called *ion transport*. The change in capacitance associated with ion transport can be probed on the time-scale of milliseconds (for I^- ions) to seconds (for MA^+ ions) [19]. There is still debate on the time-scale of ion migration. Based on the short diffusion path and the high mobility, it has also been argued that ionic migration should be almost instantaneous [44]. At the interface, *Ion accumulation* can occur. The consequence of ion accumulation is variation

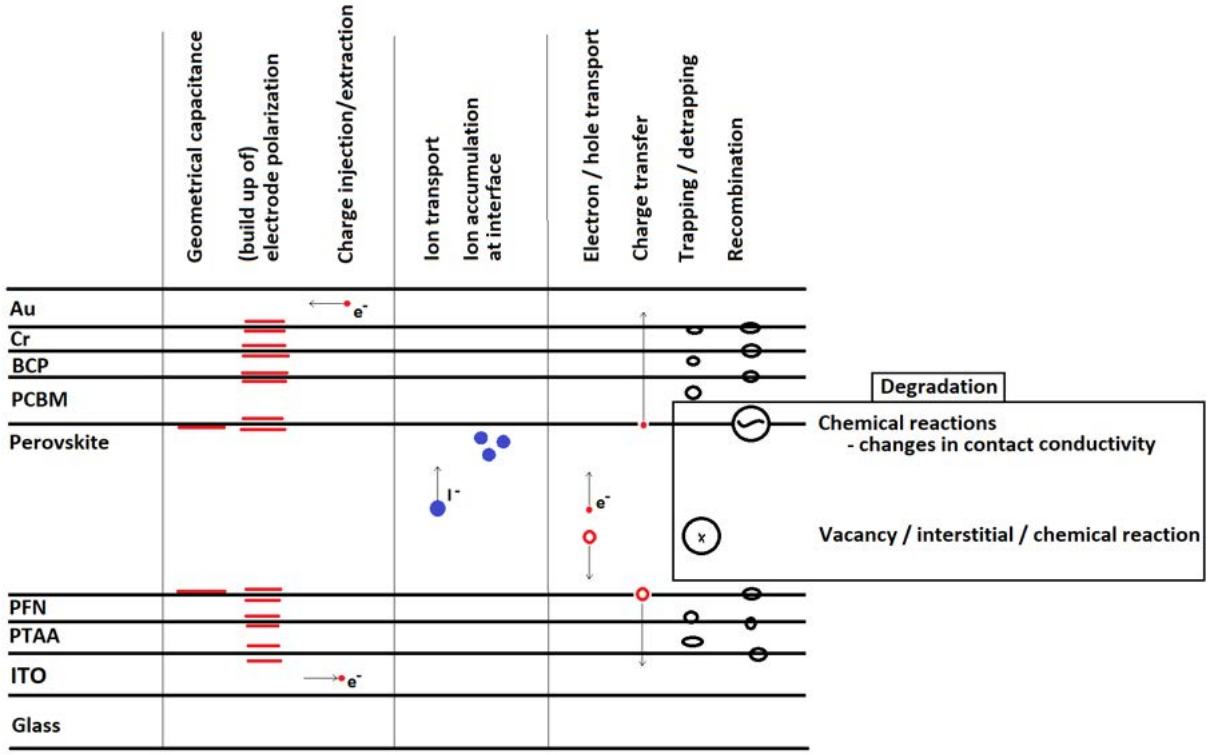

FIGURE 2.8: Transient processes in perovskite solar cells. On the left are processes induced by application of an external bias voltage, in the middle are ionic processes present in perovskite solar cells and on the right are electronic processes in solar cells. Typical layer thicknesses are 20nm for PTAA, 5nm for PFN, 500nm for perovskite, 70nm for PCBM, 5nm for BCP, 3nm for chromium and 100nm for the gold electrode.

in the time-scales of electron and hole transport, recombination, extraction and injection, as is indicated in Figure 2.7. Apart from these processes, chemical reactions can lead to changes in absorber or contact conductivity.

If voltage-dependent measurement are taken of the PSC, the device is subjected to an external (bias) voltage across the device. In this case, the device exhibits different capacitive behaviours. When the bias voltage is low, the semi-conducting perovskite behaves as an insulator. Then, the device can be approximated as a parallel plate capacitor with perovskite as dielectric. This is called *Geometrical capacitance*. This happens on the time-scale of micro-seconds [68], and it is voltage dependent. Due to interfacial characteristics, a bias voltage can lead to *(build up of) electrode polarisation*, forming an interfacial double layer capacitance. Additionally, due to the applied potential, the Fermi-levels shift and charge is injected and extracted. Charge injection happens on a picosecond time-scale [67].

The transient processes in the microsecond to second range can be assessed using impedance spectroscopy. The processes within this range are geometrical capacitance and recombination as well as ion migration. The time-scales named for the different processes can be experimentally extracted using Equivalent Circuit Modeling to yield information about the nature of perovskite solar cells. The concepts related to impedance spectroscopy, equivalent circuit modeling and Kramers-Kronig compliance testing for reliable results are described in the next section.

2.2 Impedance Spectroscopy

Impedance spectroscopy (IS) is a powerful tool to characterise electrochemical systems and solid-state devices [69]. Solid-state application of IS is most commonly on dielectrics; materials which polarise (store charge) under influence of an electric field. A solar cell is a system of multiple materials of different energy levels and polarisability stacked on top of each other. Both every material and every interface can contribute to the total resistive and capacitive response of the system [70]. Impedance spectroscopy can assess this response, and discriminate between different microscopic processes, provided the processes happen on distinctive time-scales. The electrical processes are probed by a frequency-varied perturbation signal. The frequency window of an impedance measurement is limited, and usually not fast enough to probe all electronic processes in the solid state device. Common processes and parameters measured with IS are electron transfer rates, recombination rates, trapping of charges, resistance and capacitance related to charge transport, capacitance of insulators and conductivity of conductors.

When IS is used to study emerging photovoltaics, it is possible to observe the opto-electronic transport and recombination processes of a solar cell under operating conditions. In this way, device aging or performance loss through external stress factors can be evaluated. IS can also be used to identify differences in fabrication protocol by characterising the opto-electronic response of solar cells [33].

IS has multiple limitations. Firstly, only by determining a model beforehand, dictating where in the device which physical processes take place, information about these processes can be extracted by fitting the impedance spectra to the model. Additionally, different models may result in the same impedance spectra. This means no unique solution to the impedance spectrum is available, and postulating a physical relevant model is increasingly intricate for the analysis of complex device architectures combined with unusual material properties of emerging photovoltaics [33]. Secondly, the contribution of different physical processes to the impedance response can only be determined when the processes are happening on distinctive time-scales. Thus, the physical interpretation of the data is in many cases problematic. To increase the reliability of the IS analysis for complex systems, a model should be chosen carefully. Additionally, it is good practice to corroborate the results from IS with other independent experimental techniques to verify that the chosen model is physically reasonable [69].

To summarise, IS is a tool which can model systems under very controlled and simplified conditions (such as well-defined geometry, inert contact layers, and controlled atmosphere and temperature), and characterise full solar cells under technical relevant operating conditions. Therefore, IS should be the most appropriate technique on the device level to assess complicated behaviour and interplay of electronic and ionic charge transport phenomena [44].

2.2.1 Basic operating principle of IS

In Impedance Spectroscopy a sample is subjected to a small alternating voltage V_{AC} as input signal. The V_{AC} may be superimposed on a DC offset V_{DC} (also called *bias voltage*). The input signal $V(t)$ is denoted by equation 2.1. The sample response is observed by monitoring the current output $I(t)$, equation 2.2. The current output can have a phase delay ϕ due to the sample storing and dissipating electrical energy [35].

$$V(t) = V_{DC} + V_{AC}\, cos(\omega t) \tag{2.1}$$

$$I(t) = I_{DC} + I_{AC}\, cos(\omega t - \phi) \tag{2.2}$$

The impedance (Z) is defined as the ratio of voltage and current, equation 2.3.

$$Z \equiv \frac{V}{I} \tag{2.3}$$

In these expressions, ω denotes the angular velocity, related to the frequency as $\omega = 2\pi f$. To study resistive and capacitive properties of solar cells, the frequency is swept over a range between subhertz and megahertz in a typical impedance measurement. By varying the frequency, various electronic and ionic processes are probed sequentially and a spectrum is obtained. Each process has a relaxation time-scale, which is the time it takes for the sample to return to a state of equilibrium after the electrical perturbation. The relaxation time-scale can be calculated after fitting.

After a frequency sweep, the bias voltage might be adjusted and the process is repeated. In this way for each step in bias voltage, the frequency dependence of the resistive and capacitive properties becomes clear at every point along the J-V curve of the solar cell. In Figure 2.9, the input and output signal are displayed in the time-domain.

When a sinusoidal signal is applied to the sample, it's current response needs to be linear to ensure a sinusoidal current response. Ideal components, such as resistors, capacitors and inductors, guarantee a linear response [33]. Non-ideal circuit elements, such as a diode, do not. Since a solar cell is essentially a diode, the response of the sample is nonlinear, which can be clearly observed from non-linear nature of the JV-curve. However, this problem can be solved by applying a *small* input signal V_{AC}, usually about $20mV$, through which a pseudo-linear regime in the current response is reached [35]. The consequence of measuring in the linear regime is that near the open circuit voltage V_{OC} a smaller amplitude of the input signal V_{AC} must be used than for the short circuit voltage V_{SC}, as is illustrated in figure 2.9.

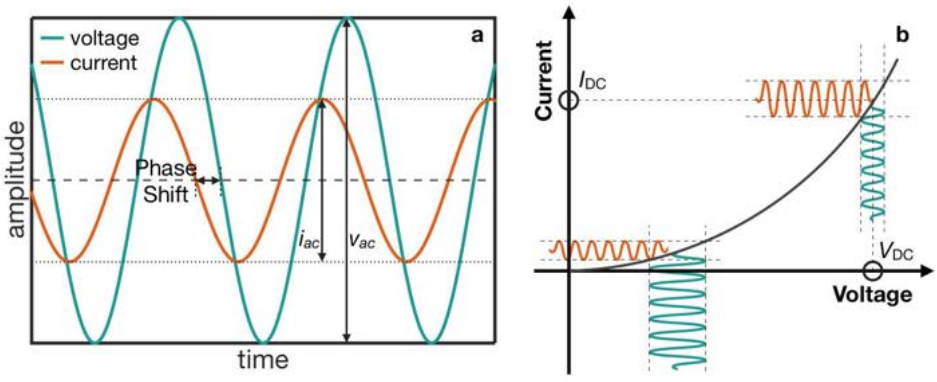

FIGURE 2.9: Impedance measurement in time domain (a) and visualisation of the input and output signal on JV-characteristics (b). Taken from [35].

Since the signals are complex quantities, they can also be written in polar form, $\hat{E} = |E_0|e^{i\omega t}$ and $\hat{I} = |I_0|e^{i(\omega t+\phi)}$, where $\hat{E}$ is the time-varying electrical field and $\hat{I}$ is the complex valued current response [1]. The complex impedance can be calculated using equation 2.3 and split in it's real and imaginary part, equation 2.4.

$$Z(\omega) = (|E_0|/|I_0|)\, e^{-i\phi} = |Z|(cos(\phi) - isin(\phi)) = Z_{Re} - iZ_{Im} \tag{2.4}$$

In the expression, $|E_0|$ and $|I_0|$ denote the magnitude of the alternating voltage and current. $|Z|$ is the magnitude of the complex impedance, and is both the fraction of the stored and dissipated energy as the magnitude of the vector of Z in the complex plane, $|Z| = |E_0|/|I_0| = (Z_{Re}^2 + Z_{Im}^2)^{1/2}$. ϕ in the complex exponential denotes the phase change, where $tan\phi = Z_{Im}/Z_{Re}$. Z_{Re} is also denoted as Z', and Z_{Im} as Z'', which will be used further on to denote the real and imaginary part of impedance. The real part in equation 2.4 is physically the real resistance R, whereas the imaginary part is physically the reactance X. Resistance is the opposition of a circuit element to the flow of electrical current. Reactance is the opposition of a circuit element to a change in current or voltage, due to the inductance or capacitance of the circuit element [69]. The SI units of impedance, resistance and reactance are Ohms. Thus, equation 2.4 can be written as

$$Z = |Z|e^{-i\phi} = R - iX = Z' - iZ'' \tag{2.5}$$

Z' and $-Z''$ can be displayed as the axes of the complex plane as in Figure 2.10.

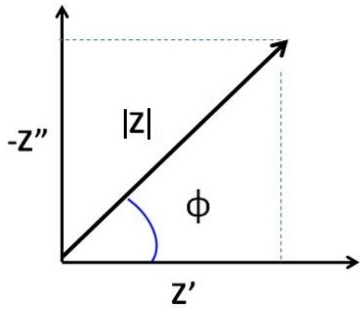

FIGURE 2.10: Complex plane representation. Z', -Z'', ϕ and |Z| are indicated. Taken and adapted from [33].

2.2.2 Impedance of ideal components and the RC circuit

The impedance of a parallel connected RC circuit is built up by the impedance of a resistor and a capacitor, and describes a time-dependent *process* in general. An RC circuit in combination with a linear series resistance is the most simple equivalent circuit model with which a transient process can be fitted, and is called a *Randles* model. The impedance of an RC circuit can be calculated by applying Kirchhoff's circuit laws of in series or in parallel connected circuit elements. The impedance of a parallel RC circuit is therefore $1/Z_{RC} = 1/Z_R + 1/Z_C$.

The impedance of the ideal circuit elements resistor R, capacitor C and inductor L can be described by $Z_R = R$, $Z_C = 1/i\omega C$ and $Z_L = i\omega L$. The impedance of a RC element can be found by applying Kirchhoff's law for addition of parallel composed circuit elements, yielding equation 2.6.

$$Z_{RC} = \frac{R}{1 + i\omega RC} \tag{2.6}$$

This denotes a single time-scale process, with characteristic time τ being

$$\tau = RC \tag{2.7}$$

This is closely related to the maximum of the semi-circle of the response of an RC-circuit, and its corresponding frequency, by $\omega_{peak} = \frac{1}{\tau} = \frac{1}{RC} = 2\pi f$. To display the time-constant in seconds, τ needs to be multiplied with 2π, resulting in $\tau \cdot 2\pi = 1/F_{peak}$.

By multiplication with the complex conjugate $(1 - i\omega RC)$ divided by itself (multiplication with 1), equation 2.6 can be split in its real and imaginary parts Z' and Z''.

$$Z_{RC} = \frac{R}{1 + \omega^2 R^2 C^2} - \frac{i\omega R^2 C}{1 + \omega^2 R^2 C^2} = Z' - iZ'' \tag{2.8}$$

The impedance response of a RC-circuit Z_{RC} follows the mathematical description of a (semi-)circle. This can be checked by filling in Z' and Z'' in the formula of a circle. The formula of a circle taking Z' as x and Z'' as y and with radius r and center at $x = a$ is

$$(Z' - a)^2 + Z''^2 = r^2 \tag{2.9}$$

The center a of the circle can be found by taking the maximum value of Z' for $\omega = 1/RC$ (the x-value for the y-maximum of the semi-circle), which results in $a = R/2$. With the appropriate center a of the circle chosen, Z' and Z'' can be inserted in equation 2.9. Working out will result in the radius r as being a constant, independent of ω, thus all the points of Z_{RC} are distributed on a circle.

This corresponds to the following observations: at high frequencies, the impedance of a capacitor $Z_C = 1/i\omega C$ goes to zero and thus acts as a short-circuit, resulting in an impedance approaching the origin. at low frequencies the impedance goes to infinity (and the overall impedance of the RC circuit goes to the parallel resistor R). At intermediate frequencies, the impedance of the RC circuit has a maximum described by $\omega_{peak} = 1/RC = 1/\tau$. The peak in the Nyquist plot corresponds to the time constant τ of a *process* in general. Here, it physically is the time it takes for the RC circuit to charge and discharge [35].

2.2.3 Non-ideal components

Experimental data of a real device does not necessarily generate a perfect semi-circle. Instead, a flattened semi-circle is observed. A flattened semi-circle indicates dispersed time-constants. This can be due to different factors: non-homogeneities such as porosities and roughness, non-ideal chemical capacitances, surface states which are present in the device [30], or simply due to two processes happening on approximately the same frequency (decade). In this case, the capacitor can be replaced by a constant phase element (CPE). The impedance of a CPE is $Z_{CPE} = 1/Q(i\omega)^n$, where $Q = CPE_T$ and $n = CPE_P$. In the ideal case when $n = 1$, the CPE reduces to a pure capacitor and $Q = C$, while for $n = 0$ it reduces to a pure resistor and $Q = 1/R$. Typically for PSCs it takes the value of 0.9.

If $n = 0.5$, the CPE reduces to a Warburg element and $Q = 1/A_W$. A Warburg element produces a 45° slope in the Nyquist plot and denotes ion (mass) transport. The Warburg impedance is given by $Z_W = A_W/\sqrt{i\omega}$. The Warburg coefficient A_W depicts the ac diffusion coefficient of the particles [33]. From the W_T parameter, the effective chemical diffusion coefficient (D) can be calculated [30].

$$D = \frac{L_D^2}{W_T} \tag{2.10}$$

where L_D^2 is the effective ion diffusion length. The maximum diffusion length can be assumed to be equal to the perovskite film thickness (about 500nm). From this value, the majority

carrier mobility μ can be calculated, equation 2.11, where q is the elementary charge, k is the Boltzmann constant and T is the temperature [30].

$$\mu = \frac{Dq}{kT} \tag{2.11}$$

2.2.4 Graphical representations of impedance spectra

Impedance spectra are commonly represented in two forms: Bode plots and Nyquist plots. The Bode plot representation of impedance spectra is in the frequency domain, where different quantities such as $|Z|$ and ϕ are plotted relative to the frequency. Nyquist plots however are impedance spectra plotted in the complex plane with the imaginary part of impedance Z'' (reactance) plotted relative to the real part of impedance Z' (resistance).

See Figure 2.11 for an example of a Bode plot of a parallel connected resistor and capacitor (RC-circuit). In the bottom part of Figure 2.11 it shows that a change in slope in the real value of Z leads to a peak in the imaginary value of Z.

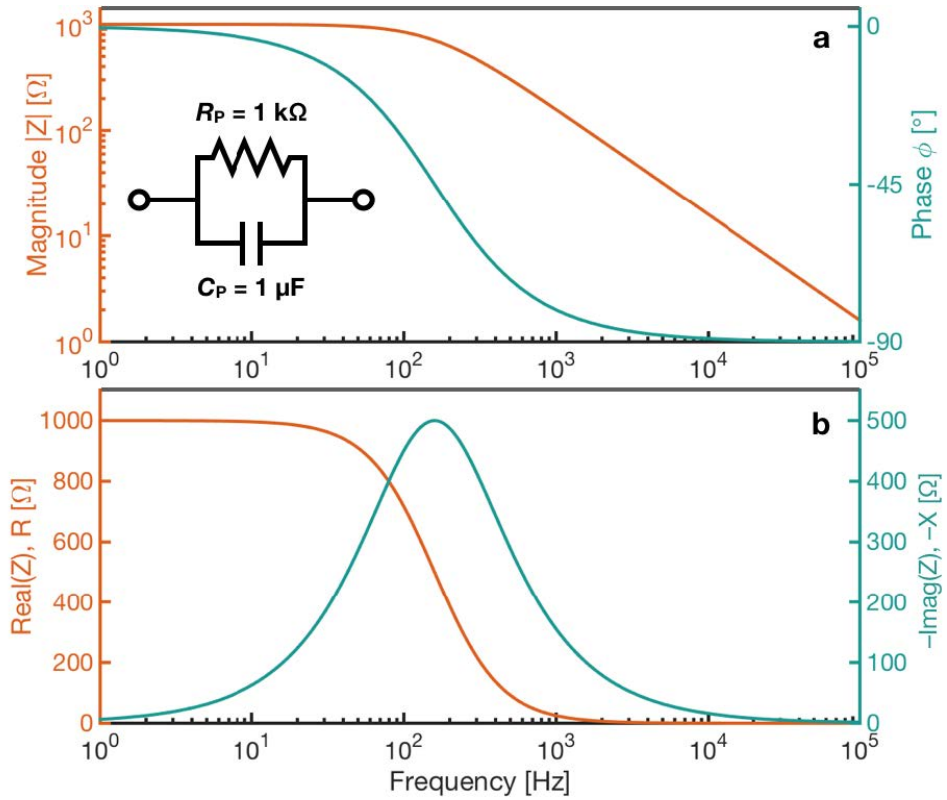

FIGURE 2.11: Bode plot of the impedance response of an RC circuit. In a) the magnitude and phase of Z versus frequency, in b) R and X versus frequency. Take note that a change in slope of real resistance results in a peak in the reactance. Taken from [35].

An example of a Nyquist plot is shown below in Figure 2.12. Here, Z' is the horizontal axis and denotes the real resistance. Z'' is the vertical axis and denotes the reactance of the sample due to it's capacitance or inductance. It is seen that the frequency information of the impedance spectra is lost in a Nyquist plot. However, the use of the nyquist plot is to facilitate the recognition of processes happening in the device. This is easier in a Nyquist plot than in a Bode plot. Therefore the Bode plot and Nyquist plot provide complementary information and together lead to a strong understanding of the processes in complex devices such as perovskite solar cells [35].

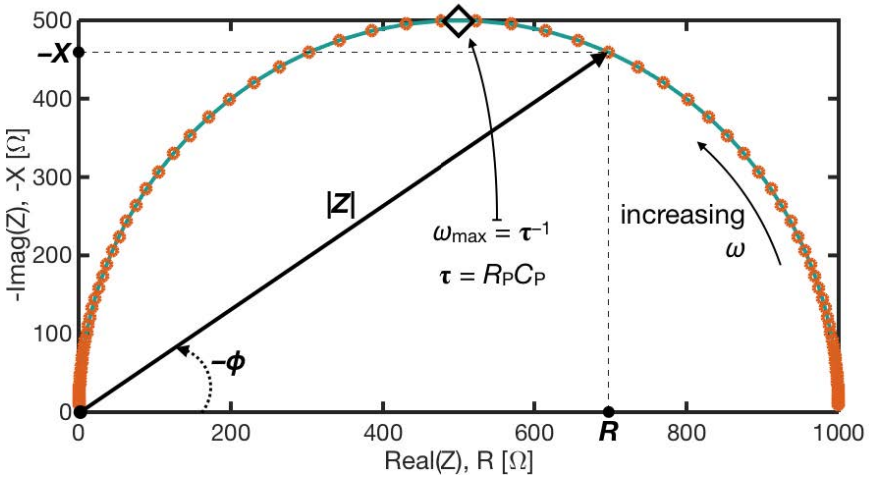

FIGURE 2.12: Nyquist plot of the impedance response of a parallel RC circuit. The direction of increasing ω is indicated, as well as the time-constant related to the peak of the semi-circle. Taken from [35].

These example plots have been made by simulating the impedance response of a RC circuit. The Nyquist plot of a single RC circuit describes a semi-circle. This denotes a single time-scale relaxation process, meaning physically the capacitor charges and then discharges via the resistor taking a specific amount of time.

2.3 Kramers-Kronig compliance testing

For any impedance data to be reliable, the data should be a representation of a linear, time-invariant and causal system containing finite impedance values. If any of these requirements is violated, no useful information can be extracted from the measurement [37]. This demonstrates the usefulness of the Kramers-Kronig compliance test.

The linearity constraint dictates that the current output of the solar cell should be directly proportional to the applied input. For solar cells, typically depicting non-linear current-voltage characteristics, this constraint is satisfied by choosing the amplitude of the input signal V_{AC} significantly low so that a pseudo-linear regime arises at which Impedance Spectroscopy can be performed [33].

A time-invariant system is a system which has properties that do not change during the measurement in such a way that the final state differs from it's initial state. That is to say, the sample should be stable and not irreversibly change during the measurement. This is usually the case if an impedance spectrum can be reproduced under forward and reversed frequency sweeps. First order processes, such as conductivity of electrons or ions, are linear (Ohmic) processes and therefore KK-compliant, but second order processes such as a change in conductivity due to chemical reactions changing the electronic structure, are not KK-compliant. PSCs exhibit both permanent and temporary changes in performance, caused by irreversible processes (such as chemical reactions) and semi-irreversible processes (such as ion transport) [33]. Irreversible processes lead to KK-incompliance. However, ion transport is a special case for KK-compliance, as a sample with ion transport is unstable during the measurement and does not return to its initial state, though the sample properties do not change irreversibly and the measurement is KK-compliant unless ω approaches 0 (when ions accumulate at the contact interfaces). PSCs suffering from this kind of temporary loss of device performance may recover when stored in the dark in a glovebox for several hours [71].

A causal system is a system that only reacts to the applied input signal, and not to external factors. These may be cable inductance, increases in temperature or ambient electric fields leading to noise. Typically, sample reactions due to external factors express mainly in the low frequency impedance data, since lower frequencies have a longer measurement time than higher frequencies [72].

To verify the measured data is a representation of a linear, time-invariant and causal system, two approaches exist [37]. The first one is to verify experimentally, the second approach is by analysing the impedance spectrum with the Kramers-Kronig relations. Experimental verification has to be done in three distinct ways: by repeating measurements under the same conditions and seeing if the impedance data is reproducible [44], by changing the size of the excitation signal above and below the chosen value to ensure the excitation signal is well within the linear response regime [33], and lastly by performing reverse frequency sweeps from low to high, as opposed to high to low, checking if the measured impedance spectrum stays the same [73].

Verification if the data is a representation of a linear, time-invariant and causal system can also be done by analysing the impedance spectrum with the Kramers-Kronig relations. The Kramers-Kronig relations relate the imaginary part to the real part of a linear, time-invariant and causal system, and vice versa. The equations, first introduced by Kramers and Kronig [37] in a slightly different form, are displayed below:

$$Z_{Re}(\omega) = \frac{2}{\pi} \cdot \int_0^\infty \frac{\omega' \cdot Z_{Im}(\omega')}{\omega^2 - \omega'^2} d\omega' \tag{2.12}$$

$$Z_{Im}(\omega) = \frac{-2}{\pi} \cdot \int_0^\infty \frac{\omega \cdot Z_{Re}(\omega')}{\omega^2 - \omega'^2} d\omega' \tag{2.13}$$

Using these equations, it is possible to calculate the imaginary part of impedance from the real part, and conversely. It is then possible to compare the measured and calculated real component to each other, and to compare the measured and calculated imaginary component to each other in a plot showing the residuals between the two (a residual spectrum). Since the real and imaginary part are mathematically related, no deviation should be seen from the measured and calculated components. If a deviation is shown, then the data is KK-incompliant and dissatisfying any of the IS requirements above. Thus the accordance of the data to the Kramers-Kronig (KK) relations can be tested. However, directly applying the KK-relations proved to be prone to errors, due to its requirement to integrate omega from zero to infinity. This is impossible for real conducted experiments [36].

An approach that overcame this checks the accordance of impedance data to the KK-relations by first fitting the data to an appropriate KK-compliant equivalent circuit model. A very general circuit model was applied: a series of RC-elements. Initially both the resistances and the time-constants of the RC-elements were fitted, leading to a frequency dependent confidence interval for the impedance measurement. This method allows for the definition of a quantitative criterion to assess which parts of the spectrum should be disregarded, and which parts are KK-compliant. However, due to the non-linearity of the fitting problem this method has two big drawbacks. Good initial solutions have to be chosen, and secondly multiple solutions for minimising the cost-function at local minima exist. Therefore this method, although indispensable for a deep level analysis of KK-compliance of impedance spectra, costs a lot of effort if one quickly wants to assess the KK-compliance of several impedance spectra [37].

The Kramers-Kronig compliance test used in this thesis entails a modified version of the test described above, allowing for quick and easy KK-compliance testing. In this test, known as the Lin-KK test, the problems with the non-linearity were solved by presetting the time-constants of the RC-elements and only fitting the ohmic resistors. This leads to the fit-problem to become linear [37]. The Lin-KK tool used in this thesis is made publicly available from Karlsruhe Institute of Technology (KIT) [74].

2.3.1 Operation of Lin-KK tool

Fitting mode

Following the recommendation in the operating guide of the Lin-KK test program [74], the fitting mode has been set to *complex-fit*. This is the most robust method, as opposed to *real-fit* or *imaginary-fit* which can be used to increase the sensitivity of the test. In the *complex-fit* mode, the cost function J to be minimized is

$$J = \sum_{i=1}^{N} \left[\frac{Z_{Re}(\omega_i) - \hat{Z}_{Re}(\omega_i)}{\mid Z(\omega_i) \mid} \right]^2 + \left[\frac{Z_{Im}(\omega_i) - \hat{Z}_{Im}(\omega_i)}{\mid Z(\omega_i) \mid} \right]^2 \tag{2.14}$$

where N is the number of frequency points of the impedance spectrum to be tested and in the nominator the calculated component using the KK-relations is subtracted from the measured component. This distributes errors across the real and imaginary part of the residual spectrum.

Model order

A complication of the Lin-KK compliance test is the pre-setting of the number of RC-elements. If the number of RC-elements is manually set, easily situations of under-fitting and over-fitting are created. If the spectrum is under-fitted, not all impedance attributes of the spectrum can be fit, leading to large errors between the fit and the data (large residuals). If the spectrum is over-fitted, measurement noise is included in the fit, leading to large errors between the fit and the data as well. In both cases, large residuals are created, indicating incompliance while the spectrum may be KK-compliant. Therefore, the test includes a function to let the program choose the

appropriate number of RC-elements, *RC-auto*, which was used in the KK-analysis in this thesis. However, *RC-auto* may fail. If the function fails, this results in sinusoidal residuals. Then, the number of RC-elements should be carefully increased while simultaneously checking if the sinusoidal residuals disappear [74]. This approach has been followed in this thesis.

Capacity
When a measured sample shows mainly capacitive behaviour, a linear capacitor needs to be added to the series of RC-elements to ensure a good fit [38].

Inductivity
The test program automatically inserts a serial inductor to the fitting model to account for unavoidable inductive effects of the measurement setup (i.e. cable inductance).

2.3.2 Interpreting test results

The difference between measured and calculated real or imaginary component of the impedance is shown in a 'residual' plot, with on the X-axis the frequency range and on the Y-axis the magnitude of the residual. The calculated component is obtained by fitting an according KK-ideal circuit model. When the residuals present a straight line with residuals smaller than 0.5 and no apparent bias, the spectrum is KK-compliant and of good quality. An example is shown in Figure 2.13. If the real and imaginary residuals in the plot show a systematic deviation (bias) from each other over various orders of magnitude, this is called *time-variance*, which indicates KK-incompliant data [74]. An example is shown in Figure 2.14.

As stated in the Lin-KK operating guide, noise in the residuals, to some extent, is normal. If noise is too big, no information can be extracted on (in)compliance. If irregularities or systematic bias are shown in the noise, this is considered as KK-incompliant. Though the Lin-KK operating guide [74] does not set a maximum level of noise for the spectrum to still be KK-compliant, in this thesis noise in the residuals showing no systematic bias is considered compliant if the residuals are smaller than 2. However, residuals in the region of $0.5 - 2$ do indicate a spectrum of poor quality. As a rule of thumb, both the real and imaginary residuals should be smaller than 0.5, and should not show (weak) systematic bias or deviation from each other in order to guarantee KK-compliance and good measurement quality. If sinusoidal residuals are obtained, likely under-fitting has occurred due to a failure of *RC-auto*. In that case, the number of RC-elements is carefully increased while checking if the sinusoidal results disappear.

More examples of KK-compliant and KK-incompliant residual spectra, taken as a guideline to interpret the residual plots in this thesis, can be found in Appendix B.1. Take note that the example residual plots presented here and in Appendix B.1 show residuals ranging from -1 to 1 for informative purpose, whereas the residual plots presented in the results section of this thesis range both from -2 to 2 and from -1 to 1. Thus, on a quick glance comparing the residuals plots in the results section with the example residual plots here, one should not assume the same scale.

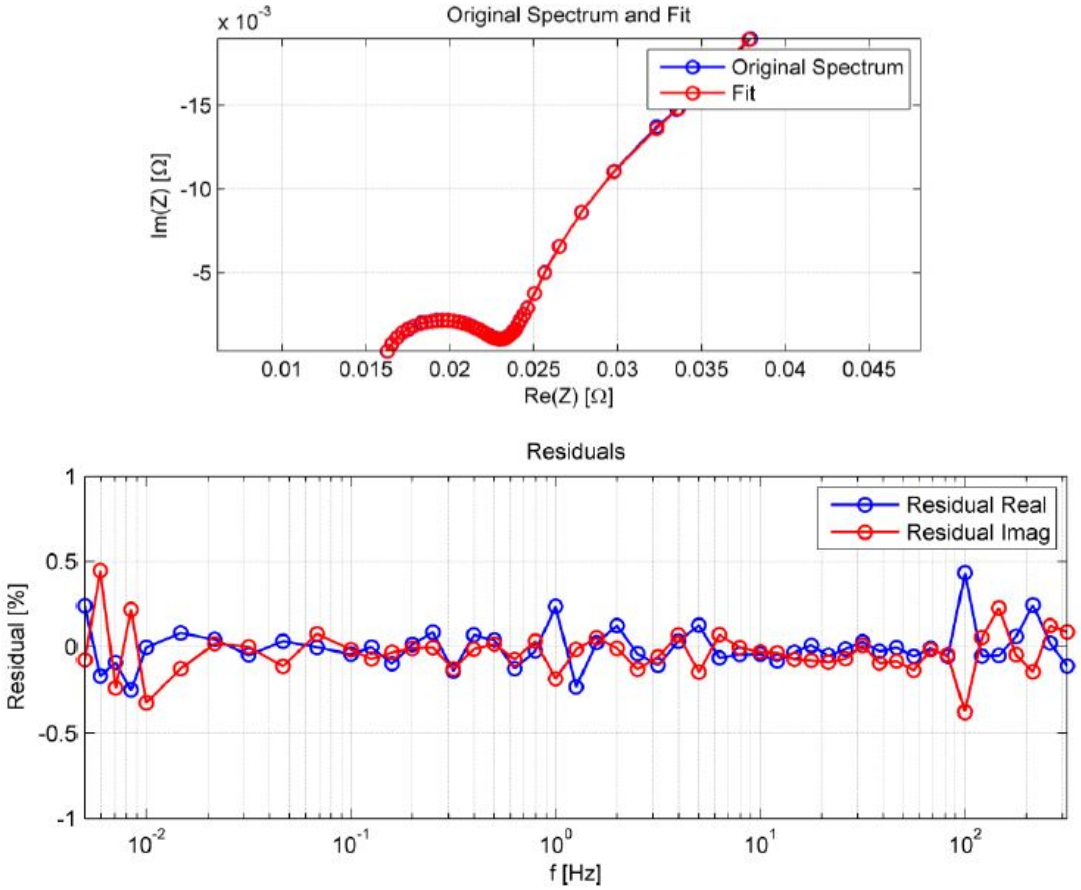

FIGURE 2.13: Valid Li-Ion Battery Spectrum (low noise situation). The residuals present a straight line which is well within the ± 0.5 border and which does not present systematic bias. Thus the spectrum is valid, time-invariant and of good quality. Taken from [74].

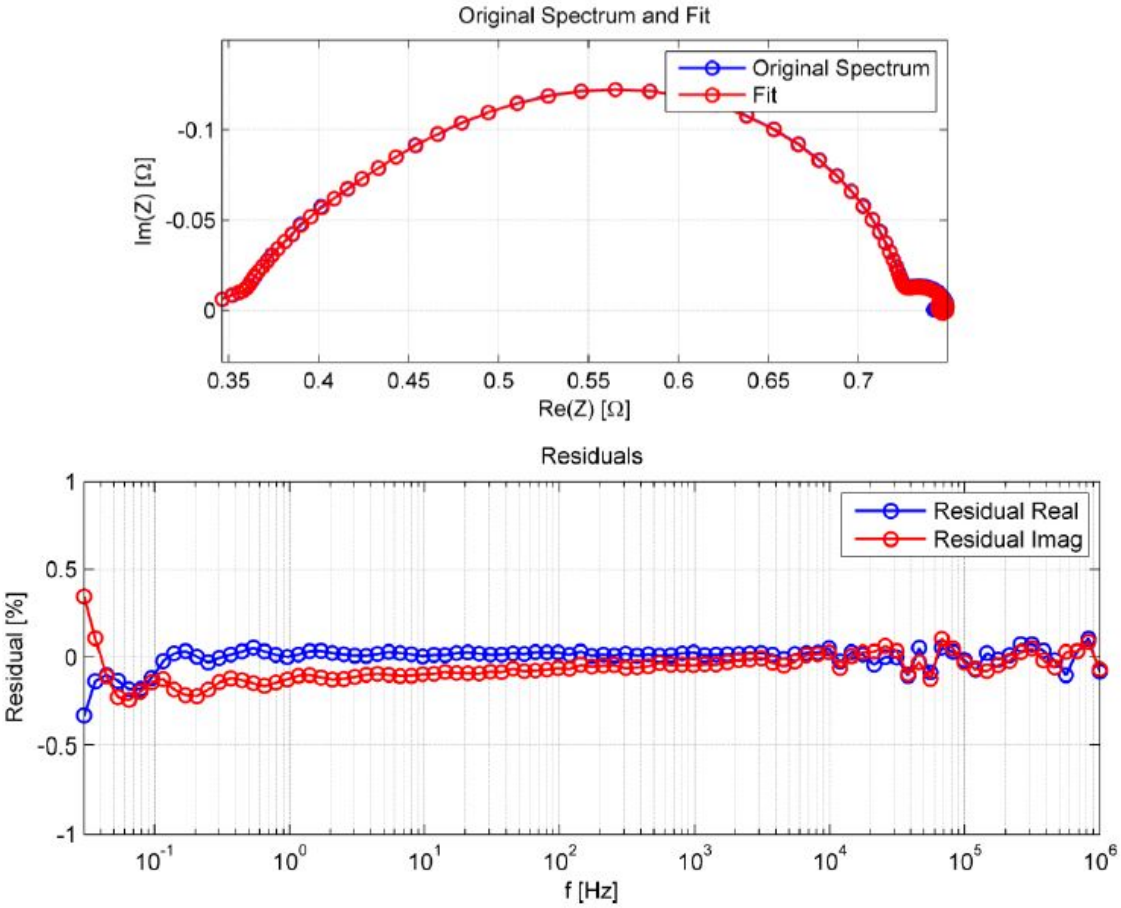

FIGURE 2.14: Invalid spectrum (time-variance) of a symmetric Anode-Anode Solid Oxide Fuel cell (SOFC). The residuals are weakly biased towards the low frequencies over a broad range. This indicates time-variance and thus an KK-incompliant spectrum. Here, the spectrum was measured at the activation phase of the SOFC, and the properties of the Anode changed during the measurement. Taken from [74]

2.4 Equivalent circuit modelling

The impedance response of a complex system can be reproduced by a combination of ideal and non-ideal circuit elements, resembling physical electrical and electrochemical processes. By fitting the impedance data to this equivalent circuit model (ECM), the physical processes can be quantified. The advantage of this approach lies in rapid comparison and quantification of different impedance spectra. The disadvantage lies in posing a physical relevant model a priori to the impedance measurement, so that physical relevant parameters can be extracted. If a physical relevant model is apparent, then carrier diffusion constants and recombination and mobility rates can be quantified. ECM can also be used to study stability (aging and degradation) of the sample [33].

In fitting the impedance spectrum to an ECM, the model is fit to the impedance spectrum as a whole rather than to a specific impedance attribute. Therefore, the fit of for example the high-frequency part is influenced by the goodness of fit of the low-frequency part, because the algorithm tries to minimise the error between fit and measurement over the full range. Thus the fit parameters of different impedance attributes are co-dependent on each other.

A poor fit indicates an unsuitable model, Kramers-Kronig (KK) incompliance [33] or bad signal to noise ratio. To compose a suitable model, an extra circuit component may only be added if it increases the quality of fit (decreasing χ^2) by a factor of 10. An acceptable χ^2 is smaller than 10^{-3}, and preferably in the range of 10^{-6} [75, 76]. A poor fit may also indicate KK-incompliance, as the data may be influenced by external parameters (violation of the *causility* criterion) or by a change in the conductivity of the sample due to a chemical reaction (violation of the *stability* criterion), or violation of the other requirements. Additionally, if the signal to noise ratio is low, measurement noise also leads to poor quality of fit.

2.4.1 Equivalent circuit models for PSCs

In the case of PSCs, many models have been proposed. A few of the models are outlined in Figure 2.15. The different models are currently used to describe different impedance attributes of PSCs when they occur in the impedance response, but a full comprehensive model describing PSC behaviour across all conditions is lacking.

The impedance response of PSCs shows two main semi-circles or arcs, plus potential additional features such as loops or negative values for reactance, indicating inductance [44]. The first semi-circle is present at high frequencies (>10 kHz), the second at low frequencies (<100 Hz). There is no agreement among researchers about the physical origin of the semi-circles, though for the high-frequency semi-circle there is a tendency to a common explanation: the capacitance of the high-frequency semi-circle could be attributed to the geometrical capacitance of the device, and the resistance could be attributed to either transport or recombination resistance (this is under debate) [44]. Both transport and recombination resistance depict the physical phenomenon of resistance of charges through the device, whether it is caused by the contact layer resistance or through recombination, effectively decreasing conductivity. The explanations for the low-frequency semi-circle and the additional features are more speculative. Both low and high frequency semi-circle change uniformly for a change in operating conditions such as light intensity or voltage, making a comparison difficult. In addition, though ion migration is shown to occur in PSCs [19], a study that clearly relates ion migration to electrically measurable quantities is still missing [44]. Without agreement on the physical origin of the main and additional features of the impedance response of PSCs, a full comprehensive model describing PSC behaviour is still missing. Four additional equivalent circuit models from literature are presented in Figure 2.16, showing how physical processes and parameters are attributed to electrical components in various configurations.

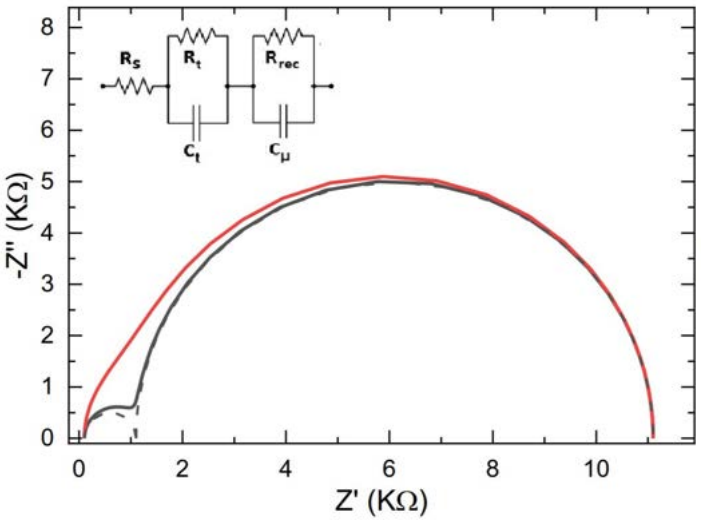

(A) ECM to describe two relaxation processes with distinct time-scale (black) or similar time-scale (red). The first relaxation denotes transport resistance and capacticance R_t and C_t of charge carriers, the second recombination resistance R_{rec} and chemical capacitance C_μ, describeing the generation and recombination of photo-generated charge [33].

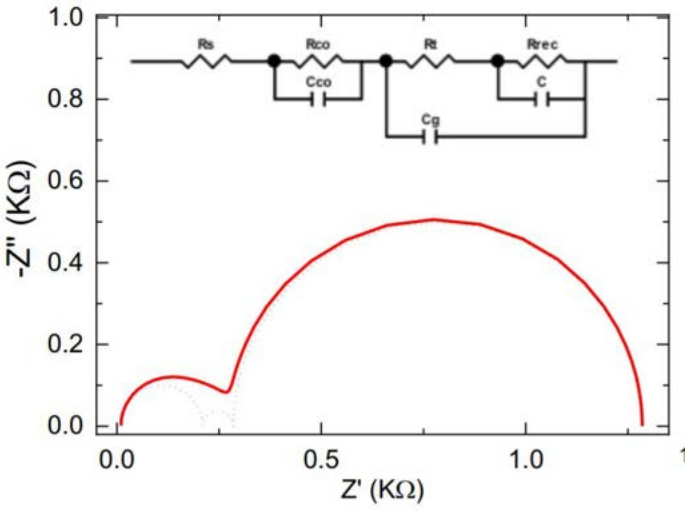

(B) ECM model containing an extra RC circuit to describe the impedance response of a bad interface (non-Ohmic), such as a Schottky junction. In the JV-characteristics a S-curve would show when this is the case. From the voltage dependence of the new RC-circuit the interface can be characterised as insulating or as a recombination site.

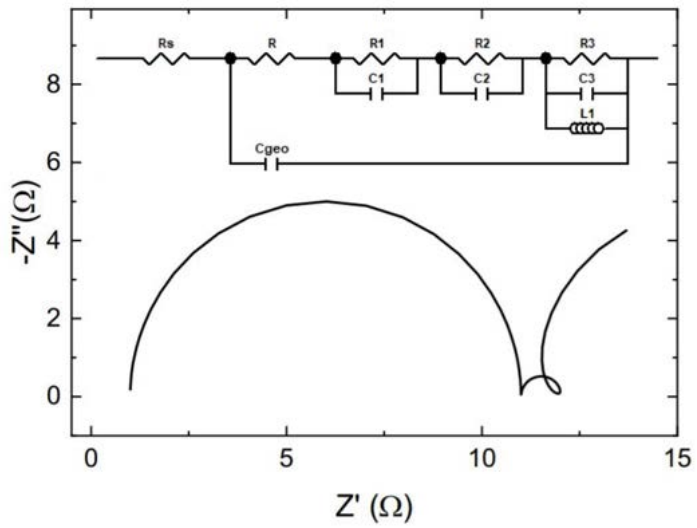

(C) ECM to model an inductive effect showing up in middle-low frequencies. This atypical behaviour is sometimes seen in the impedance response of PSCs and produces a loop in the Nyquist plot.

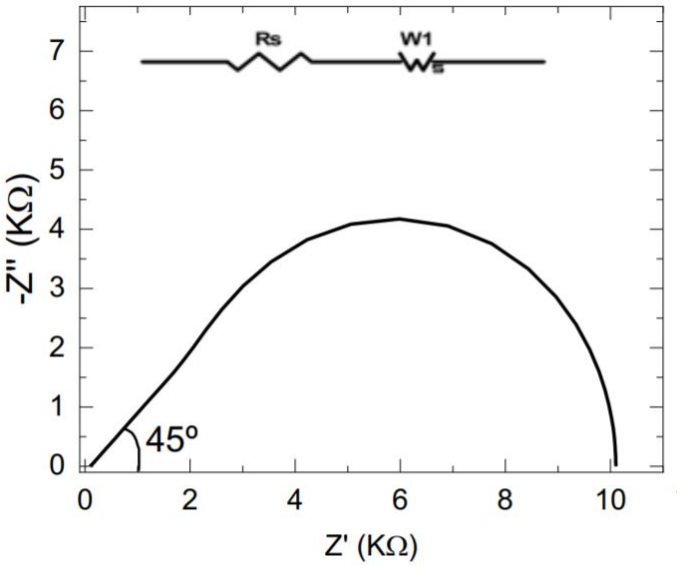

(D) ECM to model organic solar cells (OSCs) in which electron and hole mobilities (transport resistance) in the active layer is the limiting factor. This produces a slope of about 45° in the Nyquist plot at high frequencies. In the case of PSCs, this Warburg like behaviour shows up in low frequencies and indicates ion transport [33].

FIGURE 2.15: Equivalent circuit models for PSCs for fitting of IS data under light conditions. Components indicate physical processes. Circuits and simulations taken and adapted from [30].

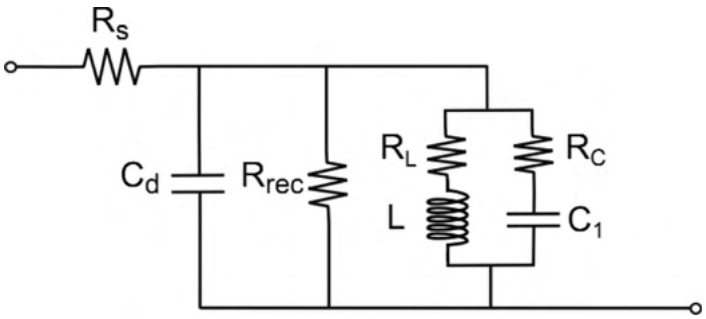

(A) Model by Bisquert et al. for PSCs with large ionic and electronic charge accumulation at the external contact interface. Here, R_s is the series resistance, C_d is the dielectric capacitance, R_{rec} is the recombination resistance, R_L is the series resistance along with the inductance L and R_C is the series resistance along with the surface charging capacitance C_1 [77].

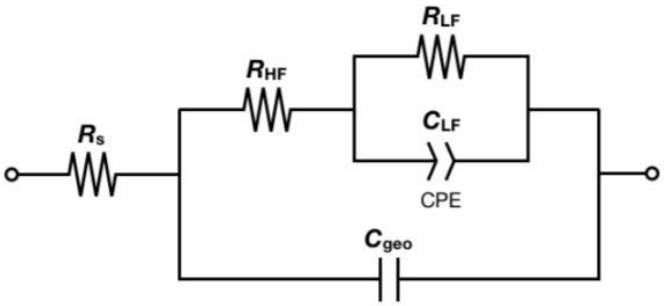

(B) Nested equivalent circuit model to model both the High Frequency (HF) and Low Frequency (LF) response of PSCs. Here R_s is the series resistance formed by the electron and hole transport layers and contacts, R_{HF} the high-frequency resistance (usually shunt or recombination resistance), C_{geo} the geometrical capacitance, R_{LF} the low frequency resistance and C_{LF} the low frequency capacitance [35].

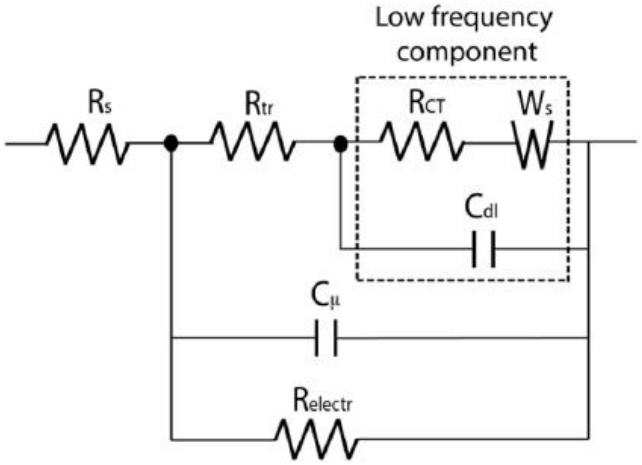

(C) ECM model for PSCs describing combined electric and ionic conduction. Here, R_s is the series resistance, R_{tr} the charge and ion transport resistance coupled with interfacial charge transfer resistance R_{CT}, C_μ is the chemical capacitance denoting stored charge in the perovskite bulk, R_{electr} denotes free carrier (electron/hole) recombination and transport, C_{dl} denotes ion accumulation at the interface and W_S denotes mass (ion) transport [34].

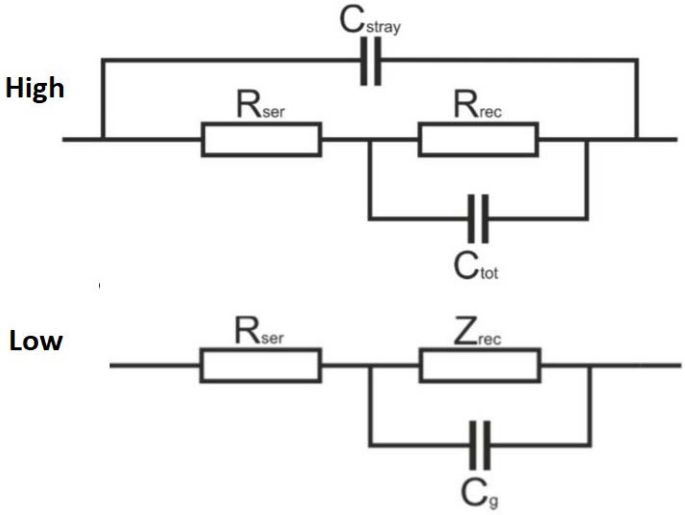

(D) Two separate ECM's to model the high and low frequency response of PSCs. The ECM for the high frequency response contains a series resistance R_ser attributed to the resistance of the transparent electrode, a voltage-dependent recombination resistance R_{rec}, a combined capacitance C_{tot} of both geometrical capacitance (charge stored in contacts) and chemical capacitance (photogenerated charge), and a capacitor for stray capacitances associated with contacts C_{stray}. The ECM for the low frequency response contains a series resistance, a geometrical capacitance and a frequency dependent recombination resistance Z_{rec}. At high frequencies, Z_{rec} can be replaced with R_{rec}, as at high frequency the recombination resistance is not influenced by ionic movement [68].

FIGURE 2.16: Additional equivalent circuit models from literature describing Perovksite solar cell device behaviour, using different components in different configurations attributed to various physical processes and parameters.

Chapter 3

Methods

3.1 Sample design and preparation

Perovskite solar cells consist of a photo-absorber layer, an electron/hole transport layer and various other layers which improve charge extraction energetics and/or improve attachment of the layers. The devices in this thesis are built conform the p-i-n (inverted) structure, meaning that solar irradiation passes through the transparent electrode and HTL before reaching the photo-active persovskite instead of passing through the transparent electrode and ETL. The several layers are presented in Figure 3.1. In this figure, Indium Tin Oxide (ITO) is a transparent electrode, PTAA is the hole transport layer, PFN increases the wettability of hydrophobic PTAA to hydrophilic perovskite, PCBM and BCP form the electron transport layer, and chromium (oxide) is an adhesive layer for the gold electrode. The various layer thicknesses are indicated. Each sample has 6 smaller areas called *pixels*, indicated in 3.1b. Each pixel is a small solar cell. The division in 6 pixels is beneficial because the probability that a small area of the solar cell is of good quality is larger than the probability of the entire cell being of good quality. To contact the ITO transparent electrode, the various solar cell layers are scratched away using a spatula until the harder ITO is reached. The samples have been received from collaboration partners at Imperial College London. The details on the experimental procedure for sample fabrication can be found in Appendix A.1. See Appendix A.2 for experimental work and sample making carried out by me at AMOLF institute for physics of functional complex matter.

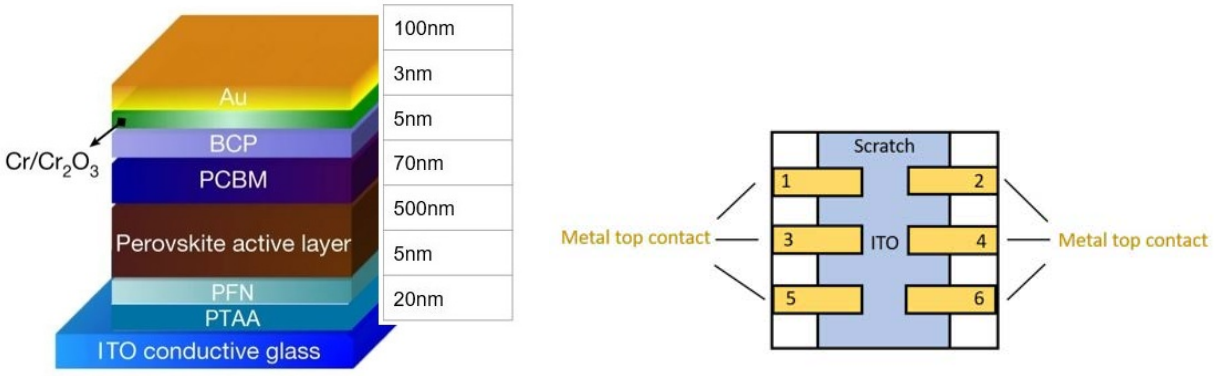

(A) Solar cell layers

(B) Sample architecture

FIGURE 3.1: Sample architecture with layer thicknesses. The device has an inverted structure of p-i-n, where p is the HTL formed of PTAA (20nm), i is perovskite (500nm) and n is the ETL formed of PCBM/BCP (75nm). The perovskite active layer is constituted of $MaPbI_3$ or $Ma_{0.95}Ga_{0.05}PbI_3$ or $Ma_{0.95}Fa_{0.05}PbI_3$. One sample contains six separate pixels. At the top of the sample the various solar cell layers are scratched away with a spatula until the harder ITO is reached. Such, a pixel can be contacted to the metal top contact and to the ITO.

3.2 Measurement setup for electrical measurements

3.2.1 Current-Voltage Characteristics

The measurement setup for JV-measurements comprises a solar simulator, sample holder, a Keithly 2400 power source and digital multimeter, and custom CPU software to operate the Keithly 2400 and apply measurement settings for JV-scans. For JV-measurements, the sample holder was connected to the Keithly 2400 which applies the voltage sweep and measures the current output. The solar simulator has a Xenon Arc lamp and contains an AM1.5G air mass filter to account for atmospheric absorbance of parts of the solar spectrum.

3.2.2 Impedance Spectroscopy

The Impedance Spectroscopy setup contains a MFIA Impedance Analyser from Zurich Instruments, sample holder and solar simulator. The MFIA Impedance Analyser has a frequency range from $1mHz$ to $5MHz$, a basic of 0.05%, and a LabOne sweeper tool for frequency, bias voltage, and test signal amplitude response measurements [78]. The MFIA is contacted to the Device Under Test (DUT) using as-short-as-possible cables to prevent cable inductance at high frequencies. The H_{CUR} terminal provides the small alternating AC current plus optional DC bias voltage (see Figure 3.2). The current is measured at the L_{CUR} terminal. The DUT is connected in two-point measurement configuration. In this configuration, the impedance is measured as the drive voltage divided by the measured current. This assumes that the voltage drop over the DUT is equal to the drive voltage, which is indeed the case for high-impedance DUTs. In the four-point measurement, two extra contacts at the DUT are used to measure the voltage drop over the DUT. Two-point measurement is advantageous because it eliminates stray capacitances and leakage currents parallel to the DUT [79]. Impedance measurements under dark conditions have been carried out using a Faraday cage to eliminate influences of external electric fields, which is necessary because of low amounts of charge carriers in the dark under low bias voltage (low signal to noise). Under illumination conditions, the Faraday cage was removed to prevent sample heating. Additionally, the room was equipped with air conditioning to provide stable ambient temperature. Here, the sample is positioned in such a way that the incident solar irradiation is $100mW/cm^2$, confirmed by measurements with the silicon reference solar cell. The MFIA was operated using it's own on-board software system LabOne, which was accessed through a direct LAN connection and the browser of a computer. Impedance spectra were checked for Kramers-Kronig compliance using the Lin-KK software tool [74] and fitted with equivalent circuit modelling using ZView software from Scribner Associates.

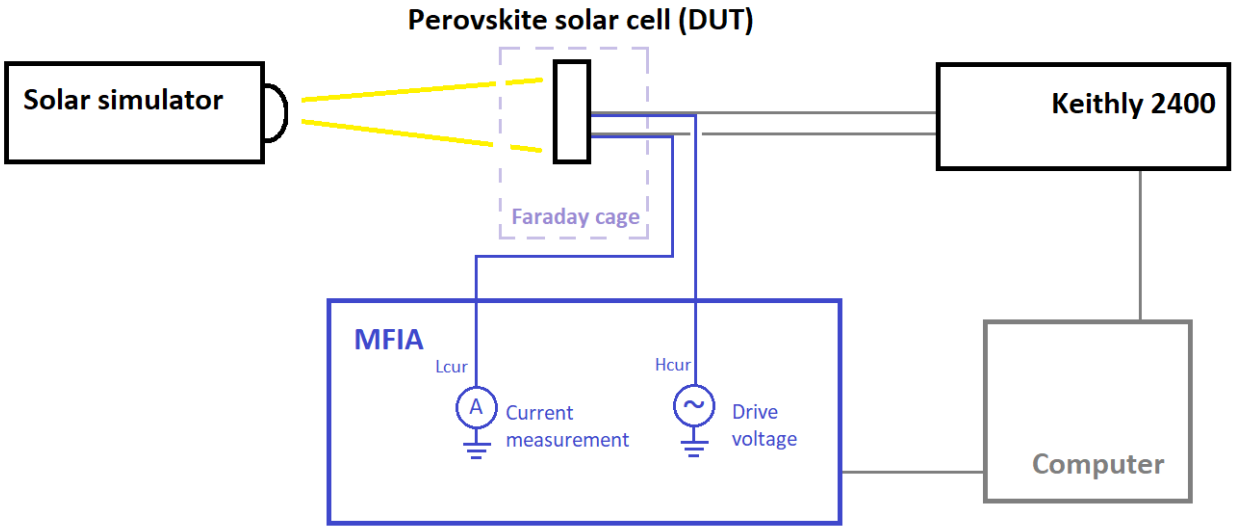

FIGURE 3.2: Two-point measurement configuration of perovskite solar cell (DUT) to the MFIA Impedance Analyser for impedance spectroscopy measurements and connection to the Keithly 2400 for taking JV-characteristics. The Faraday cage is present for measurements in dark conditions to prevent external electric influences and is absent for measurements under illumination condition to prevent sample heating. The solar simulator has a Xenon arc lamp and an AM1.5G air mass filter.

3.3 Experimental data collection

JV-characteristics were taken using the sample holder, Keithly 2400 and solar simulator. The JV-characteristics were taken using a voltage scan rate of $50mV/s$ from -0.3V to 1.3V and reverse. For illumination JV-characteristics, the sample is positioned in such a way that the incident simulated solar irradiation is $100mW/cm^2$, confirmed by measurements with the silicon reference solar cell certified by NREL. In the case of PSCs, JV-characteristics depend on variables such as voltage scan speed and light soaking, which is why both forward (fwd) and reverse (rev) scan direction were performed. The JV-characteristics were taken prior to the impedance measurements. To check if the impedance measurements influence the solar cell performance, JV-characteristics were taken in between impedance spectroscopy sessions.

Impedance measurements were carried out using the sample holder connected to the MFIA with LabOne software. A $20mV$ perturbation AC signal superimposed on a constant DC bias voltage was used. The frequency of the perturbation signal was swept from high frequency (10^6Hz) to low frequency (1Hz). This is because mass transport (ion migration) happens in the low frequency regime and may change the device. By scanning from high to low frequency, the sample is perturbed as little as possible when the measurement progresses. For measurements under dark conditions the Faraday cage was used, but not under light conditions to prevent sample heating.

Two different batches of solar cells have been measured, generating two different datasets. In the first dataset, measured in cooperation with Dr. Thomas Macdonald from Imperial College London, three perovskite solar cells were measured differing in their active layer composition. These solar cells are labelled MAPI2, MAGA and MAFA, where the first is a standard $MaPbI_3$ solar cell and the last two devices are multi-cation PSCs ($Ma_{0.95}Ga_{0.05}PbI_3$ and $Ma_{0.95}Fa_{0.05}PbI_3$). In the second dataset, made by Mr. Richard Pacalaj at Imperial College London in collaboration with Dr. Thomas Macdonald, three $MAPbI_3$ solar cells were measured. The cells in the first round of measurements contain repetitions to check for stability, the cells in the second round of measurements are taken at various bias voltages to check for any voltage dependent processes.

Chapter 4

Results

4.1 Factors influencing KK-compliance and extraction of time-constants

4.1.1 Solar cell performance

The solar cell performance of four pure $MaPbI_3$ solar cells was measured by taking the current-voltage (JV) characteristics of the solar cell, both in the dark and in the light under 1 sun illumination. The JV-characteristics are presented in Figure 4.1 and the extracted material parameters are presented in Table 4.1. It is important to notice that $MAPbI_3$-d103 shows hysteresis in the dark, whereas this is not the case in the light (or only is very slightly). JV data under illumination for $MAPbI_3$-Fresh is lost, though the cell performed similar to the other devices.

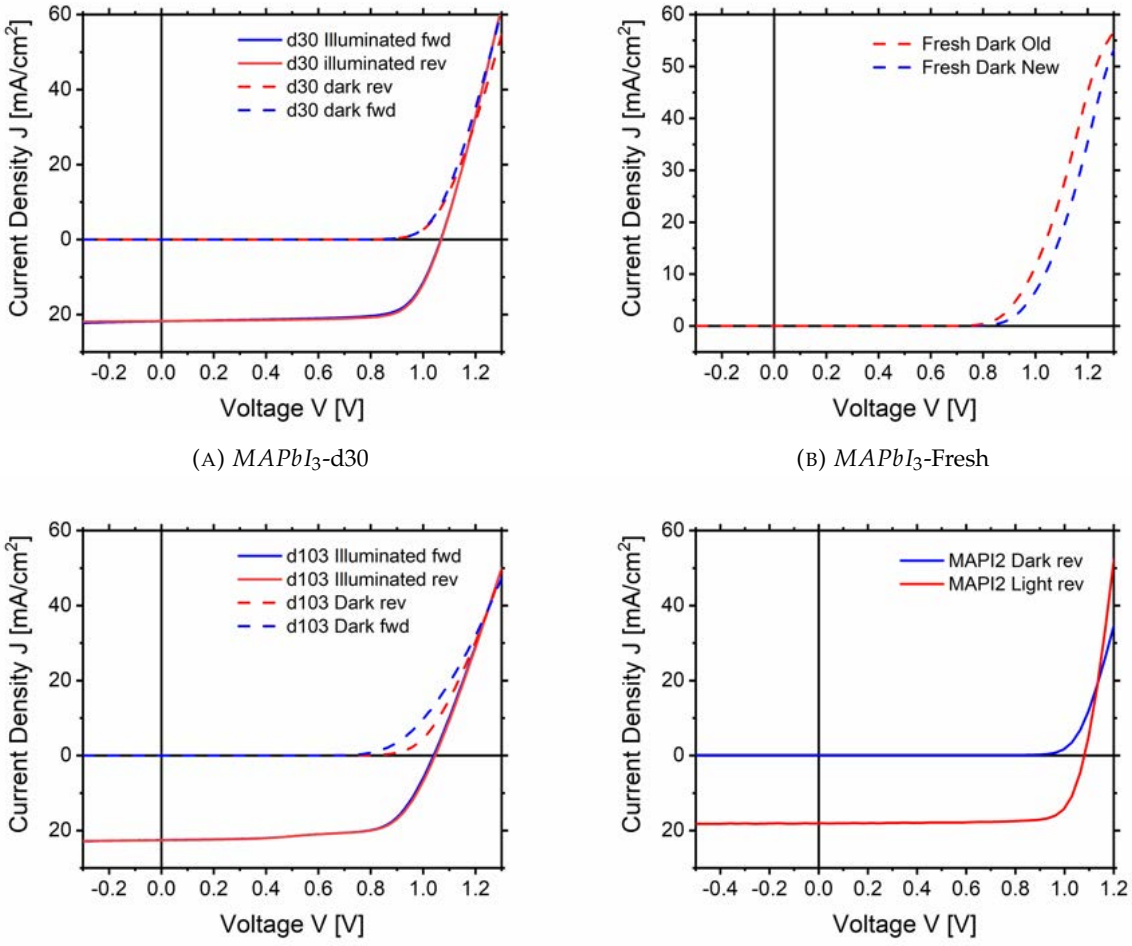

(A) $MAPbI_3$-d30

(B) $MAPbI_3$-Fresh

(C) $MAPbI_3$-d103

(D) $MAPI2$

FIGURE 4.1: Current-voltage characteristics of $MAPbI_3$ perovskite solar cells $MaPbI_3$-d30 (a), $MaPbI_3$-Fresh (b), $MaPbI_3$-d103 (c) and MAPI2 (d) under dark and under light conditions. For $MaPbI_3$-Fresh and $MaPbI_3$-d103 under dark conditions hysteresis is shown between forward and reverse scan direction. $MaPbI_3$ shows both a series (slope at V_{oc}) and shunt resistance (slope at J_{sc}) in the JV-curve.

TABLE 4.1: Solar cell performance parameters of MAPI-d30, MAPI-d103 and MAPI2. The devices have similar efficiency and V_{oc}. The Fill Factor of MAPI-d103 is smallest due to both a small series and shunt resistance, but it has the highest photo-generated current.

Device	**Jsc (mA/cm2)**	**Voc (V)**	**FF**	**MPP (V)**	**PCE (%)**
MAPI-d30	21.7	1.07	0.80	0.88	17.5
MAPI-d103	22.6	1.05	0.69	0.83	16.2
MAPI2	20.7	1.04	0.77	0.93	16.6

4.1.2 IS data representation and Kramers-Kronig compliance

In this section, data is represented using Nyquist plots, and the results from the Kramers-Kronig compliance test are presented using Residual plots. First, the Nyquist and Residual plots for $MaPbI_3$ solar cells under dark conditions are presented in Figure 4.2 and Figure 4.3, then under light conditions in Figure 4.4. If the low-frequency data of IS spectra is removed, this has consequences for the KK-compliance. This is discussed directly after the full-data presentation in Figure 4.5. Data representation by Nyquist plots and KK-analysis by Residual plots are presented together to show sample to sample variation.

Dark conditions Nyquist and KK-residual plots for MAPI

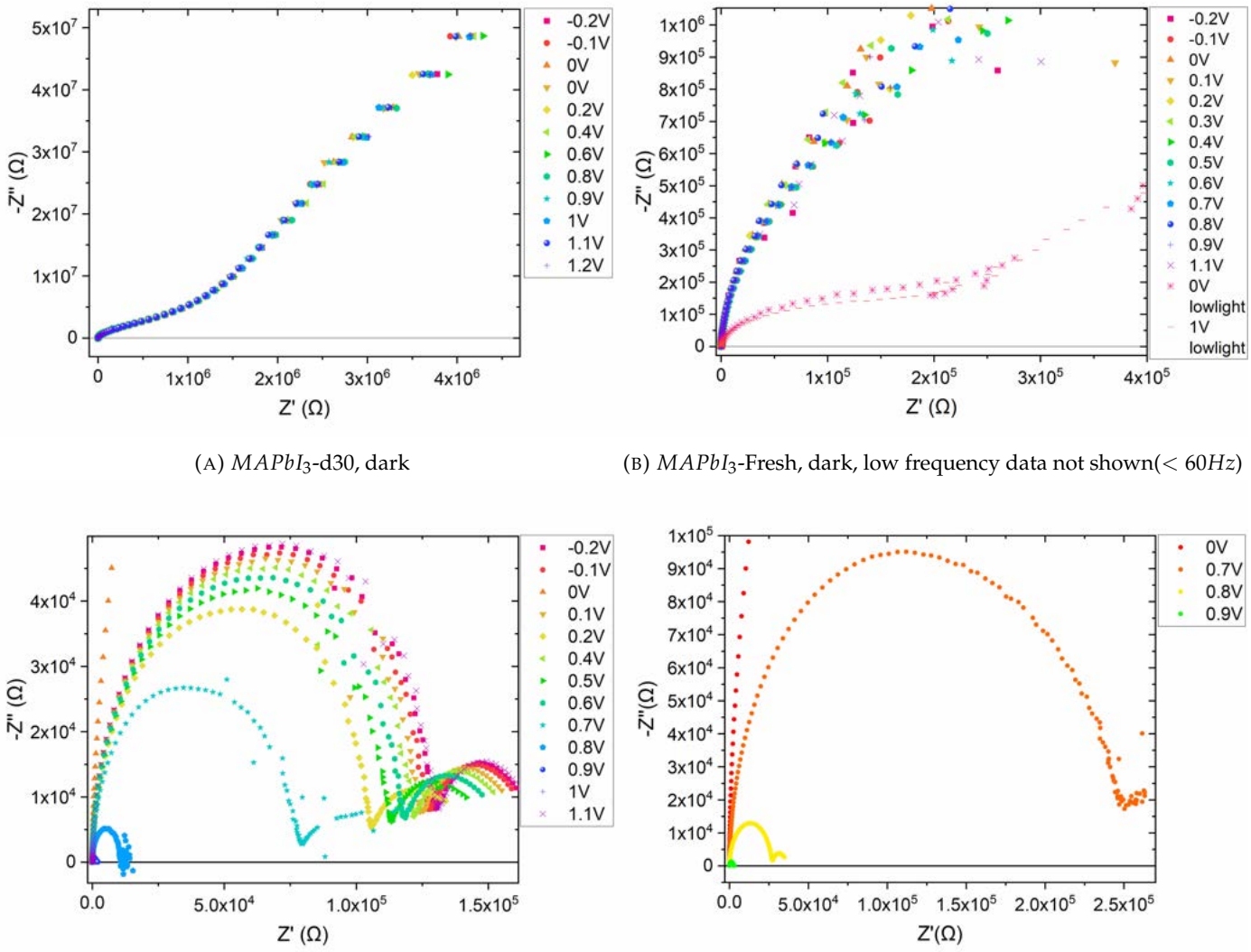

(A) $MAPbI_3$-d30, dark

(B) $MAPbI_3$-Fresh, dark, low frequency data not shown($< 60Hz$)

(C) $MAPbI_3$-d103, dark

(D) $MAPI2$, dark

FIGURE 4.2: Nyquist plots of $MAPbI_3$ solar cells in the dark under various bias voltages. $MAPbI_3$-Fresh includes two test measurements under low illumination.

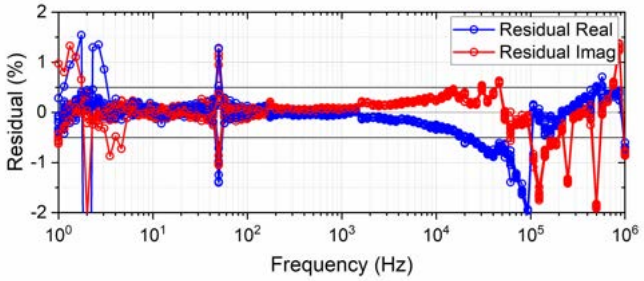

(A) $MaPbI_3$-d30, Dark, all bias voltages

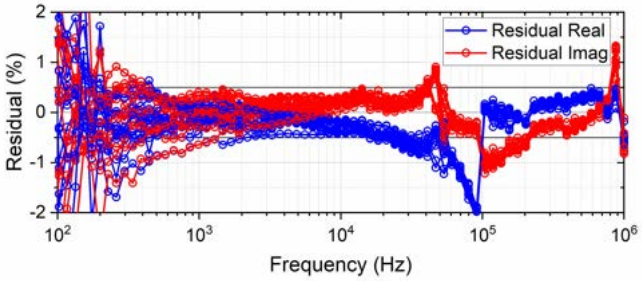

(B) $MAPbI_3$ Fresh, Dark, all bias voltages. Residuals below 100Hz show only noise

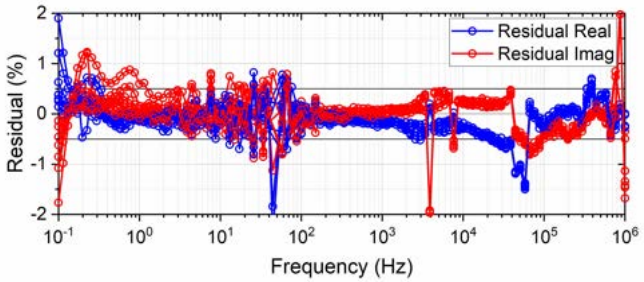

(C) $MaPbI_3$-d103, Dark, all bias voltages except 0.7-1.0V (see Figure B.1a in Appendix B.2)

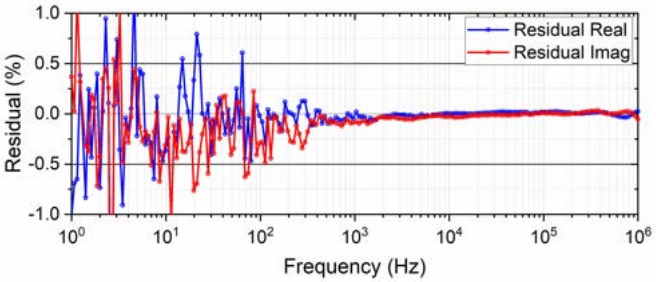

(D) $MAPI2$, Dark, 0.7V (compliant). Vertical axis is stretched to better evaluate KK-compliance. Residual plots of bias voltages 0.8V and 0.9V (evaluated incompliant) are shown in Figure B.2a in Appendix B.2.

FIGURE 4.3: Kramers-Kronig residual plots for Impedance Spectroscopy data of four $MAPbI_3$ solar cells in the dark for bias voltages of -0.2V to 1.1V. The data should present a straight line within the $\pm$ 0.5% border to be Kramers-Kronig compliant and of good quality. Systematic bias is shown for all the residuals, mainly at higher frequencies except for MAPI2 0.7V. The level of noise in lower frequencies differs greatly per sample.

Illumination condition Nyquist and KK-residual plots for MAPI

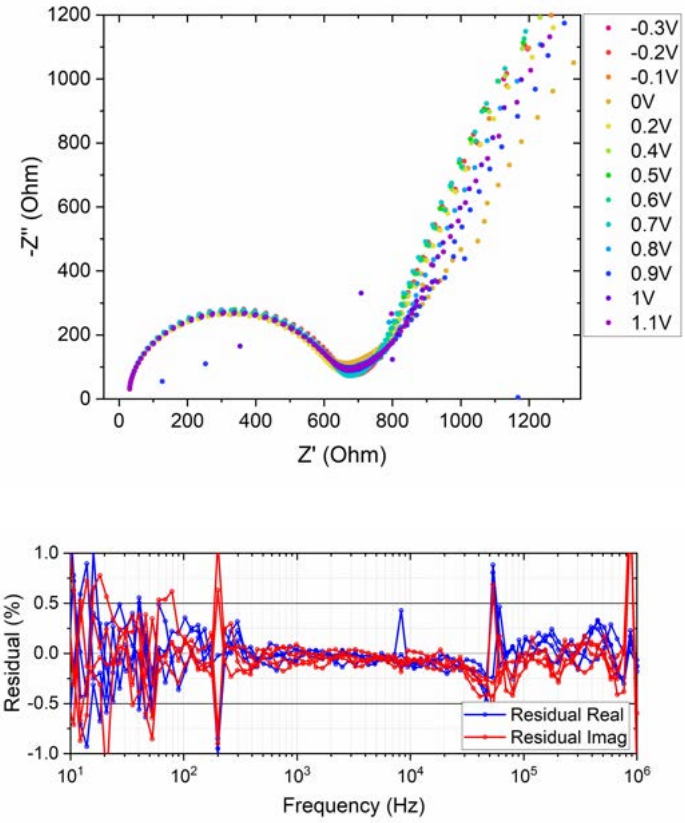

(A) Nyquist plot (top) and KK residuals plot (bottom) of illuminated $MAPbI_3$-d103. Frequency range $10^6 - 10Hz$. Low frequency data not shown due to noise ($< 10Hz$). The residual plot contains only KK-compliant evaluated spectra. These compliant spectra comprise the bias voltages -0.3V,-0.1V, 0.4V and 0.6V. Other bias voltages are evaluated KK-incompliant (see Figure B.1b in Appendix B.2).

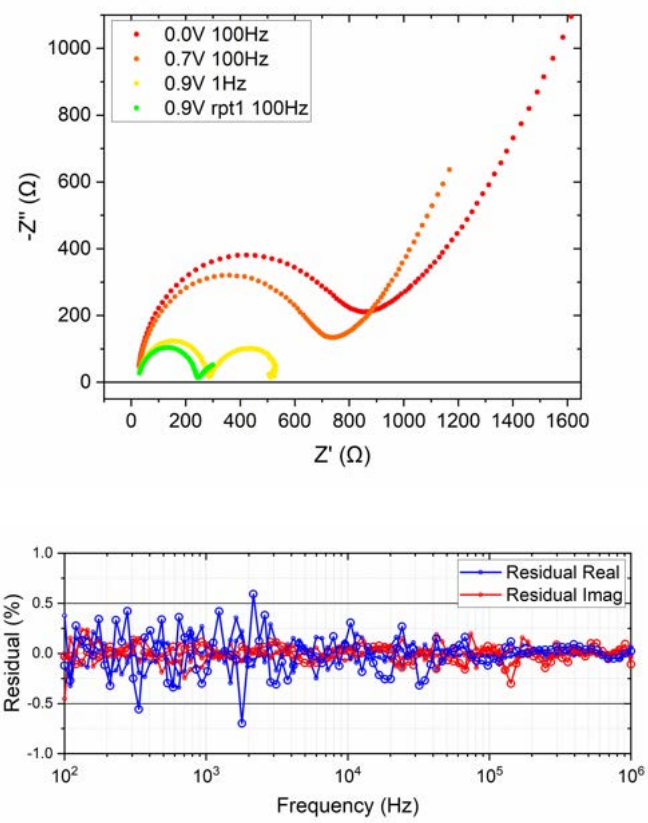

(B) Nyquist plot (top) and KK residuals plot (bottom) of illuminated $MaPI2$. The residual plot contains only KK-compliant evaluated spectra. The bias voltages included are 0V, 0.7V and 0.9V rpt1. Residual plot for 0.9V is found in Figure B.2b in Appendix B.2.

FIGURE 4.4: Nyquist and Kramers-Kronig residuals plots of illuminated $MAPbI_3$-d103 and $MAPI2$ solar cells. The data should present a straight line with no bias to be Kramers-Kronig compliant. The vertical axes of the residual plots are stretched to $\pm 1\%$ to show no systematic bias is present. The residuals lay within the $\pm$ 0.5% border, which indicates the spectra are of good quality.

Comparing the residual spectra displayed in Figure 4.4, both samples contain spectra with residuals lying approximately within the $\pm 0.5\%$ border, indicating spectra of good quality. In addition, the spectra show no systematic bias meaning the real and imaginary part of the residuals do not deviate from each other over several frequency decades. No measurements under illumination condition were performed for the samples MAPI-d30 and MAPI-Fresh. To summarise which spectra are compliant on the full available frequency range:

- Dark: MAPI2 0.7V is compliant
- Light: MAPI2 bias voltages 0V, 0.7V and 0.9V rpt1 are compliant
  d103 bias voltages -0.3, -0.1, 0.4 and 0.6V are compliant

Kramers-Kronig compliance of spectra without low frequencies (<100Hz)
The Kramers-Kronig test has been repeated for MAPI-d103 and MAPI2 for only mid- and high-frequency range. Here, all impedance data corresponding to frequencies of 100Hz and lower has been removed, to see if this influences the KK-compliance for the spectra. The results are displayed in Figure 4.5, which displays the Nyquist plots and KK-residual plots for the compliant evaluated spectra.

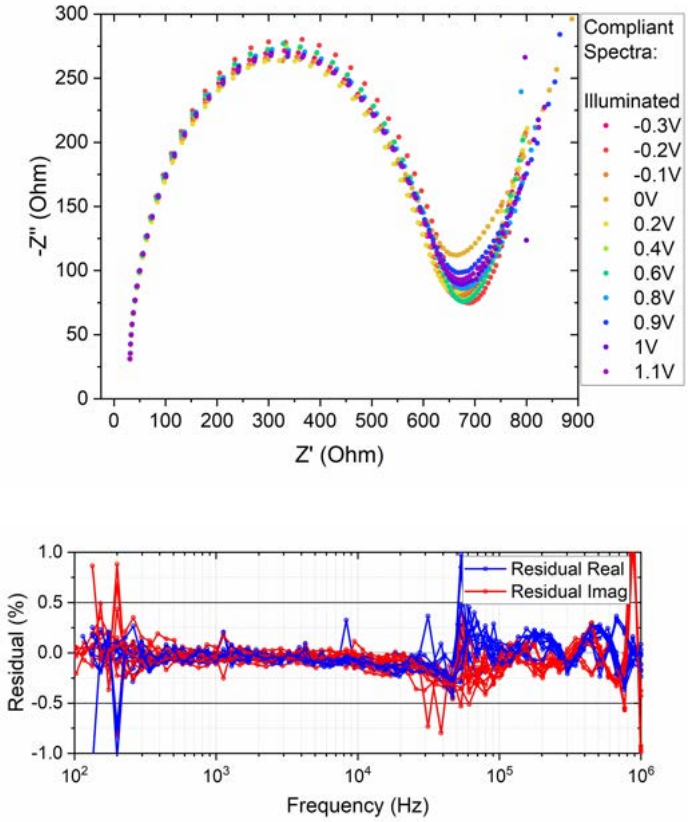

(A) Nyquist plot (top) and KK residuals plot (bottom) of KK-compliant spectra of $MAPbI_3$-d103, without low frequencies (<100Hz). These compliant spectra comprise all bias voltages except 0.5V and 0.7V (see Figure B.3 in Appendix B.2).

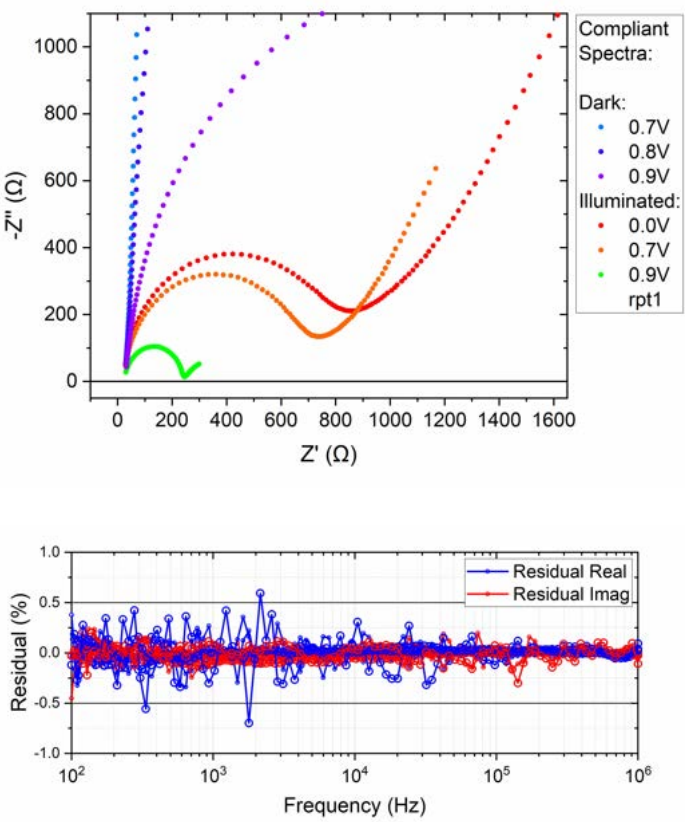

(B) Nyquist plot (top) and KK residuals plot (bottom) of KK-compliant spectra of illuminated $MaPI2$, without low frequencies (<100Hz).

FIGURE 4.5: Nyquist and Kramers-Kronig residuals plots of illuminated $MAPbI_3$-d103 and $MAPI2$ solar cells.

Summary of compliant spectra for dark and illumination condition
In Table 4.2, the KK-compliant spectra of the pure MAPI cells MAPI-d30, MAPI-Fresh, MAPI-d103 and MAPI2 are summarised. The full frequency measurement range of the spectra was from 10^6 to 1Hz, after which the KK-compliance of the spectra was checked. Then, the low frequency data below 100Hz was removed and the remaining spectrum was checked for KK-compliance again to see if the frequency range looked at makes a difference for the KK-compliance. The KK-compliant spectra over the full frequency range are shown on the left, the KK-compliant spectra over the frequency range down to 100Hz are shown on the right.

TABLE 4.2: Kramers-Kronig compliant spectra of four MAPI cells under dark and light conditions for two tested frequency regions

	Freq. Range 10^6 - 1Hz		Freq. Range 10^6 - 100Hz	
Device	**Dark**	**Light**	**Dark**	**Light**
MAPI-d30	-	-	-	-
MAPI-Fresh	-	-	-	-
MAPI-d103	-	-0.3V, -0.1V, 0.4V, 0.6V	-	-0.3V-0V, 0.2V, 0.4V, 0.6V, 0.8V-1.1V
MAPI2	0.7V	-	0.7-0.9V	0V, 0.7V, 0.9V rpt1

From Table 4.2, it shows that more spectra are compliant when low frequencies (<100Hz) are removed. This is mainly due to time-variance (systematic bias) in the residuals and to less extent due to noise, as can be observed from comparing the associated residual plots here and in Appendix B.2. The compliant spectra listed above will be modelled in the next section with equivalent circuit modelling to extract time-constants.

4.1.3 Factors impacting Kramers-Kronig compliance

Very few spectra are evaluated compliant. Thus it is investigated under which conditions the spectra are (in)compliant. This is checked by 1) varying the illumination, 2) varying the voltage, 3) varying the frequency range looked at and 4) evaluating if repeated measurements under the same conditions lead to consistent (in)compliance. The incompliance is assessed by noise (residuals bigger than 2%), and by extent of time-variance (X for maximum bias of 0.4%, x for maximum bias of 0.2%). This has been assessed dividing the spectrum up in high, mid and low frequency range, based on distinctive regions in the residual plots. Taking distinctive regions into account is important as the residuals of a frequency decade are co-dependent on the residuals in neighboring decades (due to fitting by the Lin-KK tool prior to calculating residuals).

Additionally, two ways of operating the Lin-KK tool have been assessed, to check for correct results. The Lin-KK test performs first a fit of the impedance spectrum with a series of RC-circuits to account for the mathematical frequency range of $-\infty$ to ∞, which is impossible for real-life measurements. Thereafter, it calculates the residuals. Outlier datapoints impact the KK-compliance through disturbing the fit from which the residuals are calculated. This may result in apparent KK-incompliance. Those outlier datapoints can be caused by a glitch in the instrument current range, or due to too low sample conductivity at low frequencies, leading to low-signal to noise. See Example 4 in Appendix B.1 for an example of this from the Lin-KK operating guide. Because outlier datapoints influence the KK-compliance to great extent, two types of analysis are carried out: one in which outlier datapoints are present, and one in which outlier datapoints are freely removed. See section B.3 for full analysis and extended data tables. The tables are placed below each other to make it apparent what difference removing outlier datapoints makes to the extent of time-variance in the residual plots. This analysis is presented only for $MAPbI_3$-d103 and MAPI2, as those cells are the only cells with Kramers-Kronig compliant spectra. The conclusions on factors that impact Kramers-Kronig compliance are listed in the table below. Take note that for MAPI2 High, Mid and Low frequencies are defined as $10^6 - 10^4 Hz$, $10^4 - 10^2 Hz$, $10^2 - 10^0 Hz$ respectively, whereas this is $10^6 - 500 Hz$, $500 - 10 Hz$, $10 - 0.1 Hz$ for MAPI-d103. The ranges are chosen different due to different attributes in the residual spectra for the cells denoting compliant and incompliant regions. The Lin-KK test is very sensitive to KK-incompliant data, meaning that if a KK-incompliant region is present, this has influence on the assessment of compliant regions due to the associated fitting problem.

TABLE 4.3: Factors impacting KK compliance (Impact/no impact). Impact is indicated as an 'X', no impact is indicated as an '-' and lack of data is left blank. For MAPI2 High, Mid and Low frequencies are defined as $10^6 - 10^4 Hz$, $10^4 - 10^2 Hz$, $10^2 - 10^0 Hz$ respectively. For MAPI-d103 High, mid and low frequencies are defined as $10^6 - 500 Hz$, $500 - 10 Hz$, $10 - 0.1 Hz$ respectively. The ranges are chosen different due to different attributes in the residual spectra for the cells.

	MAPI2 (incl repeat measurements)		*$MaPbI_3$*-**d103 (no repeat measurements)**	
	IMPACT?	**Comment**	**IMPACT?**	**Comment**
Illumination	-		X	*Only illuminated spectra are compliant*
Voltage	-		-	
Frequency Region (FR) looked at	-		X	*Dark: Low + Mid FR more compliance* *Light: Mid + High FR more compliance*
Consistency	X	*Repeated measurements under the same conditions are sometimes compliant and sometimes incompliant*		
Cut low frequencies <100Hz out	Dark: X Light:	*Dark: Higher Freq more compliance* *Light:*	Dark: - Light: X	*Dark: no impact* *Light: Mid and High F more compliance*

From this table it becomes apparent which factors impact the KK-compliance of the spectra of both MAPI cells. First, it is good to observe that which factors impact the KK-compliance are greatly dependent on the sample. Only the impact assessment of bias voltage is found to be congruent across both cells (indicating bias voltage does not influence KK-compliance). The impact of the other parameters differs per sample. Illumination impacts the KK-compliance for MAPI-d103, as only illuminated spectra are compliant. For MAPI2 this is not the case. KK-compliance (absence of time-variance) differs per frequency region for MAPI-d103 only, where low to mid frequency region are more often KK-compliant and in the light mid and high-frequency region are more often compliant. Repeated measurements on MAPI2 using the same measurement parameters and keeping all conditions constant results in some cases in incompliance and in some cases in compliance. Therefore, an unknown variable underlies the change in KK-compliance. Finally, cutting low frequency data (<100Hz) out has a different impact on both cells as well: for MAPI-d103 in the dark it makes no difference, whereas it does in the light conditions.

Additionally, based on evaluation experience, it is suspected that cutting an impedance spectrum does not yield the same KK-compliance result as measuring the sample over a shorter frequency range. For repeated measurements on MAPI2 in light conditions, the 0.9V repeated measurement on a shorter frequency range is compliant, whereas the cut spectrum to exactly the same range is incompliant. More evidence for this is seen by the more general evaluation of cut spectra without low frequencies: removing low frequencies can yield changes to KK-compliance in the mid- and high-frequency range as well. Apart from this, from the tables in Appendix B.3 it becomes apparent that removing outlier datapoints and reducing measurement noise has proven to influence the KK-compliance to great extent as well, though not in all cases.

To summarise: the factors that impact the Kramers-Kronig compliance differ per solar cell. KK-compliance consistency between repeated measurements under the same conditions on the same sample is low, indicating KK-compliance is dependent on a variable not listed in the table. From the table, it seems that bias voltage does not play a role in KK-compliance. Though no solid conclusions can be made on what factors impact (in)compliance based on this information, the data found KK-compliant is evaluated in the next section.

4.1.4 Extraction of time-constants using equivalent circuit modeling

KK-compliant data is presented in Table 4.2. This data was modelled with an equivalent circuit to extract time-constants, providing information about the time-scales of transient processes. In the case of MAPI-d103, cutting low-frequency data below 100Hz out resulted in the spectra of Figure 4.5a, containing a high-frequency semi-circle and a shorter low-frequency tail than the full spectra. Below, the results of fitting only the high-frequency semi-circle are presented. In the subsection thereafter, the results of fitting the full KK-compliant spectra including full-length low frequency tail are presented.

MAPI-d103 under illumination condition

- **Modeling of high-frequency semi-circle**

  The high-frequency semi-circles displayed in Figure 4.5a were quantified using Equivalent Circuit Modelling. Multiple equivalent circuits may fit the semi-circle. In this case, the semi-circle is not of perfect shape but somewhat depressed. This means that the semi-circle can be fit by a circuit containing a resistor R1 and a (non-ideal) constant phase element CPE1, or by a circuit containing two parallel RC circuits depicting two overlapping semi-circles with different time constants (double Randles circuit, Figure 4.6). Both results are shown in Table 4.4. The Chi-squared value in the table refers to the quality of fit. It should be smaller than $1E-03$ to ensure minimal quality of fit, and smaller than $1E-5$ to ensure good quality [76]. From the Chi-squared value of both fits, which should be smaller than $1E-03$, it becomes clear that only the double Randles circuit poses a fit of sufficient quality. The calculated time-constants τ (where $\tau = R \cdot C$) are multiplied by 2π to make τ the inverse of the (peak) frequency and to display the correct time-scale in seconds ($\tau \cdot 2\pi = 1/F_{peak}$). The fit parameters are averaged for the different bias voltages, as no voltage-dependence is seen for the real resistance in the Nyquist plot (see Figure 4.5a). To strengthen the argument for averaging the fit parameters, the individual time-constants times 2π per bias voltage are displayed in Figure 4.6, showing no voltage dependence.

TABLE 4.4: Fitting of high-frequency semicircle of MAPId103 Light with two Equivalent Circuit Models. Fit is of sufficient quality if Chi-sqr is smaller than 1E-03.

Model: Rs-R1C1-R2C2	**Chi-Sqr**	**Rs (Ω)**	**R1 (Ω)**	**C1(F)**	**τ1 ·2π (s)**	**R2 (Ω)**	**C2 (F)**	**τ2 ·2π (μs)**
MAPI Light High-Freq (average)	***9,57E-05***	29,6	366	5,50E-09	1,26E-05	253	2,49E-08	39,5
Model: Rs-R1Cpe1	**Chi-Sqr**	**Rs (Ω)**	**R1 (Ω)**	**CPE1-T (F)**	**CPE1-P**	**τ1 ·2π (μs)**		
MAPI Light High-Freq	*2,37E-03*	*20,09*	*630*	*1,2 E-08*	*0,92*	*48*		

A way of checking how robust a circuit model is, is to ensure the fitting model fits a complete dataset (since then it describes the system under various conditions). In this case, the double Randles fitting model fits the high-frequency *LIGHT* semi-circle of $MaPbI_3$-d103 with sufficient quality (Chi-sqr of $1E-04$). The high-frequency *DARK* semi-circle of $MaPbI_3$-d103, which is KK-incompliant data over the full frequency range, can be fit with the double Randles fitting model only partly: the chi-squared values for the bias voltages $0.8V, 0.9V$ and $1.0V$ are $2E-04$, which is sufficient, and the chi-squared values for the other bias voltages is $2E-03$, which is insufficient. This indicates that the double Randles fitting model cannot fit a complete high-frequency dataset of $MaPbI_3$-d103 under various bias voltages and illumination condition. It also indicates that incompliant spectra can be fit with equivalent circuit modeling, resulting in sufficient quality of fit. This stresses the importance of performing the Kramers-Kronig test before extracting parameters using equivalent circuit modelling.

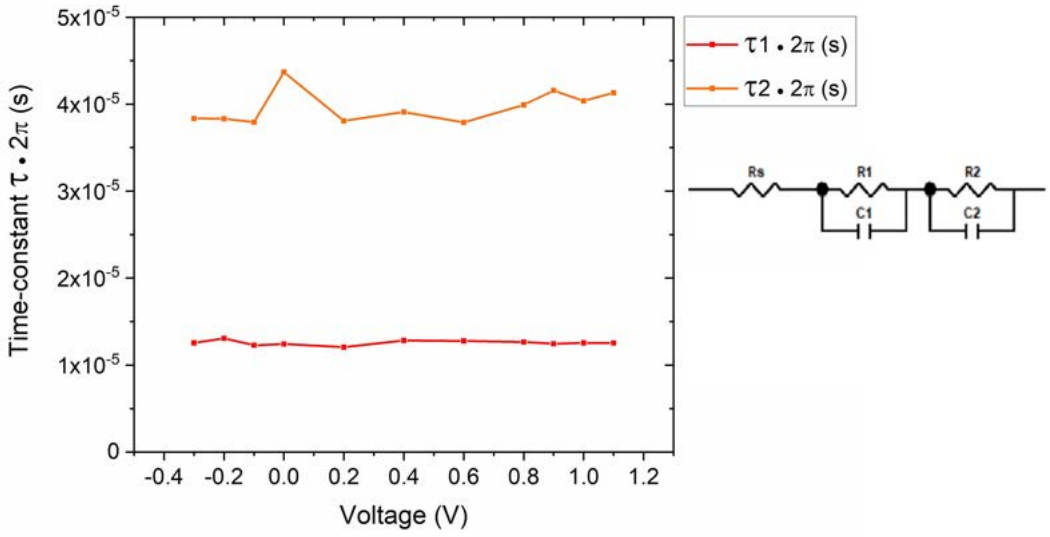

FIGURE 4.6: $MAPbI_3$-d103 LIGHT voltage independence of the processes corresponding to the high-frequency semi-circle. The vertical axis denotes the characteristic frequency the transient processes are active. The parameters are obtained from the time-constants extracted from fitting with double Randles circuit.

- **Modeling of full frequency spectra**

  Four impedance spectra of MAPI-d103 with different bias voltages have been evaluated KK-compliant over the full frequency range. Thus, the full spectra can be modelled. The fitting model used was $Rs - R1CPe1 - W_{open}$, which is KK-compliant over the full measured frequency range (see Figure C.4 in Appendix C). Fitting with the circuit model of 2.16c, used further on in this thesis to model impedance spectra of PSCs under illumination, resulted in bad quality of fits in this case, whereas for the multi-cation devices discussed in section D this fitting model does result in sufficient quality of fit.

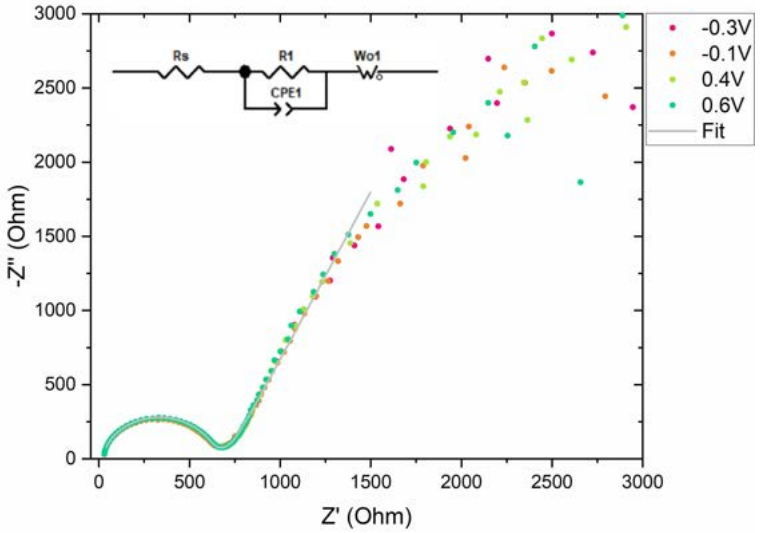

FIGURE 4.7: KK-compliant impedance spectra on the full frequency range of 10^6Hz to 1Hz of MAPI-d103 under illumination condition. The spectra do not show voltage dependence.

TABLE 4.5: Fitting values of MAPI-d103 under illumination with a Randles model and added linear Warburg-open element. The KK-compliant spectra with bias voltages -0.3V, -0.1V, 0.4V and 0.6V are fitted and averaged since no voltage dependence is shown in the Nyquist plot.

	Chi-Sqr	**Rs (Ω)**	**R1 (Ω)**	**CPE1-T** (F)	**CPE1-P**	**Wo1-R**	**Wo1-T**	**Wo1-P**
MAPI-d103 illumination	0,000593	14,87	576,9	1,04E-08	0,9450	393,8	0,0035019	0,37803

It is possible to extract the effective chemical diffusion coefficient from the Wo-T value (see equation 2.10). However, this is only possible if the Wo-P value is fixed to 0.5, indicating a 45 degree slope. From the Nyquist plot in Figure 4.7 it can be deduced that the slope of the impedance data does not amount to 45 degrees, and thus no reliable effective diffusion coefficient can be calculated from the fit. Fitting with a second RCpe element instead of Warburg-open did not result in sufficient quality of fit.

MAPI2

KK-compliant data of MAPI2 under dark and light conditions has been fit with multiple equivalent circuit models. The models are simple and double Randles circuits with and without CPEs. Of the KK-compliant evaluated spectra, see Table 4.2, only the spectra 0V, 0.7V and 0.9V rpt1 taken under illumination could be modelled and result in sufficient quality of fit. For 0V, the time-constants times 2π calculated from the fits are 28μs for process1, and 4.9μs for process2. For 0.7V, the time-constants calculated from the fits are 18μs for process1, and 3.0μs for process2. Surprisingly enough, fitting the full spectrum of 0.8V until 1Hz, evaluated incompliant, with a double randles circuit with CPE's resulted in a sufficient fit (Chi-sqr = 8,0E-04). In this case, both the high and low semi-circle were fit. The Nyquist plot of MAPI2 0.8V Dark is shown in Figure 4.2d. The extracted parameters are not displayed due to incompliance of the spectrum, which invalidates the extracted parameters. The next section deals with repeated measurements under the same conditions on MAPI2 to investigate stability of the measurements.

Summary of KK-compliant data and time-constants

Concluding, it can be said that the high-frequency semi-circle of MAPI-d103 and MAPI2 comprises two processes operating at approximately the same time-scale. Both processes lie in the range of 3-40 microseconds. Additionally, from comparing the Nyquist plots of 4.4, it is observable that the measurements under illumination of MAPI-d103 are not voltage dependent, while the measurements under illumination of MAPI2 are voltage dependent.

4.2 Stability of measurements

Repeated impedance measurements on MAPI2
For MAPI2, the same impedance measurement has been carried out at 0.9V bias voltage in dark condition three times successively on three consecutive days, and for light condition two times shortly after each other. The Maximum Power Point (MPP) of this cell, which marks the standard operating conditions, was determined to be 0.928V. Therefore, repeated measurements under operating conditions (0.9V) are presented. Repeated measurements under illumination at 0V bias are also included. Repeated measurements do not necessarily obtain the same results for perovskite samples, since the state of the samples is dependent on prior conditions the sample was subjected to, and the sample is prone to change due to degradation processes.

Dark condition 0.9V
The measurements were taken from 10^6 to 1Hz, but low frequencies were cut to 100Hz, and KK-analysis has been carried out. All spectra but the first (Day 1 17:24) and last one (Day3 16:18) proved to be compliant. The Nyquist plot of the repeated measurements is seen in Figure 4.8, the KK-residuals plot in Figure 4.9, and fitting results in Table 4.6. The measurement on Day2 18:27 has been subjected to external magnetic fields, as the Faraday cage was removed.

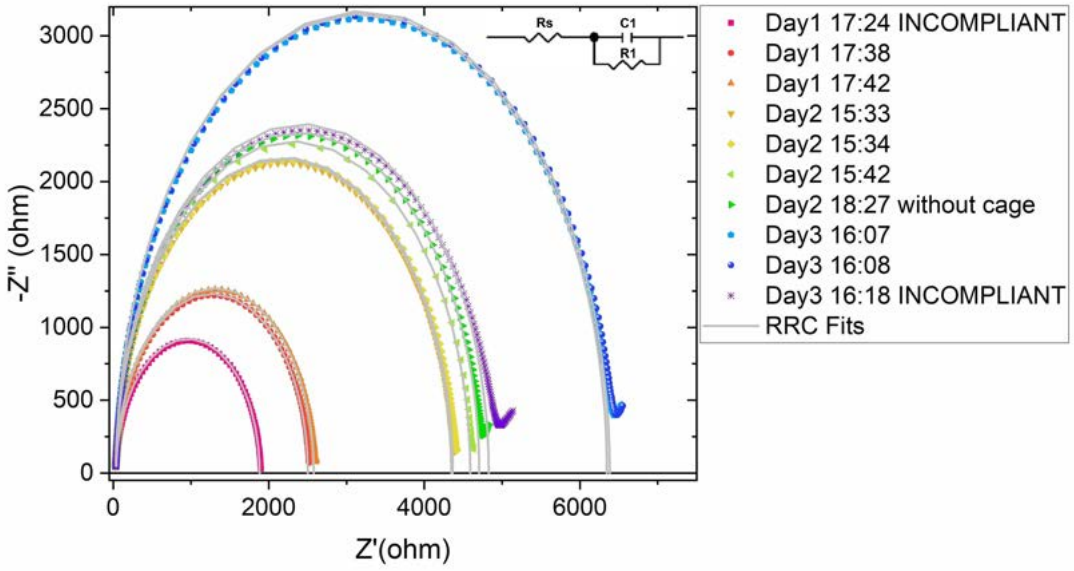

FIGURE 4.8: MAPI2 Dark, 0.9V Repeated measurements at 0.9V under dark conditions. RRC fits are indicated.

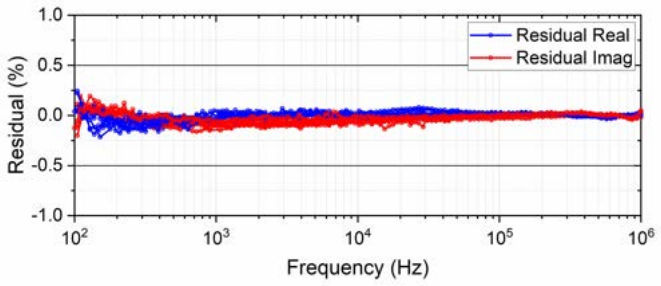

(A) Residuals from the eight KK-compliant spectra shown in the Nyquist plot above.

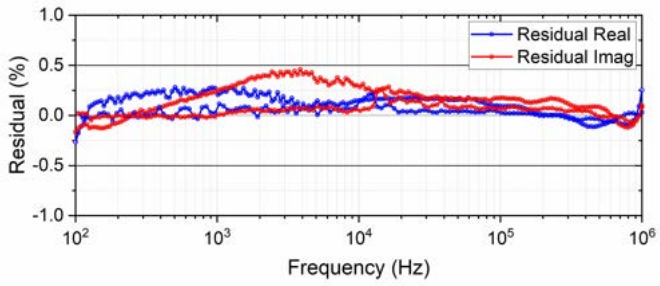

(B) Incompliant spectra. Residuals of Day1 at 17:24 and Day3 at 16:18 are displayed.

FIGURE 4.9: KK-residual plots of repeated measurements on MAPI2 0.9V in the dark.

TABLE 4.6: Fitting of high-frequency semicircle of MAPI2 Red 0.9V with Randles equivalent circuit model (Rs - R1C1). Fit is of sufficient quality if Chi-squared is smaller than 1,00E-03. Please note that the spectra of 17:24 and 16:18 are KK-incompliant, meaning the extracted parameters (in grey) are unreliable. Fit parameters from insufficient quality of fit are displayed in grey as well.

		Chi-Sqr	Rs (Ω)	R1 (Ω)	C1 (F)	$\tau 1 \cdot 2\pi$ (μs)	error $\tau 1$ (%)
Day1	**17:24 INCOMPLIANT**	6,0E-04	*38,01*	*1843*	*3,40E-09*	*39,3*	*0,32*
	17:38	7,0E-04	37,84	2463	3,24E-09	50,1	0,33
	17:42	7,0E-04	37,86	2539	3,22E-09	51,3	0,34
Day2	**15:33**	*1,7E-03*	*30,45*	*4315*	*3,32E-09*	*89,8*	*0,33*
	15:34	*1,1E-03*	*31,44*	*4333*	*3,30E-09*	*89,8*	*0,41*
	15:42	1,0E-03	36,51	4553	3,26E-09	93,0	0,59
	18:27	9,0E-04	30,91	4674	3,03E-09	89,2	0,38
Day3	**16:07**	*1,1E-03*	*39,47*	*6307*	*3,06E-09*	*121*	*0,35*
	16:08	1,0E-03	40,26	6342	3,05E-09	121	0,40
	16:18 INCOMPLIANT	1,0E-03	*36,65*	*4790*	*3,07E-09*	*92,4*	*0,37*

The change in the time-constant τ is mainly due to R1, which moves from 2460Ω to 6300Ω over the successive measurements (a factor 2.6). The Capacitance C1 only changes marginally from 3,2E-09 F to 3,1E-09 F. The resulting changes in $\tau \cdot 2\pi$ go from 50μs to 100μs (a factor 2). The series resistance Rs varies across the successive measurements up and down between 30Ω and 40Ω.

Light condition 0.9V

Measurements in light condition at 0.9V bias voltage were carried out on the same sample and pixel. The spectra were cut to 100Hz and analysed for KK-compliance. The first spectrum taken proved to be KK-incompliant, while the measurement taken about 10 minutes later proved to be KK-compliant without any change in external variables. From KK-incompliant spectra, no reliable parameters can be extracted. Here they are displayed to show that KK-incompliant spectra could in principle, though they should not, be modelled with Equivalent Circuit Modelling, and parameters could be extracted (and falsely processed) if one was not aware of the consequences of KK-incompliance for the reliability of the measurement. The time-constants displayed in Table 4.7 are somewhat lower than for the measurements under dark conditions (6 microseconds as opposed to 40-100 microseconds), and thus depicts a faster process. See Appendix C for another example of KK-incompliant data that can be fit with an ECM and result in a fit of good quality. This spectrum depicts two semi-circles and is taken under dark conditions 0.9V.

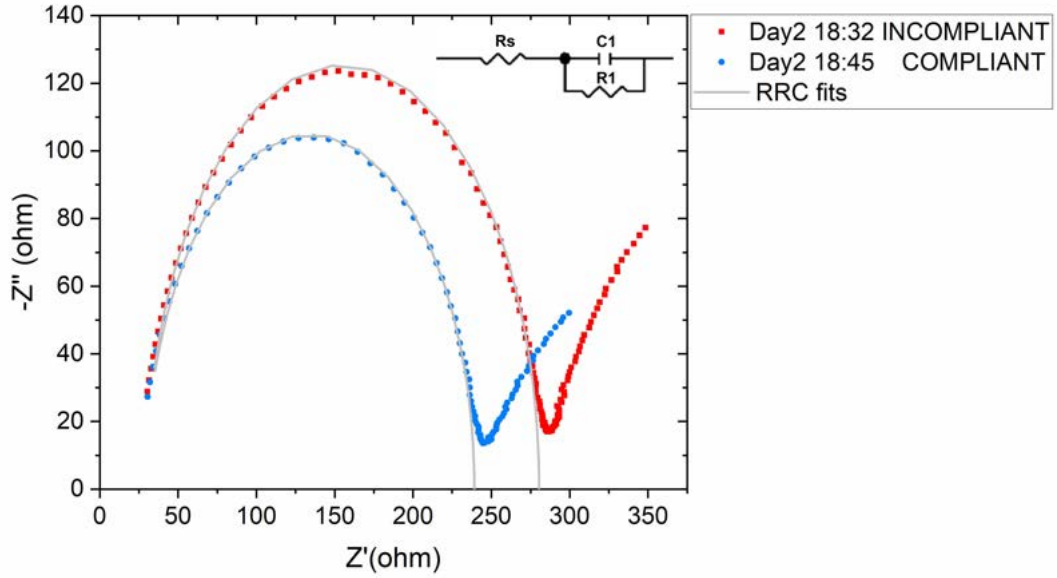

FIGURE 4.10: MAPI2 Light, 0.9V Repeated measurements. RRC fits are indicated.

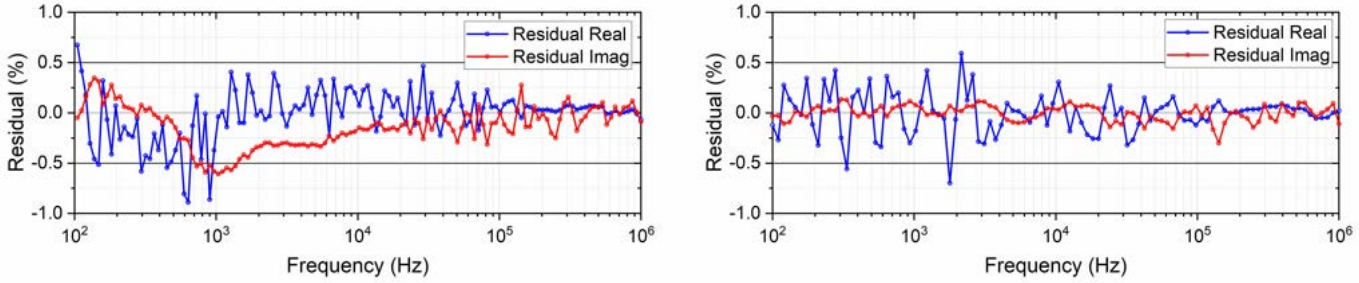

(A) Incompliant spectrum from Day2 18:32.

(B) Compliant spectrum from Day2 18:45

FIGURE 4.11: KK-residual plots of repeated measurements on MAPI2 0.9V in the light.

TABLE 4.7: Fitting of high-frequency semicircle of MAPI2 Red 0.9V in light condition with Randles equivalent circuit model (Rs - R1C1). Fit is of sufficient quality if Chi-squared is smaller than 1,00E-03. Please note that the spectrum of 18:32 is KK-incompliant, meaning the extracted parameters are unreliable.

		Chi-Sqr	**Rs (Ω)**	**R1 (Ω)**	**C1 (F)**	**$\tau 1 \cdot 2\pi$ (μs)**	**error τ (%)**
Day2	**18:32 INCOMPLIANT**	*7,5E-4*	*29,7*	*250,7*	*4,33E-09*	*6,79*	*0,66*
	18:45	3,1E-4	29,34	209,8	4,43E-09	5,84	0,68

Light condition 0.0V

The Nyquist plot of repeated measurements of MAPI2 in light condition at 0V bias voltage is shown in Figure 4.12. This figure is added to complement the repeated measurements of MAPI2 in light condition at 0.9V bias voltage. All spectra are KK-compliant, see Figure 4.13 for the residuals plot.

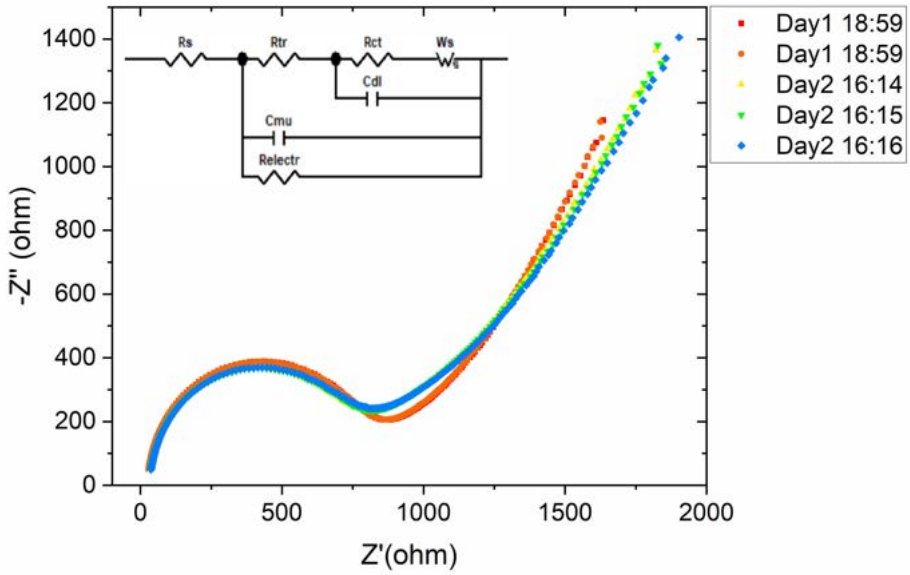

FIGURE 4.12: MAPI2 Light, 0.0V Repeated measurements. Frequency range is from $10^6 Hz$ to $100 Hz$. Minimum of the spectra lies around 10kHz.

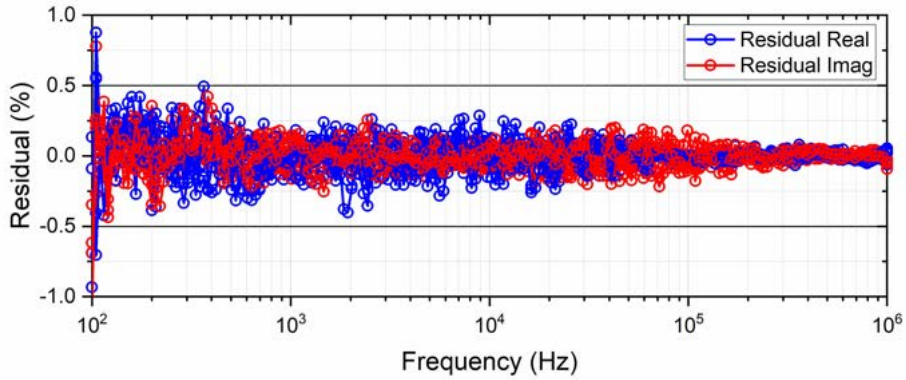

FIGURE 4.13: Kramers-Kronig residual plots of impedance spectra of MAPI2 at 0V bias under illumination condition. The residuals lie within the 0.5% border and show no apparent systematic bias, and the spectra are evaluated KK-compliant.

The high-frequency semi-circle lies in the frequency range of $10^6 Hz$ to $10^4 Hz$. Fitting only this first semi-circle with a Randles circuit containing a constant-phase element CPE does not result in good quality of fit, thus no parameters are extracted. The full spectra can be fit in minimal quality using a double Randles circuit with CPE's and an added linear open Warburg element. Results of this are not included due to the arbitrary choice of the circuit model.

The spectra can also be fit with the model from 2.16c. The parameters extracted are listed in the table below. The difference between the repeated measurements is mostly seen through change of the electrical resistance.

TABLE 4.8: Fitting parameters extracted from fitting with the circuit model of Figure 2.16c.

	Chi-Sqr	Rs (Ω)	Rtr (Ω)	Rct (Ω)	Ws-R	Ws-T	Ws-P	Cdl (F)	Cμ (F)	Relectr (Ω)
Day 1 18:59	6,38E-04	27	785	205	8520	0,031	0,60	1,00E-07	2,66E-09	1,60E+11
Day 2 16:16	6,64E-04	36	744	254	10465	0,034	0,59	7,90E-08	2,73E-09	1,00E+20

Solar cell performance before and after impedance measurements

In figure 4.14 current voltage characteristics are shown which are made in between the impedance sessions. This is done to evaluate the impact of the impedance measurements on the device performance. The plot is shown in logarithmic scale which makes small changes in performance apparent. From the JV curves under illumination condition (Light), it can be deduced that no apparent change is occuring. From the JV curves made in the dark, it can be deduced that the impedance measurements have only a minimal impact on the conductivity. The effect is reversible over time, as the last measurement on day 3 shows (small dots). Concluding it can be said that the impedance measurements itself cause no irreversible changes to de perovskite solar cell device performance.

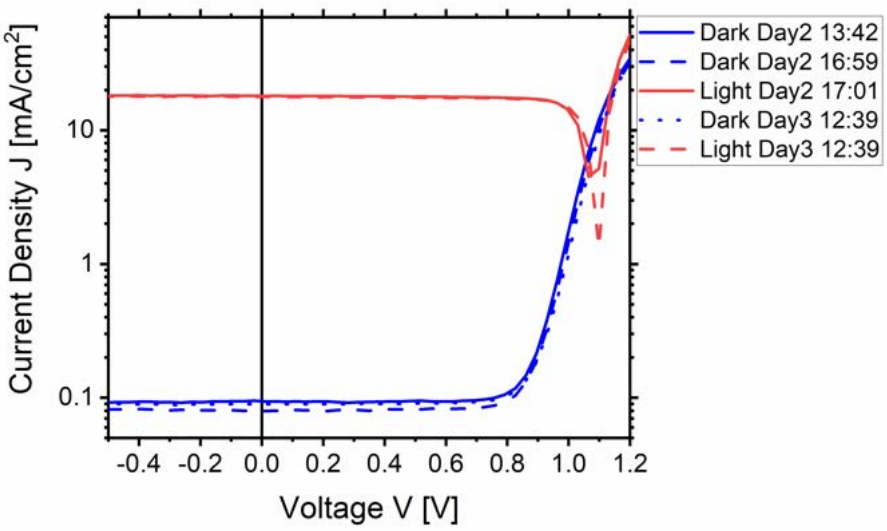

FIGURE 4.14: MAPI2 current-voltage characteristics taken in between impedance measurements, on a logarithmic scale. Minimal change in performance indicates the impedance measurement does not degrade the device.

Chapter 5

Discussion

5.1 Violation of KK-requirements in incompliant spectra

In this thesis, the factors that make an impact on KK-(in)compliance of perovskite solar cells were investigated by varying the DC bias voltage, illumination conditions and frequency range looked at. The results indicate that sample stability is the largest factor determining the (in) compliance. Illumination seems to make an impact on the (in)compliance, whereas DC bias voltage seems not to make an impact on the (in)compliance. Additionally, by assessing different parts of the impedance spectra, it was found that (in)compliance seems to be frequency range dependent (Table 4.3).

The four requirements underpinning Kramers-Kronig compliance are *linearity, stability, causality* and *finiteness* (see section 2.3). From these factors, stability seems to be the problematic factor. Results show that impedance spectra from repeated measurements are in some cases evaluated as compliant and in some cases as incompliant- without a change in measurement conditions. It is therefore likely that the change between compliance and incompliance stems from an unstable sample during the measurement. Repeat measurements switch not only between compliance and incompliance, they also differed quantitatively (section 4.2). Thus, the sample seems to change both during the measurement (leading to incompliance) and between measurements (leading to different quantities).

Changes in quantity and changes in KK-compliance for repeated measurements on MAPI2 can be seen from the results in Figures 4.9 and 4.11 and the corresponding fitting tables. The Nyquist plots of repeated measurements do not overlap and the fitting tables show increases in mainly the value of real resistance. The associated residual plots change as well, showing biased residuals at different frequencies for KK-incompliant evaluated spectra.

Poor sample stability is expected to express itself by biased residuals towards lower frequencies, as at lower frequencies the measurement time increases (and the sample changes over time). However, the spectra discussed above show bias in the residuals at *high frequencies*: from 10^6 to 100Hz. The measurement there is much shorter (several seconds) compared to measurements down to 1Hz (which take more than 2 minutes). The change in the residual spectra is not one directional (as in the example in Figure 2.14): bias in the residual spectra increases and decreases at different places in the frequency spectrum for the same measurements under the same conditions. Thus, if the sample is indeed unstable, it seems to be expressed at higher frequencies, in a non-trivial way.

Another cause for biased residuals at higher frequencies could be violation of the *linearity* requirement. Then, the amplitude of the AC perturbation voltage was set too high. This would lead to higher harmonics in the output signal, irrespective of the frequency at which was measured. Therefore, if the residuals show bias irrespective of frequency (across the whole spectrum), consistently for repeated measurements under the same conditions, the linearity constraint may have been violated. Residual plots of repeated measurements on MAPI2 show compliance and incompliance inconsistently, and therefore the linearity requirement is most likely not violated. Experimentally, by zooming into the JV-curve and making a linear regression it can

be checked if the data is taken in the linear (Ohmic) regime. Resolution of the JV-curves was not high enough to check this for this dataset.

If there is an unknown variable influencing the measurement, this could explain the incompliant measurements as the *causality* requirement would have been violated. An example of how purposely changing the temperature leads to bias in the residuals at low frequencies can be found in Appendix B.1 (example 5). However, the unknown variable has to be an occasional and fast fluctuation of a parameter since most measurements are KK-compliant, and the bias is seen non-trivially at different places along the frequency spectrum irrespective of a change in measurement parameters (DC bias or illumination). A flickering of stray light could possibly lead to the incompliant measurements at higher frequencies, though care was spend to prevent this from occurring: in the dark the Faraday cage blocks stray light. Additionally, the Faraday cage blocks influences from external electric sources and prevents noise from occurring in the low frequency range. Another possibility for KK-incompliance in different frequency decades can be artifacts due to the measurement setup.

It can be concluded that KK-requirement violated is *stability*, if sample instability is expressed at higher frequencies, or possibly *causality* if the measurement was disturbed by an occasional and fast changing variable like a flickering of light. Based on the data, it seems that the measurement results are not reproducible both in terms of quantity and in terms of residual spectra (KK-compliance). For KK-incompliant measurements, the bias in the residuals is not reproducible because the frequency at which maximum bias occurs varies for every measurement. Since the sample already changes when no variable is introduced, no conclusions should be attributed to the measurements in which a variable *was* changed, such as perovskite composition, DC bias voltage, illumination condition, or KK-compliance assessment of different parts of the impedance spectra.

Not only sample stability hinders a conclusion attributed to the data. Additionally, large sample to sample variation impedes making conclusions. For example: under illumination MAPI-d103 does not show voltage dependence, but MAPI2 does (Figure 4.4). This indicates that for the same type of sample under the same conditions the processes occurring within the solar cell are fundamentally different. This argument is strengthened by the different results for MAPI-d103 and MAPI2 at which factors make an impact on the KK-compliance (Table 4.3). Therefore, both sample stability and sample reproducibility impede arriving at reliable conclusions.

Based on analysis of this data and summary in the before mentioned table, it can therefore only be suggested that illumination may and DC bias voltage may not make an impact on KK-compliance, and the KK-compliance may be dependent on the specific frequency range looked at. If measurement statistics and number of samples are increased these results can gain reliability.

Additionally, it has been found that deleting lower frequency data (<10Hz) also has a diminishing influence on the residuals at higher frequency data (>500Hz) (appendix B.3.1 illumination condition). This may be due to the associated fitting problem of incompliant data imported in the Lin-KK tool, which can influence the residuals over a broad range (Figure B.1). Special care should be taken on analysing the right cut-off point for compliant/incompliant data.

5.2 Factors causing KK-incompliance

Apart from connecting the KK-incompliant data to the specific KK-requirement violated, below the link between (in)compliance and dependence on illumination, DC bias voltage and frequency range is discussed based on observations in the data and theory. The consequences of noise for KK-compliance testing and methods to increase signal-to-noise ratio are discussed at last.

Firstly, for MAPI-d103 we see that spectra taken under dark conditions are incompliant, whereas spectra taken under *light* conditions are *compliant*. This is not expected, as illumination stresses the device, which may lead to chemical reactions during the measurement leading to KK-incompliance. For example, a light-induced chemical reaction can lead to a change in the electrical properties (i.e. conductivity) of the sample during the measurement. Another explanation for the dark incompliance could be the existence of a link between the hysteresis of the solar cell, which is most pronounced in the dark (see the JV-curves in Figure 4.1c), and the KK-incompliance which is only present in the dark. Lee et al. found that for MAPI dark hysteresis can be partly explained due to ion migration (based on temperature dependent JV-characteristics that begin to show hysteresis around the frozen time for iodide ion migration [80]). However, the frequency region that shows incompliance in the dark spectra is $10^4 - 10^5$Hz, which is just too fast for Iodide ion migration. Additionally, it was found that the data under illumination could not be modelled with a Warburg element (the slope in the Nyquist plot is not 45°). Besides, the link between ion migration and KK-incompliance is not well defined as well, since ion migration itself is a KK-compliant process (but its consequences are not if ion migration leads to degradation). In considering the origin of dark incompliance and light compliance it is important to note that the JV-curve under illumination might not be the superposition of the JV-curve taken in the dark, since we are working with non-ideal solar cells [81]. Thus, dark and light (in)compliance may not necessarily be correlated.

Secondly, here the link between DC bias voltage and (in)compliance is discussed. The results (Table 4.3) show that DC bias voltage seems disconnected from KK-(in)compliance. In the case of the linearity requirement this can be explained: if the V_{AC} is chosen appropriately small for each bias voltage, the measurement is taken in the linear regime and KK-compliance is independent of bias voltage. If the amplitude of the signal is chosen constant, however, the V_{ac} perturbation signal which is appropriate at smaller bias voltages could enter a non-linear region of the JV-curve around the maximum power point, where the curvature is biggest. Then, KK-compliance would be bias voltage dependent. The absence of a link between DC bias voltage and KK-compliance in the data seems to suggest that DC bias voltage does not affect the stability (and consequent degradation) of the solar cell.

Thirdly, KK-compliance may be dependent on a specific frequency range, for example in the case of a blocking contact which leads to impedance values going to infinity at low frequencies. This is not shown in the data, though biased residuals are present for MAPI2 at *low* frequencies, and for MAPI-d103 at *high* frequencies (under dark conditions). Bias in the residuals happens thus at different frequency regions for the same type of sample. Fast or slow processes might thus limit KK-compliance dependent on the sample. Theoretical explanations for biased residuals at low frequencies may be sample instability, low measurement accuracy due to equipment limits (though this seems not to be the case, Figure E.1), or influences from external electric fields produced by power supply of equipment (the sample was shielded by the Faraday cage, but the connection cables were not electrically shielded). Bias at high frequency can be induced by cable inductance. There is debate whether cable inductance would show up consistently for each sample, or that the influence of cable inductance would also be sample dependent.

Lastly, noisy data is difficult to evaluate for KK-compliance because the noise gets propagated to the residual spectrum. Measurement noise is present when there is low sample conductivity (generally under low bias voltages when the perovskite is insulating), and in the dark when there are no photo-generated charges. To increase the signal to noise ratio, V_{ac} can be increased, paying close attention the linearity requirement does not get violated. Noise is also more prevalent for low-frequency measurements. External sources operating at these frequencies may produce electric fields which disturb the measurement. Therefore shielding using a Faraday cage is important. Additionally the connection wires should be shielded [40], which was not the case in our experimental setup. Other measures to reduce noise can be to increase the integration time or to increase the number of integrations during the measurement. This,

however, leads to an increase of measurement time which is ill-advised for samples dealing with stability issues. Reducing the number of frequency points is recommended when applying this measure [40]. Smoothing impedance spectra before KK-analysis with the Lin-KK tool could in principle reduce noise in the residuals, without altering test expression of biased residuals. However, it is debatable if it can be quantified which data is noise and which data is real data.

5.3 KK-compliance and Equivalent Circuit Modelling

The fitting results from equivalent circuit modelling on MAPI-d103 and MAPI2 (section 4.1.4) indicated that KK-incompliant data can be fit with low error in equivelent circuit modelling. This is additionally demonstrated in Appendix C, where an incompliant spectrum with a loop in the Nyquist plot is modelled with a by-definition KK-compliant circuit model in low error. The results from modelling the spectra of the multi-cation PSCs can be found in Appendix D, since they behaved similar as the $MaPbI_3$ cells and no further reliable insights were derived from this data.

Only a very small number of impedance spectra of PSCs in this thesis was rated KK-compliant. The consequence of the small number of compliant spectra is that it was impossible to find a robust equivalent circuit model for the data: the models used could not describe a similar sample due to large sample-to-sample variation. Therefore the time-constants extracted using equivalent circuit modelling are not attributed to physical processes. Since additionally a measurement on a sample may be KK compliant/incompliant under both the same and different conditions, this makes it difficult to develop a robust, universal model based on this data.

Many equivalent circuit models for IS on PSCs exist in literature. Reasons why many models are proposed are firstly that the architecture of cells (composition of the perovskite and contact layers) is often different. Secondly, the solar cells are often not stable enough. This means that the sample changes during long impedance measurements. Plus, the sample cannot be expected to give the same response under the same conditions again, as a result of external stress imposed by the measurement or measurement conditions. Additionally, both temporary and permanent changes in device performance are present. Thirdly, due to hysteresis it is not clear under which conditions the impedance measurement should be carried out (pre-biasing or light soaking). Fourthly, due to lack of understanding of the physical origin of transient processes in PSCs (both electronic and ionic) the designed models are often not robust enough to describe the sample for variation in illumination or DC bias voltage. Fifthly, the transient processes in perovskites happen on a range of timescales that is impractical or outside equipment limits. Sixthly, because samples cannot be reproduced well enough to ensure the same impedance response for the same type of samples. Lastly, conclusions in literature may be based on unreliable data since the Kramers-Kronig compliance test is rarely performed [44], and measurement protocols are not sufficiently documented or standardised. Since currently there is no unique circuit model for a frequency spectrum, attributing the features in the spectrum to a specific physical mechanism is not trivial.

In this thesis it has been has been demonstrated that KK-incompliant data can be fit in low error to a circuit model as well. That this is possible may contribute to the difficulties of developing a robust, universal model. This leads to the open question: where is the threshold for KK-compliance/incompliance that results in errors in the ECM analysis?

5.4 Measurement protocol and analysis methods

Elaborate guidelines are available for measuring perovskite solar cells and documenting the results [82, 83, 84]. During the International Summit on Organic Photovoltaic Stability (ISOS), a consensus was reached between researchers in the field for protocols to test perovskite solar cell stability [85]. This includes JV-scans, EQE, storage, stress conditions, encapsulation and more. Additionally, in the supplementary information of the before-mentioned article a template is provided for data reporting.

However, detailed protocols on performing impedance spectroscopy measurements on PSCs to ensure stability and reliability are missing from these documents and are generally not discussed in literature in the field. The results in this thesis indicate that sample stability and variation impede making reliable conclusions. It is therefore recommended the measurements are performed in such a way that the sample is disturbed as little as possible (by voltage, illumination and oxygen/water exposure) and the number of Kramers-Kronig compliant spectra is increased. Below, suggestions are made to ensure and check stability of PSCs during impedance spectroscopy sessions.

Suggestions to develop a measurement protocol based on this research include:

1. Perform a test measurement at 3 different sizes of the V_{AC} perturbation signal in the dark at 0.2V bias (In the dark at 0V a noisy and only capacitive response is obtained, providing no information). If the measurement results are the same, the test-signal is chosen correctly. Perform the same test under applied bias near MPP and V_{OC} on a reference device to make sure also a quasi-linear regime is reached where the curvature of the JV-curve is larger. Confirm with a linear regression around the voltage measurement point in the JV-curve with the amplitude of V_{AC} as range. The Kramers-Kronig compliance of a measurement can be assessed directly after taking the measurement since the Lin-KK allows for rapid analysis. If measurements are KK-incompliant, the measurement parameters and external influences should be evaluated. Lastly, the KK-incompliant measurement should be repeated every few minutes and checked for any changes in the residuals [86] to see the impact of wait (relaxation) time. Repeat the test measurements on the reference device under light conditions.

2. In determining the measurement protocol, take relaxation times for exposure to light and voltage into account before a later measurement is performed (introduce a wait-time until the device is stable).

3. Perform IS measurements on 1 of the 6 pixels of a sample only, to make sure exposure to illumination during IS measurement of several pixels do not influence each other.

4. Perform JV-measurements as cross-checks to make sure the sample performance has not decreased due to the IS measurement (only dark JV-characterisation for only dark IS measurements, dark and light JV-characterisation for light IS measurements). Keep track of changes in the maximum power point and V_{OC}.

5. Repeat the same set of measurements 24h later to make sure the device behaviour is representable, since perovskite solar cells are known to recover from stress after storage in the dark in a nitrogen-filled glovebox for several hours [44].

6. Repeat the same set of measurements for an identical architecture device in the same batch and as well repeated batches to increase statistics of device behaviour. This is necessary as sample reproducibility is low.

7. Perform IS measurements on a fixed frequency range, to keep exposure to external stress conditions as bias voltage and illumination constant.

8. Perform the same set of measurements on each device consistently following the same measurement protocol.
9. Measure in dry/inert atmosphere with temperature control and store in a nitrogen glovebox in the dark.
10. Use electrical shielding for the sample (using a Faraday cage) and the connection wires [40].

Additionally, the guidelines presented in the two papers that *do* discuss reliability of impedance spectra of perovskite solar cells [33, 40] should be applied and taken into account when designing a measurement protocol. Lastly, standardisation of measurement protocol and incorporation of the Kramers-Kronig compliance test is necessary to allow for inter-study comparability.

5.5 Future outlook

Based on this research, three recommendations for future work on KK-compliance of impedance spectroscopy data of PSCs are formulated. First, there is a need to quantify and reevaluate KK-compliance thresholds for the spectra in comparison to the errors in equivalent circuit modelling. In principle, KK-incompliant spectra cannot be modelled by a by definition KK-compliant circuit model, though in this thesis it was demonstrated that this was possible with low error. Either the threshold for KK-incompliance was set too strict, or the allowed error on equivalent circuit modelling was set too loose. The evaluation of KK-(in)compliance was now based on six example evaluations of residual spectra included with the Lin-KK tool (see 2.3.2 and B). Other tools may provide more quantitative measures for KK-(in)compliance. For example, the software RelaxIS by Nova has the same functionality as the Lin-KK tool, plus provides additional statistical Chi-sqr, p-values and Shapiro-Wilk-Normality parameters for the goodness of fit and residuals [76]. Another tool of interest has been published recently, where several scores that provide quick metrics for the evaluation of the EIS data quality have been proposed. Here, the Kramers-Kronig relations have been reformulated under a Bayesian framework [87].

Second, IS data on PSCs can be corroborated with other measurement techniques to add strength to the conclusions based on IS. Stability needs to be ensured with JV-checks, or any changes to the perovskite or interfaces can be observed with structural studies such as XRD or (cross-sectional) SEM. Other methods to extract timescales of carrier dynamics (electrical, optical) and compare these to results from impedance analysis are transient photovoltage (TPV), transient/intensity-modulated photocurrent spectroscopy (TPC or IMPS) measurements [88, 89, 90, 91]. These techniques can be split into small and large modulation methods, where either a small perturbation is applied on top of a base light intensity, or the light is switched on or off. In both cases, the device voltage or current response is measured during and after the excitation. Using these techniques, the transient device response in carrier transport, accumulation and recombination kinetics can be investigated [88]. An overview of characterisation techniques for PSCs is presented by Kim et al., including an overview of more techniques to investigate carrier dynamics and measure device performance of PSCs [92]. These methods can contribute to the design of a universal and robust circuit model for PSCs.

Third, analysis of impedance spectra and subsequently equivalent circuit modelling is not trivial due to anomalous device behaviour and responses. This leads to varying attributes in the impedance spectra. After analysis of the spectra in this thesis, a paper was found in which guidelines are presented to do ECM and empirical analysis on impedance spectra [93]. These guidelines can be followed or further developed to work towards a universal approach for the analysis of impedance spectra of perovskite solar cells.

Chapter 6

Conclusion

In this research, four pure $MaPbI_3$ perovskite solar cells and two multi-cation perovskite solar cells $Ma_{0.95}Ga_{0.05}PbI_3$ and $Ma_{0.95}Fa_{0.05}PbI_3$ have been measured using impedance spectroscopy. The research was centered around the question: *Which factors impact the KK-compliance of impedance spectra from perovskite solar cells and what is the influence on equivalent circuit modelling*

The factors investigated to make an impact on KK-(in)compliance were illumination, DC bias voltage and the frequency range looked at. It was found that it is sample dependent which factors influence KK-compliance. Additionally, the analysis showed low consistency of KK-compliance between repeated measurements under the same measurement conditions on the same sample. Therefore, KK-compliance is dependent on a variable not checked, and any conclusions connected to the impact of the assessed factors are as well dependent on this underlying variable. The KK-requirement violated is likely to be *stability*, since both the impedance spectra and KK-residual plots can not be systematically reproduced. It was found that bias voltage does not make an impact on KK-compliance, whereas the illumination and frequency range looked at may have an impact. Physical causes for incompliance might be changes in contact conductivity due to degradation processes enabled by ion migration or external electric influences.

Further it was found that a large portion of the data was KK-incompliant, leaving limited possibilities to analyse the data using equivalent circuit modelling. Here it was found that due to large sample-to-sample variation the compliant spectra could not be fit to one model consistently, hence no physical parameters could reliably be attributed to the spectra. Additionally, it was demonstrated that KK-incompliant data can be fit to a KK-compliant ECM and result in sufficient quality of fit (see Appendix C). Therefore further research needs to be done on thresholds for KK-incompliance leading to errors in equivalent circuit modelling.

Based on this research, guidelines were composed to promote KK-compliance in the data and perform checks for stability to increase reliability of IS measurements on PSCs. Additionally, future research using KK-compliant spectra could corroborate time-constants obtained using impedance spectroscopy with timescales for carrier dynamics obtained with transient photovoltage (TPV) or transient photocurrent spectroscopy (TPC). Both in measuring and in analysing IS data guidelines should be followed [40, 93]. Finally, understanding (semi-)reversible processes which induce changes in device performance, and subsequently lead to degradation, can lead to stable perovskite solar cells in the future.

Bibliography

[1] Susanne Koch. *Correlation between Trap State Properties and Ion Migration in Metal Halide Perovskites*. PhD thesis, Universitat Konstanz, Konstanz, 2018.

[2] Dieter Lüthi, Martine Le Floch, Bernhard Bereiter, Thomas Blunier, Jean Marc Barnola, Urs Siegenthaler, Dominique Raynaud, Jean Jouzel, Hubertus Fischer, Kenji Kawamura, and Thomas F. Stocker. High-resolution carbon dioxide concentration record 650,000-800,000 years before present. *Nature*, 453(7193):379–382, 5 2008. ISSN 14764687. doi: 10.1038/nature06949.

[3] NOAA US Department of Commerce. Global monitoring laboratory - carbon cycle greenhouse gases, Oct 2005. URL https://esrl.noaa.gov/gmd/ccgg/trends_ch4/.

[4] Rebecca Lindsey. Climate change: Atmospheric carbon dioxide: Noaa climate.gov, Aug 2020. URL https://www.climate.gov/news-features/understanding-climate/climate-change-atmospheric-carbon-dioxide. Date accessed 29 September 2020.

[5] Kate Marvel, Benjamin I. Cook, Céline J.W. Bonfils, Paul J. Durack, Jason E. Smerdon, and A. Park Williams. Twentieth-century hydroclimate changes consistent with human influence. *Nature*, 569(7754):59–65, 5 2019. ISSN 14764687. doi: 10.1038/s41586-019-1149-8. URL https://www.nature.com/articles/s41586-019-1149-8.

[6] Union of Concerned Scientists. The connection between climate change and wildfires, 2020. URL https://www.ucsusa.org/resources/climate-change-and-wildfires. Date accessed 29 September 2020.

[7] FAO. *Climate Change and Food Security: A Framework Document*. 2008. URL http://www.fao.org/3/k2595e/k2595e00.htm.

[8] Carolyn Gramling. Australia's wildfires have now been linked to climate change, Mar 2020. URL https://www.sciencenews.org/article/australia-wildfires-climate-change. Date accessed 29 September 2020.

[9] BP. Full report – BP Statistical Review of World Energy 2019. Technical report, 2019.

[10] Jeff Tsao, Nate Lewis, and George Crabtree. Solar faqs, 2006. URL https://www.sandia.gov/~jytsao/Solar%20FAQs.pdf. Date accessed 29 September 2020.

[11] Josh Floyd. What is the potential for renewable energy, May 2016. URL https://beyondthisbriefanomaly.org/2016/04/07/what-is-the-potential-for-renewable-energy/. Date accessed 29 September 2020.

[12] Patrick Moriarty and Damon Honnery. What is the global potential for renewable energy? *Renewable and Sustainable Energy Reviews*, 16:244–252, 2011. doi: 10.1016/j.rser.2011.07.151.

[13] Akihiro Kojima, Kenjiro Teshima, Yasuo Shirai, and Tsutomu Miyasaka. Organometal halide perovskites as visible-light sensitizers for photovoltaic cells. *Journal of the American Chemical Society*, 131(17):6050–6051, 5 2009. ISSN 00027863. doi: 10.1021/ja809598r.

[14] NREL. Best research-cell efficiency chart, 2020. URL https://www.nrel.gov/pv/cell-efficiency.html. Date accessed 29 September 2020.

[15] European Perovskite Initiative. Perovskite-based photovoltaics: A unique chance for European PV-industry. Technical report, EPKI – Perovskite-PV European White Paper, 2019.

[16] Dianxing Ju, Yangyang Dang, Zonglong Zhu, Hongbin Liu, Chu Chen Chueh, Xiaosong Li, Lei Wang, Xiaobo Hu, Alex K.Y. Jen, and Xutang Tao. Tunable Band Gap and Long Carrier Recombination Lifetime of Stable Mixed CH3NH3PbxSn1- xBr3 Single Crystals. *Chemistry of Materials*, 30(5):1556–1565, 3 2018. ISSN 15205002. doi: 10.1021/acs.chemmater.7b04565. URL https://pubs.acs.org/sharingguidelines.

[17] Qifan Xue, Ruoxi Xia, Christoph J. Brabec, and Hin Lap Yip. Recent advances in semi-transparent polymer and perovskite solar cells for power generating window applications, 7 2018. ISSN 17545706. URL https://pubs.rsc.org/en/content/articlehtml/2018/ee/c8ee00154ehttps://pubs.rsc.org/en/content/articlelanding/2018/ee/c8ee00154e.

[18] Yaoguang Rong, Yue Hu, Anyi Mei, Hairen Tan, Makhsud I. Saidaminov, Sang Il Seok, Michael D. McGehee, Edward H. Sargent, and Hongwei Han. Challenges for commercializing perovskite solar cells, 9 2018. ISSN 10959203. URL http://science.sciencemag.org/.

[19] Moritz H. Futscher, Ju Min Lee, Lucie McGovern, Loreta A. Muscarella, Tianyi Wang, Muhammad Irfan Haider, Azhar Fakharuddin, Lukas Schmidt-Mende, and Bruno Ehrler. Quantification of ion migration in CH3NH3PbI3 perovskite solar cells by transient capacitance measurements. *Materials Horizons*, 6(7):1497–1503, 8 2019. ISSN 20516355. doi: 10.1039/c9mh00445a. URL https://pubs.rsc.org/en/content/articlehtml/2019/mh/c9mh00445ahttps://pubs.rsc.org/en/content/articlelanding/2019/mh/c9mh00445a.

[20] Sang Won Lee, Seongtak Kim, Soohyun Bae, Kyungjin Cho, Taewon Chung, Laura E. Mundt, Seunghun Lee, Sungeun Park, Hyomin Park, Martin C. Schubert, Stefan W. Glunz, Yohan Ko, Yongseok Jun, Yoonmook Kang, Hae Seok Lee, and Donghwan Kim. UV Degradation and Recovery of Perovskite Solar Cells. *Scientific Reports*, 6(1):1–10, 12 2016. ISSN 20452322. doi: 10.1038/srep38150. URL www.nature.com/scientificreports.

[21] Jae Sung Yun, Jincheol Kim, Trevor Young, Robert J. Patterson, Dohyung Kim, Jan Seidel, Sean Lim, Martin A. Green, Shujuan Huang, and Anita Ho-Baillie. Humidity-Induced Degradation via Grain Boundaries of HC(NH ₂) ₂ PbI ₃ Planar Perovskite Solar Cells. *Advanced Functional Materials*, 28(11):1705363, 3 2018. ISSN 1616301X. doi: 10.1002/adfm.201705363. URL http://doi.wiley.com/10.1002/adfm.201705363.

[22] Sisi He, Longbin Qiu, Luis K. Ono, and Yabing Qi. How far are we from attaining 10-year lifetime for metal halide perovskite solar cells?, 4 2020. ISSN 0927796X.

[23] Zongqi Li, Yingzhi Zhao, Xi Wang, Yuchao Sun, Zhiguo Zhao, Yujing Li, Huanping Zhou, and Qi Chen. Cost analysis of perovskite tandem photovoltaics. *Joule*, 2(8):1559–1572, 2018. doi: 10.1016/j.joule.2018.05.001. URL https://doi.org/10.1016/j.joule.2018.05.001.

[24] Weijun Ke and Mercouri G Kanatzidis. Prospects for low-toxicity lead-free perovskite solar cells. *Nature communications*, 10(1):965, 2019. doi: 10.1038/s41467-019-08918-3. URL https://doi.org/10.1038/s41467-019-08918-3.

[25] Riski Titian Ginting, Mi Kyoung Jeon, Kwang Jae Lee, Won Yong Jin, Tae Wook Kim, and Jae Wook Kang. Degradation mechanism of planar-perovskite solar cells: correlating evolution of iodine distribution and photocurrent hysteresis. *Journal of Materials Chemistry A*, 5(9):4527–4534, 2017. ISSN 20507496. doi: 10.1039/c6ta09202k.

[26] Diego Di Girolamo, Fabio Matteocci, Felix Utama Kosasih, Ganna Chistiakova, Weiwei Zuo, Giorgio Divitini, Lars Korte, Caterina Ducati, Aldo Di Carlo, Danilo Dini, and Antonio Abate. Stability and Dark Hysteresis Correlate in NiO-Based Perovskite Solar Cells. *Advanced Energy Materials*, 9(31):1901642, 8 2019. ISSN 1614-6832. doi: 10.1002/aenm.201901642. URL https://onlinelibrary.wiley.com/doi/abs/10.1002/aenm.201901642.

[27] Seckin Akin. Hysteresis-Free Planar Perovskite Solar Cells with a Breakthrough Efficiency of 22% and Superior Operational Stability over 2000 h. *ACS Applied Materials and Interfaces*, 11(43):39998–40005, 2019. ISSN 19448252. doi: 10.1021/acsami.9b13876. URL https://pubs.acs.org/doi/abs/10.1021/acsami.9b13876.

[28] Severin N Habisreutinger, Nakita K Noel, and Henry J Snaith. Hysteresis index: A figure without merit for quantifying hysteresis in perovskite solar cells. *ACS Energy Letters*, 3(10): 2472–2476, 2018.

[29] Wolfgang Tress, Mozhgan Yavari, Konrad Domanski, Pankaj Yadav, Bjoern Niesen, Juan Pablo Correa Baena, Anders Hagfeldt, and Michael Graetzel. Interpretation and evolution of open-circuit voltage, recombination, ideality factor and subgap defect states during reversible light-soaking and irreversible degradation of perovskite solar cells. *Energy and Environmental Science*, 11(1):151–165, 1 2018. ISSN 17545706. doi: 10.1039/c7ee02415k. URL https://pubs.rsc.org/en/content/articlehtml/2018/ee/c7ee02415khttps://pubs.rsc.org/en/content/articlelanding/2018/ee/c7ee02415k.

[30] Beatriz Romero, Gonzalo del Pozo, Belén Arredondo, Diego Martín-Martín, Enrique Hernández-Balaguera, and María del Carmen López González. Characterization of organic and perovskite solar cells by impedance spectroscopy. In Monica Lira-Cantu and Zakya H. Kafafi, editors, *Women in Renewable Energy (WiRE)*, volume 11095, pages 1 – 10. International Society for Optics and Photonics, SPIE, 2019. doi: 10.1117/12.2530568. URL https://doi.org/10.1117/12.2530568.

[31] Pilar Lopez-Varo, Juan A Jiménez-Tejada, Manuel García-Rosell, Sandheep Ravishankar, Germà Garcia-Belmonte, Juan Bisquert, and Osbel Almora. Device Physics of Hybrid Perovskite Solar cells: Theory and Experiment. *Advanced Energy Materials*, 8(14):1702772, 2018. doi: 10.1002/aenm.201702772. URL https://onlinelibrary.wiley.com/doi/abs/10.1002/aenm.201702772.

[32] Pankaj Yadav, Silver Hamill Turren-Cruz, Daniel Prochowicz, Mohammad Mahdi Tavakoli, Kavita Pandey, Shaik M. Zakeeruddin, Michael Grätzel, Anders Hagfeldt, and Michael Saliba. Elucidation of Charge Recombination and Accumulation Mechanism in Mixed Perovskite Solar Cells. *Journal of Physical Chemistry C*, 122(27):15149–15154, 7 2018. ISSN 19327455. doi: 10.1021/acs.jpcc.8b03948. URL https://pubs.acs.org/doi/abs/10.1021/acs.jpcc.8b03948.

[33] Elizabeth Von Hauff. Impedance Spectroscopy for Emerging Photovoltaics. *The Journal of Physical Chemistry C*, 123(18):11329–11346, 2019.

[34] Monojit Bag, Lawrence A Renna, Ramesh Y Adhikari, Supravat Karak, Feng Liu, Paul M Lahti, Thomas P Russell, Mark T Tuominen, and D Venkataraman. Kinetics of ion transport in perovskite active layers and its implications for active layer stability. *Journal of the American Chemical Society*, 137(40):13130–13137, 2015.

[35] Mehmet C E M. *Advanced Electrical Characterization of Organic-Inorganic Hybrid Perovskite Solar Cells by Impedance Spectroscopy*. PhD thesis, Middle East Technical University, 2018.

[36] Bernard A Boukamp. A Linear Kronig-Kramers Transform Test for Immittance Data Validation. *Journal of The Electrochemical Society*, 142(6):1885, 1995. doi: 10.1149/1.2044210. URL https://doi.org/10.1149%2F1.2044210.

[37] M Schönleber, D Klotz, and E Ivers-Tiffée. A Method for Improving the Robustness of linear Kramers-Kronig Validity Tests. *Electrochimica Acta*, 131:20–27, 2014. ISSN 0013-4686. doi: https://doi.org/10.1016/j.electacta.2014.01.034. URL http://www.sciencedirect.com/science/article/pii/S0013468614001005.

[38] M Schönleber and E Ivers-Tiffée. Approximability of impedance spectra by RC elements and implications for impedance analysis. *Electrochemistry Communications*, 58:15–19, 2015. ISSN 1388-2481. doi: https://doi.org/10.1016/j.elecom.2015.05.018. URL http://www.sciencedirect.com/science/article/pii/S1388248115001502.

[39] Alexander R Pascoe, Noel W Duffy, Andrew D Scully, Fuzhi Huang, and Yi-Bing Cheng. Insights into Planar CH3NH3PbI3 Perovskite Solar Cells Using Impedance Spectroscopy. *The Journal of Physical Chemistry C*, 119(9):4444–4453, 3 2015. ISSN 1932-7447. doi: 10.1021/jp509896u. URL https://doi.org/10.1021/jp509896u.

[40] Didac Pitarch-Tena, Thi Tuyen Ngo, Marta Valles-Pelarda, Thierry Pauporte, and Ivan Mora-Sero. Impedance spectroscopy measurements in perovskite solar cells: device stability and noise reduction. *ACS Energy Letters*, 3(4):1044–1048, 2018.

[41] Jyoti Chaudhary, Shaily Choudhary, Chandra Mohan Singh Negi, Saral K Gupta, and Ajay Singh Verma. Electrical characterization of hybrid halide perovskites based heterojunction device. *Semiconductors*, 53(4):489–492, 2019.

[42] Wei Peng, Clara Aranda, Osman M Bakr, Germà Garcia-Belmonte, Juan Bisquert, and Antonio Guerrero. Quantification of ionic diffusion in lead halide perovskite single crystals. *ACS Energy Letters*, 3(7):1477–1481, 2018.

[43] Dominic W Ferdani, Samuel R Pering, Dibyajyoti Ghosh, Peter Kubiak, Alison B Walker, Simon E Lewis, Andrew L Johnson, Peter J Baker, M Saiful Islam, and Petra J Cameron. Partial cation substitution reduces iodide ion transport in lead iodide perovskite solar cells. *Energy Environ. Sci.*, 12(7):2264–2272, 2019. doi: 10.1039/C9EE00476A. URL http://dx.doi.org/10.1039/C9EE00476A.

[44] Dino Klotz, Ganbaatar Tumen-Ulzii, Chuanjiang Qin, Toshinori Matsushima, and Chihaya Adachi. Detecting and identifying reversible changes in perovskite solar cells by electrochemical impedance spectroscopy. *RSC Advances*, 9(57):33436–33445, 2019.

[45] Dino Klotz. Negative capacitance or inductive loop?–A general assessment of a common low frequency impedance feature. *Electrochemistry Communications*, 98:58–62, 2019.

[46] Hans-Rudolf Wenk and Andrey Bulakh. *Minerals: their constitution and origin*. Cambridge University Press, 2016.

[47] Masashi Ikegami, Jun Suzuki, Kenjiro Teshima, Masahide Kawaraya, and Tsutomu Miyasaka. Improvement in durability of flexible plastic dye-sensitized solar cell modules. *Solar Energy Materials and Solar Cells*, 93(6-7):836–839, 6 2009. ISSN 09270248. doi: 10.1016/j.solmat.2008.09.051.

[48] Haining Tian, Gerrit Boschloo, and Anders Hagfeldt. *Molecular devices for solar energy conversion and storage*. Springer, 2018.

[49] Efat Jokar, Cheng-Hsun Chien, Cheng-Min Tsai, Amir Fathi, and Eric Wei-Guang Diau. Robust Tin-Based Perovskite Solar Cells with Hybrid Organic Cations to Attain Efficiency Approaching 10%. *Advanced Materials*, 31(2):1804835, 1 2019. ISSN 09359648. doi: 10.1002/adma.201804835. URL http://doi.wiley.com/10.1002/adma.201804835.

[50] Zewen Xiao, Yuanyuan Zhou, Hideo Hosono, Toshio Kamiya, and Nitin P Padture. Bandgap Optimization of Perovskite Semiconductors for Photovoltaic Applications. *Chemistry – A European Journal*, 24(10):2305–2316, 2018. doi: 10.1002/chem.201705031. URL https://chemistry-europe.onlinelibrary.wiley.com/doi/abs/10.1002/chem.201705031.

[51] Erika Vega, Miguel Mollar, and Bernabé Marí. Effect of guanidinium on the optical properties and structure of the methylammonium lead halide perovskite. *Journal of Alloys and Compounds*, 739:1059–1064, 3 2018. ISSN 09258388. doi: 10.1016/j.jallcom.2017.12.177.

[52] Weihai Zhang, Juan Xiong, Jinhua Li, and Walid A. Daoud. Guanidinium induced phase separated perovskite layer for efficient and highly stable solar cells. *Journal of Materials Chemistry A*, 7(16):9486–9496, 2019. ISSN 20507496. doi: 10.1039/c9ta01893j. URL https://pubs.rsc.org/en/content/articlehtml/2019/ta/c9ta01893jhttps://pubs.rsc.org/en/content/articlelanding/2019/ta/c9ta01893j.

[53] Dominik J. Kubicki, Daniel Prochowicz, Albert Hofstetter, Marcin Saski, Pankaj Yadav, Dongqin Bi, Norman Pellet, Janusz Lewiński, Shaik M. Zakeeruddin, Michael Grätzel, and Lyndon Emsley. Formation of Stable Mixed Guanidinium-Methylammonium Phases with Exceptionally Long Carrier Lifetimes for High-Efficiency Lead Iodide-Based Perovskite Photovoltaics. *Journal of the American Chemical Society*, 140(9):3345–3351, 3 2018. ISSN 15205126. doi: 10.1021/jacs.7b12860. URL https://pubs.acs.org/doi/abs/10.1021/jacs.7b12860.

[54] Loreta A Muscarella, Eline M Hutter, Francesca Wittmann, Young Won Woo, Young-Kwang Jung, Lucie Mcgovern, Jan Versluis, Aron Walsh, Huib J Bakker, Bruno Ehrler, Corresponding Author, and B Ehrler@amolf Nl. Lattice compression increases the activation barrier for phase segregation in mixed-halide perovskites. Technical report, AMOLF, 2020.

[55] David P. McMeekin, Golnaz Sadoughi, Waqaas Rehman, Giles E. Eperon, Michael Saliba, Maximilian T. Hörantner, Amir Haghighirad, Nobuya Sakai, Lars Korte, Bernd Rech, Michael B. Johnston, Laura M. Herz, and Henry J. Snaith. A mixed-cation lead mixed-halide perovskite absorber for tandem solar cells. *Science*, 351(6269):151–155, 1 2016. ISSN 10959203. doi: 10.1126/science.aad5845. URL http://science.sciencemag.org/.

[56] Wei Geng, Le Zhang, Yan-Ning Zhang, Woon-Ming Lau, and Li-Min Liu. First-Principles Study of Lead Iodide Perovskite Tetragonal and Orthorhombic Phases for Photovoltaics. *The Journal of Physical Chemistry C*, 118(34):19565–19571, 8 2014. ISSN 1932-7447. doi: 10.1021/jp504951h. URL https://pubs.acs.org/doi/10.1021/jp504951h.

[57] Claudio Quarti, Edoardo Mosconi, James M. Ball, Valerio D'Innocenzo, Chen Tao, Sandeep Pathak, Henry J. Snaith, Annamaria Petrozza, and Filippo De Angelis. Structural and optical properties of methylammonium lead iodide across the tetragonal to cubic phase transition: Implications for perovskite solar cells. *Energy and Environmental Science*, 9(1):155–163, 1 2016. ISSN 17545706. doi: 10.1039/c5ee02925b.

[58] Riley E Brandt, Vladan Stevanović, David S Ginley, and Tonio Buonassisi. Identifying defect-tolerant semiconductors with high minority carrier lifetimes: Beyond hybrid lead halide perovskites. *arXiv preprint arXiv:1504.02144*, 2015.

[59] Ben Sudbury Keith McIntosh, Malcolm Abbott. The global standard spectrum (AM1-5g). URL https://www2.pvlighthouse.com.au/resources/courses/altermatt/The%20Solar%20Spectrum/The%20global%20standard%20spectrum%20(AM1-5g).aspx.

[60] Yasuhiro Yamada, Toru Nakamura, Masaru Endo, Atsushi Wakamiya, and Yoshihiko Kanemitsu. Near-band-edge optical responses of solution-processed organicinorganic hybrid perovskite CH3NH3PbI3on mesoporous TiO2electrodes. *Applied Physics Express*, 7(3):32302, 2 2014. doi: 10.7567/apex.7.032302. URL https://doi.org/10.7567%2Fapex.7.032302.

[61] Yuguo Tao. Screen-Printed Front Junction n-Type Silicon Solar Cells. In *Printed Electronics - Current Trends and Applications*. InTech, 9 2016. doi: 10.5772/63198.

[62] Alessandro Senocrate, Tolga Acartürk, Gee Yeong Kim, Rotraut Merkle, Ulrich Starke, Michael Grätzel, and Joachim Maier. Interaction of oxygen with halide perovskites. *Journal of Materials Chemistry A*, 6(23):10847–10855, 6 2018. ISSN 20507496. doi: 10.1039/c8ta04537b. URL https://pubs.rsc.org/en/content/articlehtml/2018/ta/c8ta04537bhttps://pubs.rsc.org/en/content/articlelanding/2018/ta/c8ta04537b.

[63] M. I. Asghar, J. Zhang, H. Wang, and P. D. Lund. Device stability of perovskite solar cells – A review, 9 2017. ISSN 18790690.

[64] Caleb C. Boyd, Rongrong Cheacharoen, Tomas Leijtens, and Michael D. McGehee. Understanding Degradation Mechanisms and Improving Stability of Perovskite Photovoltaics, 3 2019. ISSN 15206890. URL https://pubs.acs.org/doi/abs/10.1021/acs.chemrev.8b00336.

[65] Mary O'Kane. Perovskite solar cells: Causes of degradation. URL https://www.ossila.com/pages/perovskite-solar-cell-degradation-causes. Date accessed 29 September 2020.

[66] Wolfgang Tress. Metal Halide Perovskites as Mixed Electronic-Ionic Conductors: Challenges and Opportunities - From Hysteresis to Memristivity, 7 2017. ISSN 19487185. URL https://pubs.acs.org/doi/pdfplus/10.1021/acs.jpclett.7b00975.

[67] Arianna Marchioro, Joël Teuscher, Dennis Friedrich, Marinus Kunst, Roel van de Krol, Thomas Moehl, Michael Grätzel, and Jacques-E. Moser. Unravelling the mechanism of photoinduced charge transfer processes in lead iodide perovskite solar cells. *Nature Photonics*, 8(3):250–255, 3 2014. ISSN 1749-4885. doi: 10.1038/nphoton.2013.374. URL http://www.nature.com/articles/nphoton.2013.374.

[68] A. Pockett. *Characterization of Perovskite Solar Cells*. PhD thesis, University of Bath, 2016.

[69] Evgenij Barsoukov and J Ross Macdonald. *Impedance spectroscopy: theory, experiment, and applications*. John Wiley & Sons, 2018.

[70] Nikolaos Bonanos, Polycarpos Pissis, and J. Ross Macdonald. Impedance Spectroscopy of Dielectrics and Electronic Conductors. In *Characterization of Materials*, pages 1–14. John Wiley & Sons, Inc., Hoboken, NJ, USA, 6 2012. doi: 10.1002/0471266965.com121. URL http://doi.wiley.com/10.1002/0471266965.com121.

[71] Gergely F Samu, Csaba Janáky, and Prashant V Kamat. A Victim of Halide Ion Segregation. How Light Soaking Affects Solar Cell Performance of Mixed Halide Lead Perovskites. *ACS Energy Letters*, 2(8):1860–1861, 8 2017. doi: 10.1021/acsenergylett.7b00589. URL https://doi.org/10.1021/acsenergylett.7b00589.

[72] J Matthew Esteban. On the Application of the Kramers-Kronig Relations to Evaluate the Consistency of Electrochemical Impedance Data. *Journal of The Electrochemical Society*, 138 (1):67, 1991. doi: 10.1149/1.2085580. URL https://doi.org/10.1149%2F1.2085580.

[73] Matt Lacey. The kramers-kronig transform, Sep 2020. URL http://lacey.se/science/eis/kramers-kronig/. Date accessed 29 September 2020.

[74] M. Schönleber and E. Ivers-Tiffée. Publications - Lin-KK Tool, 2015. URL http://www.iam.kit.edu/wet/english/Lin-KK.php.

[75] Kashif Mairaj Deen. What is the acceptable value for chi square for well fitted impedance plots, 2018. URL https://www.researchgate.net/post/what_is_the_acceptable_value_for_chi_square_for_well_fitted_impedance_plots. Date accessed 29 September 2020.

[76] NOVA. Impedance Spectroscopy Tutorial. Technical report. URL https://www.ecochemie.nl/download/NovaTutorials/Impedance_measurements_tutorial.pdf.

[77] Elnaz Ghahremanirad, Agustín Bou, Saeed Olyaee, and Juan Bisquert. Inductive Loop in the Impedance Response of Perovskite Solar Cells Explained by Surface Polarization Model. *Journal of Physical Chemistry Letters*, 8(7):1402–1406, 4 2017. ISSN 19487185. doi: 10.1021/acs.jpclett.7b00415. URL https://pubs.acs.org/doi/full/10.1021/acs.jpclett.7b00415.

[78] Zhinst. 500 khz / 5 mhz impedance analyzer. URL https://www.zhinst.com/europe/products/mfia-impedance-analyzer. Date accessed 29 September 2020.

[79] Zhinst. MFIA User Manual. Technical report, Zurich Instruments, 2008.

[80] Heejae Lee, Sofia Gaiaschi, Patrick Chapon, Denis Tondelier, Jean Eric Bourée, Yvan Bonnassieux, Vincent Derycke, and Bernard Geffroy. Effect of Halide Ion Migration on the Electrical Properties of Methylammonium Lead Tri-Iodide Perovskite Solar Cells. *Journal of Physical Chemistry C*, 123(29):17728–17734, 7 2019. ISSN 19327455. doi: 10.1021/acs.jpcc.9b04662. URL https://pubs.acs.org/doi/pdf/10.1021/acs.jpcc.9b04662.

[81] F. A. Lindholm, J. G. Fossum, and E. L. Burgess. Application of the superposition principle to solar-cell analysis. *IEEE Transactions on Electron Devices*, 26(3):165–171, 1979.

[82] Philippe Holzhey and Michael Saliba. A full overview of international standards assessing the long-term stability of perovskite solar cells. *Journal of Materials Chemistry A*, 6(44):21794–21808, 2018.

[83] Eugen Zimmermann, Ka Kan Wong, Michael Müller, Hao Hu, Philipp Ehrenreich, Markus Kohlstädt, Uli Würfel, Simone Mastroianni, Gayathri Mathiazhagan, Andreas Hinsch, et al. Characterization of perovskite solar cells: Towards a reliable measurement protocol. *Apl Materials*, 4(9):091901, 2016.

[84] Eva Unger, Gopinath Paramasivam, and Antonio Abate. Perovskite solar cell performance assessment. *Journal of Physics: Energy*, 2(4):044002, 2020.

[85] Mark V Khenkin, Eugene A Katz, Antonio Abate, Giorgio Bardizza, Joseph J Berry, Christoph Brabec, Francesca Brunetti, Vladimir Bulović, Quinn Burlingame, Aldo Di Carlo, et al. Consensus statement for stability assessment and reporting for perovskite photovoltaics based on isos procedures. *Nature Energy*, 5(1):35–49, 2020.

[86] Dino Klotz, André Weber, and Ellen Ivers-Tiffée. Practical guidelines for reliable electrochemical characterization of solid oxide fuel cells. *Electrochimica Acta*, 227:110–126, 2017.

[87] Liu J, Wan TH, and Ciucci F. A Bayesian View on the Hilbert Transform and the Kramers-Kronig Transform of Electrochemical Impedance Data: Probabilistic Estimates and Quality Scores. *Electrochimica Acta*, 5 2020. doi: 10.26434/CHEMRXIV.12152529.V2. URL https://europepmc.org/article/PPR/PPR159193.

[88] Emilio Palomares, Núria F Montcada, María Méndez, Jesús Jiménez-López, Wenxing Yang, and Gerrit Boschloo. Photovoltage/photocurrent transient techniques. In *Characterization Techniques for Perovskite Solar Cell Materials*, pages 161–180. Elsevier, 2020.

[89] Zi Shuai Wang, Firouzeh Ebadi, Brian Carlsen, Wallace CH Choy, and Wolfgang Tress. Transient photovoltage measurements on perovskite solar cells with varied defect concentrations and inhomogeneous recombination rates. *Small Methods*, page 2000290, 2020.

[90] Sandheep Ravishankar, Clara Aranda, Sandy Sanchez, Juan Bisquert, Michael Saliba, and Germa Garcia-Belmonte. Perovskite solar cell modeling using light-and voltage-modulated techniques. *The Journal of Physical Chemistry C*, 123(11):6444–6449, 2019.

[91] Meysam Pazoki and Tomas Edvinsson. Time resolved photo-induced optical spectroscopy. In *Characterization Techniques for Perovskite Solar Cell Materials*, pages 139–160. Elsevier, 2020.

[92] Min-cheol Kim, So-Yeon Ham, Diyi Cheng, Thomas A Wynn, Hyun Suk Jung, and Ying Shirley Meng. Advanced characterization techniques for overcoming challenges of perovskite solar cell materials. *Advanced Energy Materials*, page 2001753, 2020.

[93] Anna Todinova, Lidia Contreras-Bernal, Manuel Salado, Shahzada Ahmad, Neftalí Morillo, Jesús Idígoras, and Juan A Anta. Towards a universal approach for the analysis of impedance spectra of perovskite solar cells: equivalent circuits and empirical analysis. *ChemElectroChem*, 4(11):2891–2901, 2017.

[94] Young-Hyun Song, Jin Sun Yoo, Eun Kyung Ji, Chul Woo Lee, Gill Sang Han, Hyun Suk Jung, and Dae-Ho Yoon. Design of water stable green-emitting ch3nh3pbbr3 perovskite luminescence materials with encapsulation for applications in optoelectronic device. *Chemical Engineering Journal*, 306:791 – 795, 2016. ISSN 1385-8947. doi: https://doi.org/10.1016/j.cej.2016.08.002. URL http://www.sciencedirect.com/science/article/pii/S1385894716310737.

[95] Michael Saliba, Juan-Pablo Correa-Baena, Christian M Wolff, Martin Stolterfoht, Nga Phung, Steve Albrecht, Dieter Neher, and Antonio Abate. How to make over 20% efficient perovskite solar cells in regular (n–i–p) and inverted (p–i–n) architectures. *Chemistry of Materials*, 30(13):4193–4201, 2018.

[96] Yehao Deng, Qi Wang, Yongbo Yuan, and Jinsong Huang. Vividly colorful hybrid perovskite solar cells by doctor-blade coating with perovskite photonic nanostructures. *Materials Horizons*, 2(6):578–583, 2015.

Appendix A

Sample Design and Fabrication

Sample design and fabrication constitutes of two parts. First in A.1, the experimental procedure to make the PSC samples actually used for data collection in this thesis (sample preparation and experimental procedure by Dr. Tom Macdonald, measurements by Mr. Richard Pacalaj), second in A.2 the experimental procedure and sample making carried out by me at AMOLF Institute for Atomic and Molecular Physics.

A.1 PSC samples from Imperial College London

Experimental procedure:
All devices were fabricated in a nitrogen filled glovebox. PTAA (Ossila, Inc.) at a concentration of 2mg/ml in toluene was deposited on the ITO by spin coating at 3000rpm for 20s. The PTAA layer was then dried in air for 5 minutes. The PFN solution (0.05 wt% in methanol, PFN purchased from 1-Material, Inc.) was spin casted on the substrate at 5000rpm for 30s to improve the wettability. The perovskite solution was spin-coated on the substrate at 4000rpm for 30s where at 7s, 0.5ml of diethyl ether was dripped on the substrate. The PCBM (Ossila. Inc) at 40mg in chlorobenzene was spin casted at 1500rpm for 30s on the perovskite layer. The BCP (Lumtec, Inc) in methanol (0.5mg/methanol) was deposited on the substrate by spin-coating at 4000rpm for 20s on substrate. At last, 3 nm of Cr and 80 nm of Au was evaporated on the substrate as top contact. The device performance was measured by J-V characteristic under Air Mass 1.5G global (AM 1.5G) illumination provided by an Xenon lamp. The light intensity was calibrated by silicon reference cell certificated by National Renewable Energy Laboratory (NREL).

A.2 Sample making and experimental work at AMOLF

Prior to measurements on the PSCs from Dr. Thomas Macdonald, samples were fabricated at AMOLF institute for physics of functional complex matter and several months of experimental work were carried out. Recipes were designed from combining work of PhD student Lucie Mcgovern with recipes from literature. Though the samples proved to be unstable, I learned a lot during this time on working with equipment, gloveboxes, handling chemicals, safety and working precision. Also I familiarised myself with measurement techniques as x-ray diffraction (XRD), Scanning Electron Microscopy (SEM), UV-Vis absorption and External Quantum Efficiency (EQE) measurements. After sample fabrication by me, PhD student Lucie Mcgovern kindly fabricated samples for this research project. However, the batch of PSCs she made proved to be unstable as well (PCE <1.9% for $MaPbI_3$). Impedance spectroscopy measurements on the unstable samples did not result in usable data for the research project. A summary from the experimental work is found below.

Experimental procedure:
Cleaning substrates
ITO substrates, pre-cut and etched are cleaned in five steps. 1) With soap in water and toothbrush 2) Ultrasonic bath with soap in water for 15minutes 3) Ultrasonic bath with water for 15minutes 4) Ultrasonic bath acetone for 15 minutes and 5) Ultrasonic bath with isopropanol for 15 minutes. The substrates are dried with nitrogen and plasma treatment is applied (just before spin-casting the hole transport layer).

Three fabrication methods/architectures and results

1. The first recipe is for PSCs with architecture ITO/PTAA/$MaPbBr_3$/C60/BCP/Au. 4.5mg of PTAA is dissolved in 3ml anhydrous toluene and stirred for 3hours in inert atmosphere. 60-80μL per 6.25cm^2 of the solution was spin-casted on the substrate with 6000rpm for 30s (acceleration of 2000rpm/s) and annealed at 100° Celsius for 10minutes in a glovebox filled with nitrogen. The sample was allowed to cool for 5minutes. Perovskite solution and spin-coating values were taken from the paper of Song et al. [94]. $MaBr$ and $PbBr_2$ precursors were mixed in a 1:1 mole ratio in a mixture of DMF & DMSO in 4:1 volume ratio. The solution was filtered using a 0.45μm PVDF LC 25mm Acrodisc and spin-coated with 2000rpm for 20s in the glovebox. Upon spin-casting and annealing it is observed that the perovskite does not attach to the PTAA layer (perovskite crystal is only present at the edges of the substrate where no PTAA is present). The recipe needs to be changed by either changing the surface roughness of the PTAA layer (by changing from ITO to FTO as transparent electrode) or by application of a PFN layer to increase the wettability of hydrophobic PTAA for the hydrophilic perovskite solution. Additionally, the spin-coating values may have been unsuitable for fabrication of a solar cell active layer with appropriate layer thickness. The evaporation step of the transport layers has been passed over, as the perovskite layer was not attached properly. See Figure A.1 for a schematics of the fabrication methods for perovskite and transport layers.

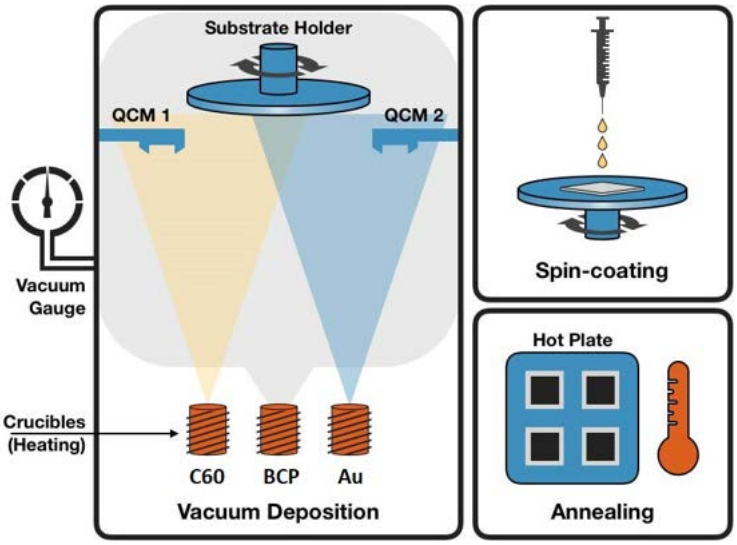

FIGURE A.1: Schematics of fabrication methods for perovskite and transport layers. Vacuum deposition/evaporation, spin-coating and annealing [35]. In the case of vacuum deposition, the sources are not heated at the same time but sequentially.

2. The second recipe uses Nickel Oxide (NiO) as HTL on ITO transparent electrode, $MaPbBr_3$ as perovskite, C60/BCP as ETL and Au as top electrode. A 0.3M solution is obtained after dissolving $Ni(NO_3)_2$ hexahydrate in pure ethanol in a nitrogen-filled glovebox. The solution is filtered with a 0.45μm PVDF LC25mm acrodisc. After plasma cleaning, 120 μL of the NiO solution is spin-casted on the substrate in ambient atmosphere at 4000rpm for 15s and directly after annealed at 150° Celsius for 25min. Then, the substrate with NiO layer is put in a furnace for 1hour at 350° Celsius with a 2h ramping of 3° Celsius/minute and a cooling time of 1h. The substrates were plasma-cleaned before application of the perovskite active layer. 152mg of $MaBr$ and 498.2mg of $PbBr_2$ were dissolved in pure ethanol to get a 40% weight solution of 1M. 200μL of the perovskite solution was spin-casted in a nitrogen-filled glovebox with 2000rpm for 15s, 30s, 45s and 60sec and directly afterwards annealed on a hotplate of 100° C for 10minutes. After storage in the glovebox for 1 night, 30nm of C60 and 8nm of BCP were evaporated on the substrate with 0.1Å/s. 100nm of gold was evaporated of the substrate at 0.8Å/s, of which the first 10nm at 0.1Å/s. Parameters from the NiO layer are from the work of PhD student Lucie Mcgovern and the perovskite and ETL parameters taken from the experimental procedure of the paper "How to make over 20% Efficient Perovskite Solar Cells in Regular (n–i–p) and Inverted (p–i–n) Architectures" from Saliba et al. [95].

   JV-characteristics were taken using a solar simulator and a reference cell to check for 100mW/cm^2 incident irradiation. First the dark and then the light characteristics were taken from -0.3V to 1.2V on three different scan speeds. The fastest scan speed was 181 steps of 0.02V using a 1ms wait time, the second speed of 361 steps of 0.01V of 1ms wait time and the slowest scan speed of 361 steps of 0.01V and 100ms wait time. PCE of the best pixels was about 1.7%. This was functional, as $MaPbBr_3$ using this recipe was expected to have an efficiency of 5%.

   Scanning Electron Microscopy (SEM) of the 60second spin-coated perovskite solution showed the perovskite layer did not contain pinholes, but was not densely packed (see Figure A.2).

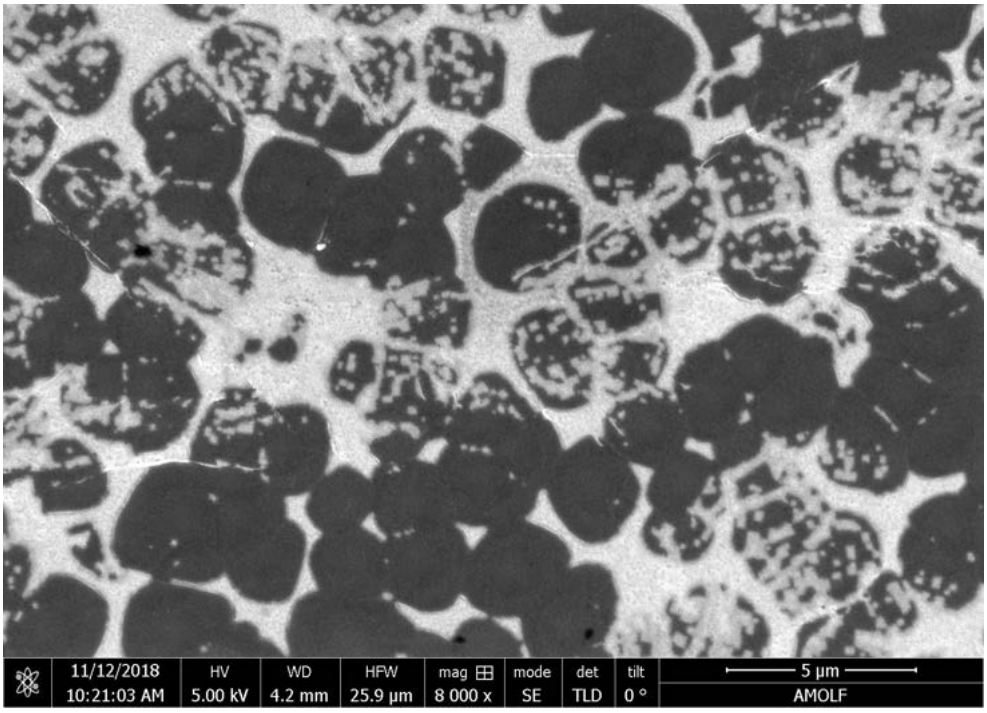

FIGURE A.2: Scanning electron microscopy image of perovskite layer deposited via spin-casting for 60seconds at 2000rpm.

SEM of the 15second spin-coated perovskite solution revealed a specific feature in the perovskite layer: concentric rings (Figure A.3a, A.3b). These rings have been documented in literature [96], speculating the concentric rings are caused by circulation of the perovskite solution, though a completely different fabrication technique was used there (see Figure A.3c).

Besides JV, also External Quantum Efficiency (EQE), UV-Vis absorption and XRD were measured. Results of this are not included. Impedance spectroscopy measurements on these samples were carried out as well, but proved to be too noisy for equivalent circuit modelling. The poor device functioning can be due to the perovskite solution which was not filtered before application, not concentrated enough, or due to a too low oxygen level during plasma-cleaning, leaving organic molecules present on the substrate. Another reason for bad results is likely to be that the solar cell was not contacted properly to the equipment, as the various solar cell layers at the top of the solar cell were not scratched away by a spatula to contact the bottom ITO electrode successfully.

3. The third recipe focuses on mixed halide PSCs, where the ratio between iodide and bromide is varied and applied on two different HTL's (PTAA and NiO). The NiO solution was prepared and applied as in the second recipe. Bromide/iodide perovskite stock solutions were prepared following the paper from Saliba [95]. Pure $MaPbI_3$ and $MaPbBr_3$ perovskite were produced, and mixed iodide/bromide $MaPbI_{20}Br_{80}$, $MaPbI_{40}Br_{60}$, $MaPbI_{60}Br_{40}$, $MaPbI_{80}Br_{20}$, $MaPbI_{85}Br_{15}$ as well. The perovskite solutions were filtered using a $0.2\mu m$ PTFE 13mm acrodisk filter. $20\mu L$ of the solutions was spin-coated on the PTAA or NiO substrate at 4000rpm for 30s with an acceleration of 2000rpm/s. 10s before the end, $100\mu L$ of chlorobenzene was applied on the center of the spinning substrate both fluently and mildly as to not cause a pinhole in the center. After, the samples are annealed at 100°C for 20-25minutes. See for a photo of the resulting perovskite layer in Figure A.4. Evaporation of the electron transport layers C60/BCP and the gold electrode was done using the parameters from the second recipe.

   Four different batches have been fabricated using this protocol. The first batch yielded solar cells of maximum 0.7%PCE. This was likely to be due to not accurate enough perovskite precursor solutions. During the second batch, not enough gold for the top electrode was present in the evaporator. The temperature rose, which could have burnt away the organic ETL, and the vaccuum had to be breached to insert more gold, which could have lead to contamination of the surface. No problems were encountered during fabrication of the third batch, however a problem occurred during transport of the samples (they were attached to the sample box using sticky tape, which proved to be impossible to get loose afterwards for all samples). Again no problems were encountered for the last batch, but still the samples did not work. This could have been due to ill calibrated pipettes leading to inaccurate precursor solutions or due to the use of old C60 as ETL. Another very likely cause to ill working samples is the combination of parameters from recipes for pure $MaPbI_3$ and pure $MaPbBr_3$ PSCs on various HTLs (NiO and PTAA). A recipe for perovskite solar cells takes several months to optimise, and combining recipes is therefore not a good idea to obtain working samples in a three month time-frame.

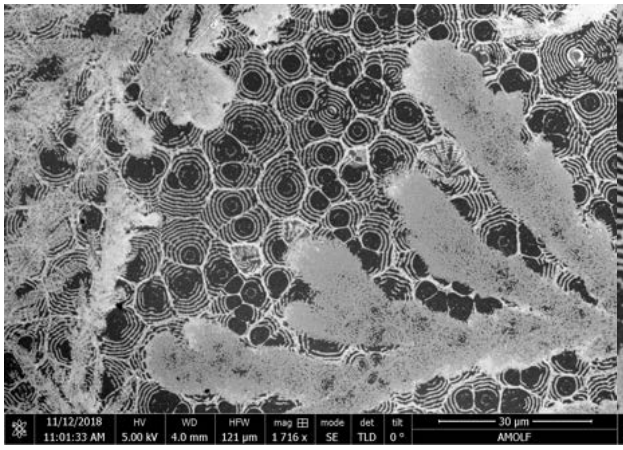

(A) Scanning electron microscopy image of perovskite layer deposited via spin-casting for 15seconds at 2000rpm.

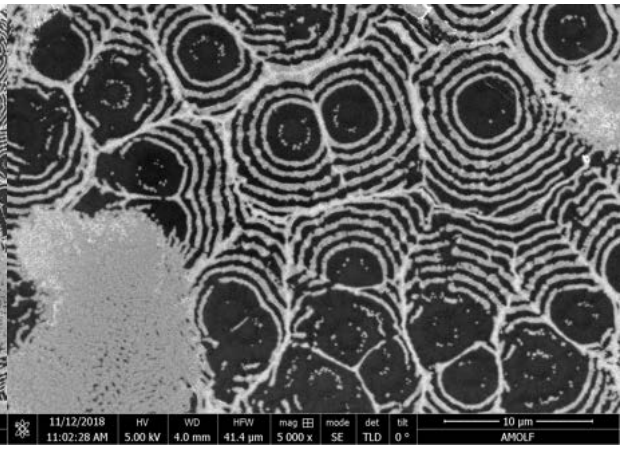

(B) Scanning electron microscopy image of perovskite layer deposited via spin-casting for 15seconds at 2000rpm at a smaller scale.

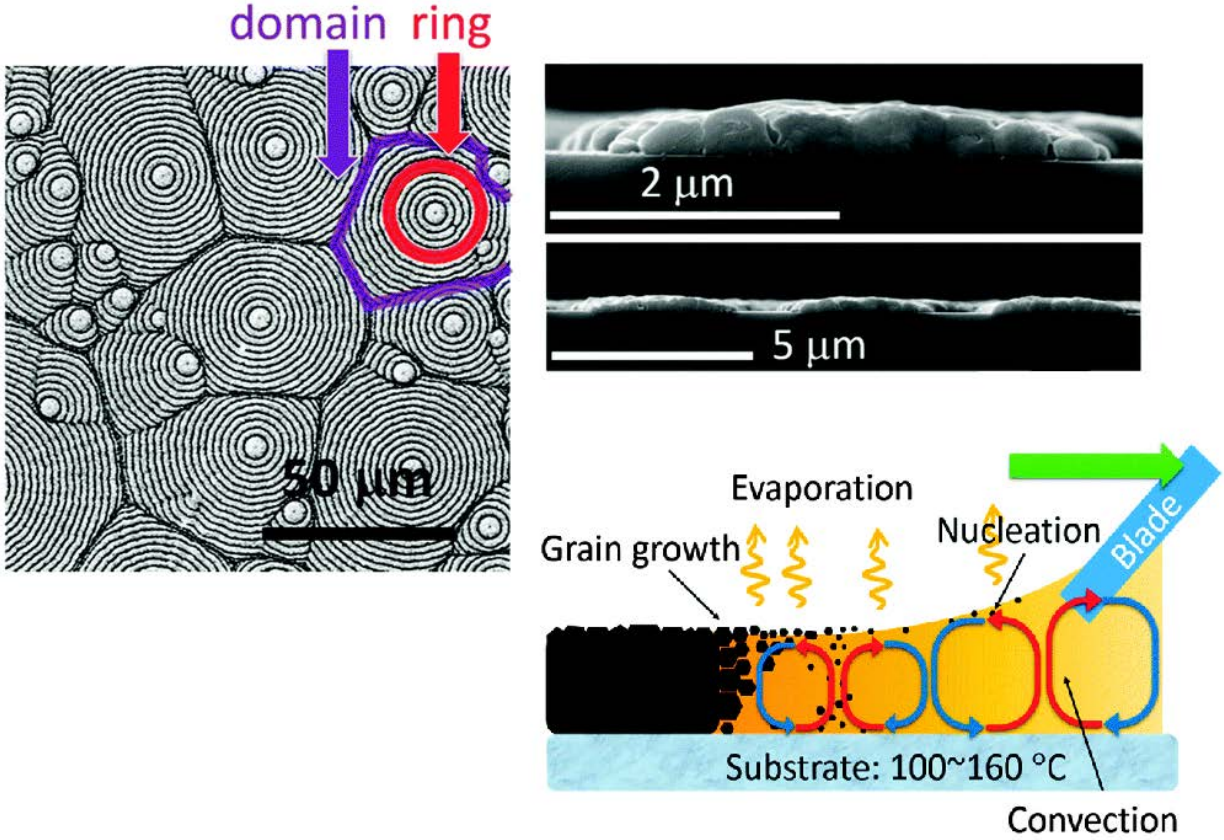

(C) SEM images from literature of perovskite layer deposited using doctor-blade coating, featuring concentric rings [96]. The ring structure can be formed by circulation of the perovskite solution during annealing, when the crystallisation of perovskite is in progress.

FIGURE A.3: Scanning electron microscopy images of the perovskite active layer displaying a specific feature: concentric rings (a, b). This phenomenon has been reported previously in literature using doctor-blade coating (c) [96].

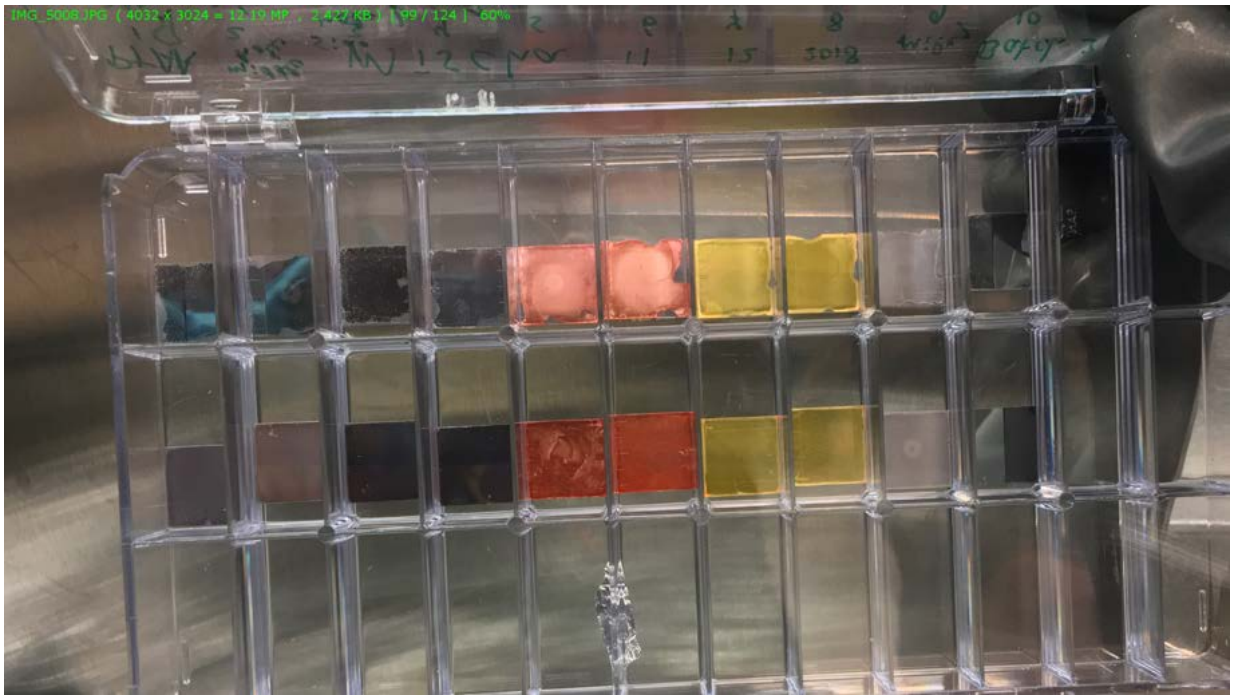

FIGURE A.4: Perovskite layers $MaPbI_3$, $MaPbBr_3$ and mixed $MaPbI_xBr_{1-x}$ in different ratio's (x = 0.2, 0.4, 0.6, 0.8). On the left: pure $MaPbI_3$, on the right: pure $MaPbBr_3$.

Appendix B

Kramers-Kronig relations experiments

B.1 KK example plots included with Lin-KK tool to guide compliance assessment

- Example 3: Valid Li-Ion Battery Spectrum (noisy situation)

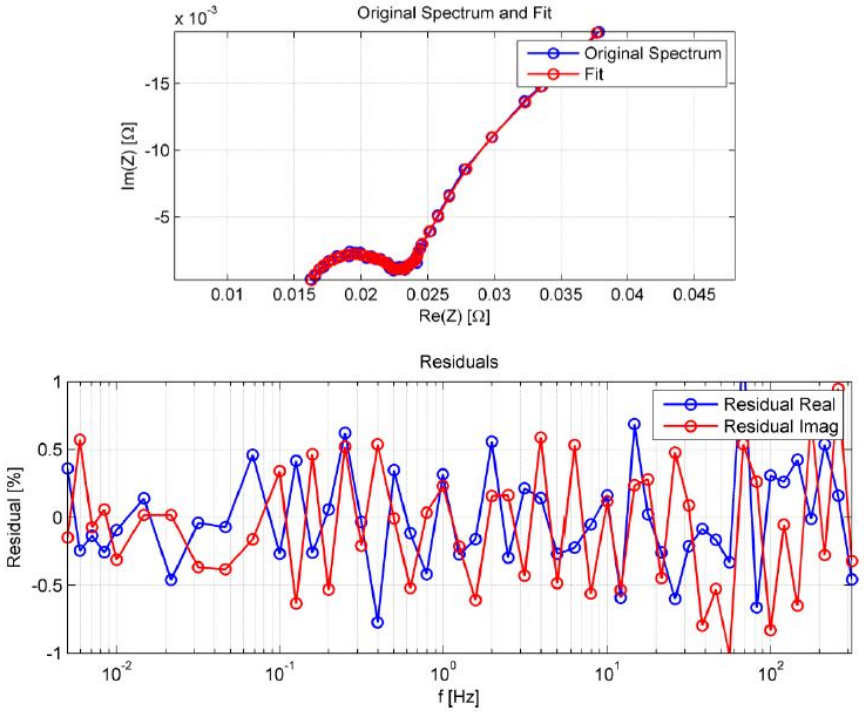

The residuals are bigger than in the first example, though do not display significant bias. Hence, the spectrum is of lower quality but is still KK-compliant.

- Example 4: Valid Li-Ion Battery Spectrum (outlier situation)

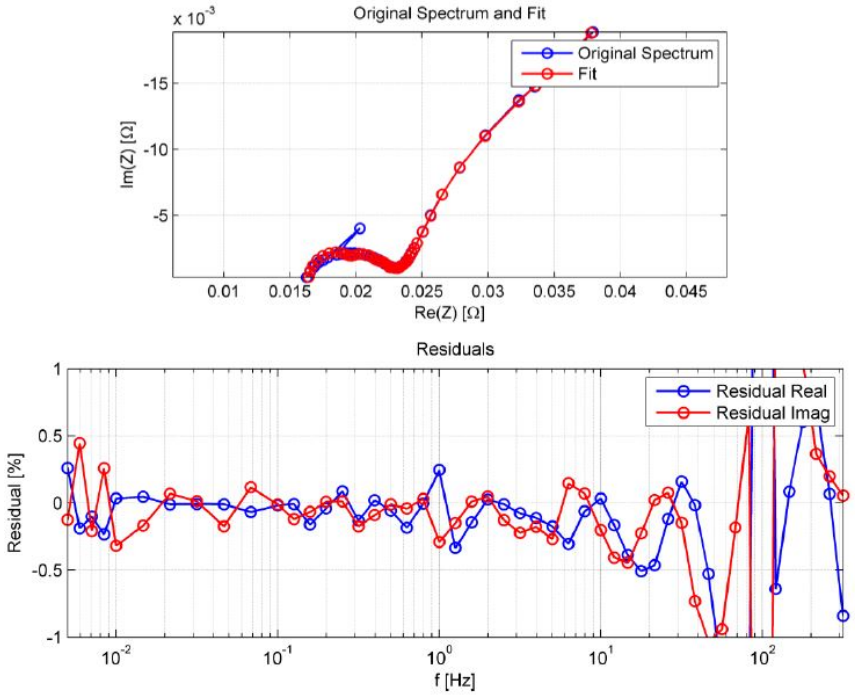

The measurement outlier at 100Hz, quite common for multiples of the power supply frequency, has increased the residuals over a broad frequency range. This is because the program tries to include the measurement point in the fit, at the cost of deviating from the data around the outlier datapoint. Thus the obtained residuals are bigger than they should be. The outlier datapoint thus has to be selected and deleted using the Lin-KK tool. This will result in the true residual spectrum shown below [74].

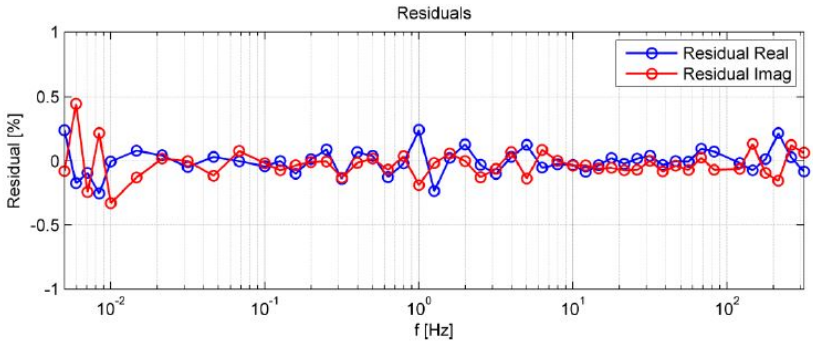

- Example 5: Invalid Li-Ion Battery Spectrum (time-variance)

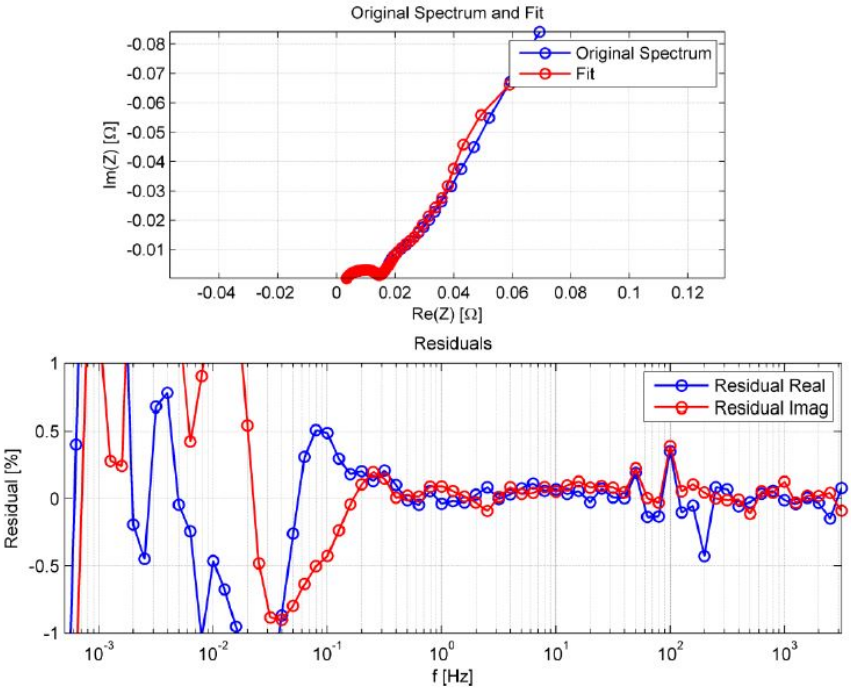

The residuals are greatly biased in the low frequency region. This indicates time-variance and therefore an KK-incompliant spectrum. In fact, the ambient temperature was purposely altered during the measurement. This shows up mainly in the low frequency region, as low frequencies take longer to measure than high frequencies and are therefore more prone to contain measurement noise or influence from external changes during the measurement [74].

- Example 6: Valid SOFC Spectrum

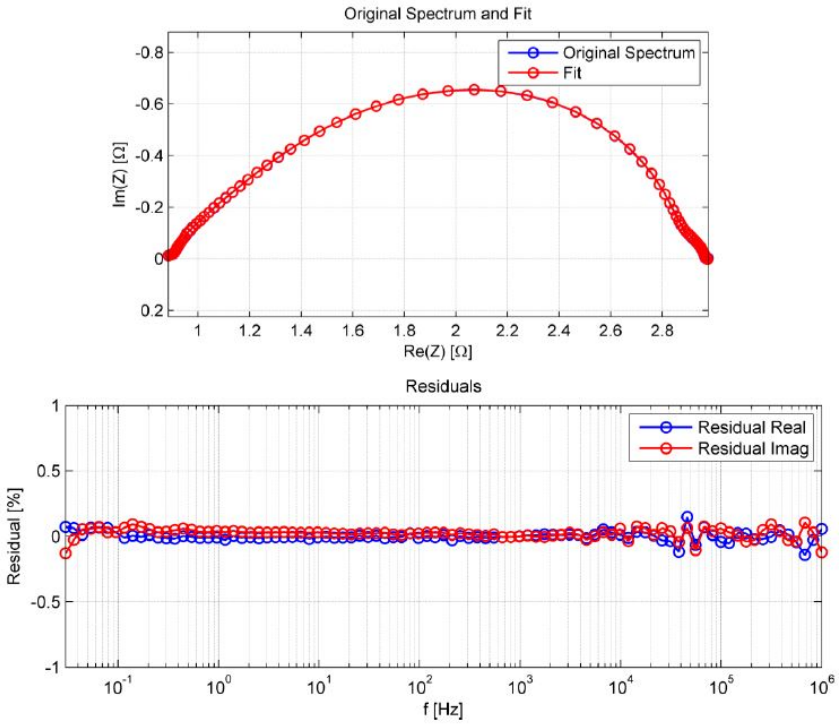

The residuals of this spectrum are small and show no systematic bias. Thus, this spectrum of this symmetric Anode-Anode Solid Oxygen Fuel Cell (SOFC) contains low-noise and describes a time-invariant system [74].

B.2 KK residual plots from experimental data

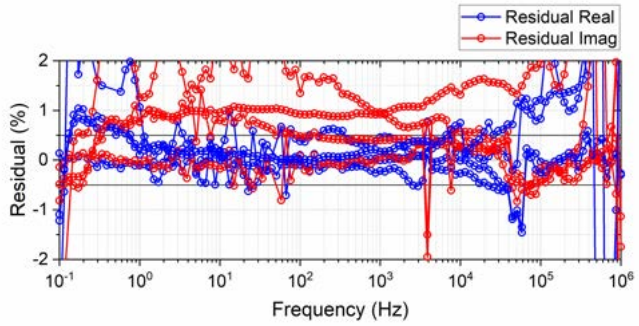

(A) Dark conditions KK-residuals plots of $MaPbI_3$-d103, bias voltages 0.7-1.0V

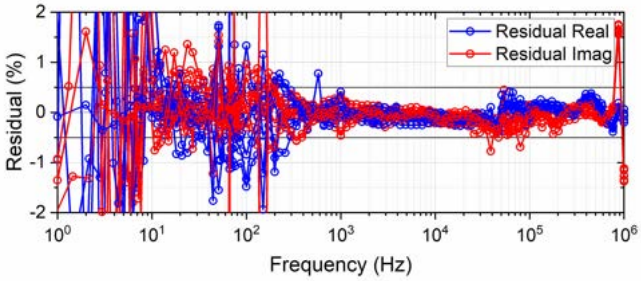

(B) Illumination condition KK-residuals plots of $MAPbI_3$-d103, bias voltages -0.2V, 0V, 0.2V and 0.7-1.1V.

FIGURE B.1: Kramers-Kronig residual plots for Impedance Spectroscopy data of $MAPbI_3$-d103 in dark (a) and illumination (b) condition. The data should present a straight line with no bias to be Kramers-Kronig compliant. Systematic bias is present for the bias voltages in the plots.

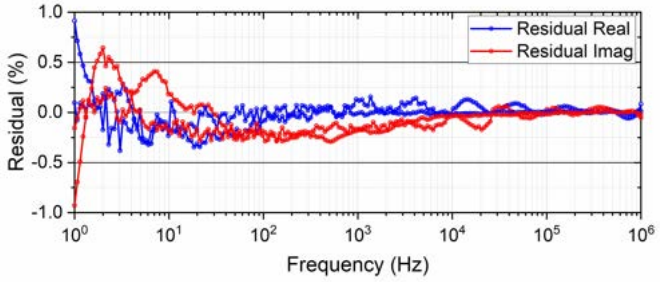

(A) Dark conditions KK-residuals plots of $MaPbI2$, bias voltages 0.8V and 0.9V.

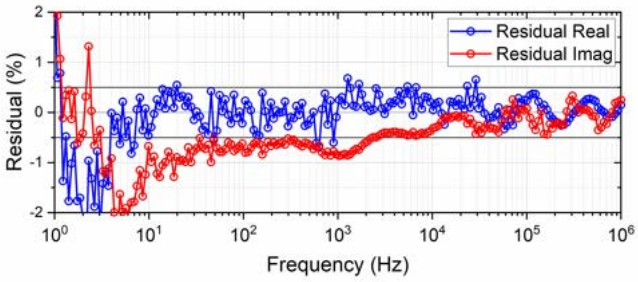

(B) Illumination condition KK-residuals plot of $MAPbI2$, bias voltage 0.9V.

FIGURE B.2: Kramers-Kronig residual plots for Impedance Spectroscopy data of $MAPbI2$ in dark (a) and illumination (b) condition. Systematic bias is present for the bias voltages in the plots.

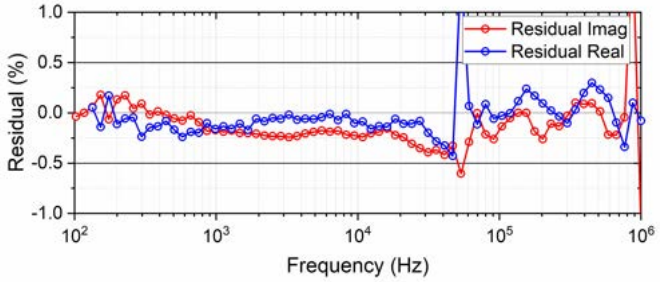

(A) KK-residuals plot of illuminated $MaPbI_3$-d103, bias voltage 0.5V on vertical scale of $\pm$ 1%. Systematic bias becomes apparent on this scale.

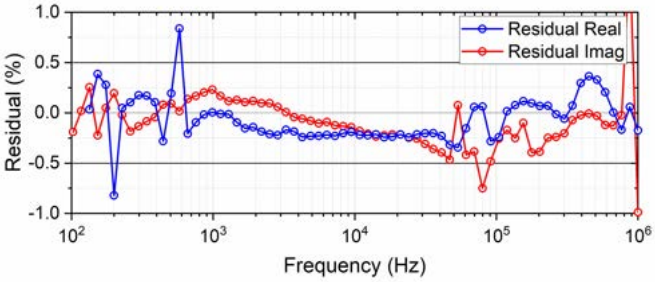

(B) KK-residuals plot of illuminated $MaPbI_3$-d103, bias voltage 0.7V on vertical scale of $\pm$ 1%. Systematic bias becomes apparent on this scale.

FIGURE B.3: Kramers-Kronig residual plots for Impedance Spectroscopy data of illuminated $MAPbI_3$-d103 for (a) 0.5V and (b) 0.7V on the frequency range of 10^6Hz to $100Hz$. Systematic bias is present for the bias voltages in the plots, whereas all other bias voltages are KK-compliant on this frequency range.

B.3 Conditions impacting KK-compliance

Qualitative analysis was carried out using the norms set by the example plots in section 2.3 on Kramers-Kronig relations in Impedance Spectroscopy. By categorising time-variance in magnitude by inserting "X" for strong time-variance (>0.4%) or "x" for weak time-variance (>0.2%) in the tables, the residual spectra can easily be checked for three potentially impacting variables on KK-compliance: *bias voltage, frequency region* and *illumination*. Consistency across repeated measurements is included for MAPI2. This leads to a better understanding of the conditions under which the impedance data is and is not Kramers-Kronig compliant. If a measurement is absent, a "-" is inserted in the table. The individual plots which are assessed are not included in the thesis, as this would lead to the inclusion of 76 individual Kramers-Kronig residual plots in the appendix. The individual Kramers-Kronig plots are available on request.

B.3.1 MAPI-d103

KK-analysis results for $MAPbI_3$-d103 under dark condition
In the tables below, the residual plots obtained by performing the Kramers-Kronig compliance test were assessed. The attributes *time-variance* and *level of noise* >2% of the residual plots were evaluated. High, mid and low frequencies are defined as $10^6 - 500Hz$, $500 - 10Hz$, $10 - 0.1Hz$ respectively.

TABLE B.1: **MAPI15_d103 DARK.** Presence of time-variance across High, Mid and Low Frequency Range (FR). "X" indicates strong time-variance (>0.4%), "x" indicates weak time-variance (>0.2%). When a cell is empty, this means no time-variance is present.

	-0.3V	-0.2V	-0.1V	0V	0.1V	0.2V	0.3V	0.4V	0.5V	0.6V	0.7V	0.8V	0.9V	1.0V	1.1V
High FR	-	X	X	-	X	X	-	X	X	X	X	noise	X	X	X
Mid FR	-		x	-		x	-				X	noise	X	X	
Low FR	-			-		X	-		x	x	X	noise	X	X	

TABLE B.2: Data outliers removed analysis of presence of time-variance across High, Mid and Low Frequency Range (FR). "X" indicates strong time-variance (>0.4%), "x" indicates weak time-variance (>0.2%). When a cell is empty, this means no time-variance is present.

	-0.3V	-0.2V	-0.1V	0V	0.1V	0.2V	0.3V	0.4V	0.5V	0.6V	0.7V	0.8V	0.9V	1.0V	1.1V
High FR	-	X	X	-	X	X	-	X	X	X	X	noise	X	X	X
Mid FR	-			-			-				X	noise	X	X	
Low FR	-			-		X	-		x	x	X	noise	X	X	

From comparing the tables above, it shows that in this case removing outlier datapoints only minimally leads to less time-variance in the residual spectra. Furthermore, we can observe that the high frequency range is always showing vast time-variance, and thus is KK-incompliant. The mid frequency range is incompliant more in the high bias voltages. The low frequency range is generally also incompliant at higher voltages. Not shown in the tables, but nonetheless investigated, is performing the analysis without the low frequency impedance data ($< 100Hz$). Here we see that deleting low frequency data does not influence mid or high frequency time-variance. These observations can be summarised by concluding that for $MAPbI_3$-d103 in the dark, removing outlier datapoints and low frequencies does not have an effect, and time-variance is mostly in the high frequencies.

KK-analysis results for $MAPbI_3$-d103 under illumination condition

In the tables below, the residual plots obtained by performing the Kramers-Kronig compliance test were assessed for PSC under illumination condition. The attributes time-variance and level of noise of the residual plots were evaluated. High, Mid and Low frequencies are defined as $10^6 - 500Hz$, $500 - 10Hz$, $10 - 0.1Hz$ respectively.

TABLE B.3: **MAPbI3-d103 LIGHT** analysis of presence of time-variance across High, Mid and Low Frequency Range (FR). "X" indicates strong time-variance (>0.4%), "x" indicates weak time-variance (>0.2%). When a cell is empty, this means no time-variance is present.

	-0.3V	**-0.2V**	**-0.1V**	**0V**	**0.1V**	**0.2V**	**0.3V**	**0.4V**	**0.5V**	**0.6V**	**0.7V**	**0.8V**	**0.9V**	**1.0V**	**1.1V**
High FR				X	-		-	x			x			X	X
Mid FR		x	x	X	-	x	-	X	x	x	X	x	x	X	X
Low FR	X	X	X	X	-	x	-	X	X	X	X	x		X	X

TABLE B.4: Data outliers removed analysis of presence of time-variance across High, Mid and Low Frequency Range (FR). "X" indicates strong time-variance (>0.4%), "x" indicates weak time-variance (>0.2%). When a cell is empty, this means no time-variance is present.

	-0.3V	**-0.2V**	**-0.1V**	**0V**	**0.1V**	**0.2V**	**0.3V**	**0.4V**	**0.5V**	**0.6V**	**0.7V**	**0.8V**	**0.9V**	**1.0V**	**1.1V**
High FR				X	-		-				x	x	X		X
Mid FR					-		-		x					X	noise
Low FR		x		noise	-	x	-				noise	noise	noise	noise	noise
	compliant		*compliant*					*compliant*		*compliant*					

From comparing the tables above, the following can be observed. Removing outlier datapoints has a big diminishing effect on the time-variance shown in the residual spectra, and leads to significantly more KK compliance in the mid and low frequency region. If data outliers are removed, a small voltage dependence becomes visible. Lower voltages are more often KK compliant.

In the table below, the results from the same analysis are presented for spectra cut at $100Hz$ to range $10^6 - 100Hz$.

TABLE B.5: Data outliers and low frequencies removed analysis of presence of time-variance across High, Mid and Low Frequency Range (FR). "X" indicates strong time-variance (>0.4%), "x" indicates weak time-variance (>0.2%). When a cell is empty, this means no time-variance is present.

	-0.3V	**-0.2V**	**0V**	**0.1V**	**0.2V**	**0.4V**	**0.5V**	**0.6V**	**0.7V**	**0.8V**	**0.9V**	**1.0V**	**1.1V**
High FR									X				
Mid FR							x						
	compliant	*compliant*	*compliant*	*compliant*	*compliant*	*compliant*		*compliant*		*compliant*	*compliant*	*compliant*	*compliant*

Only in two cases time-variance is present, for $0.5V$ and $0.7V$, and the rest of the residuals display a straight line without systematic bias and thus are compliant. This means that all the spectra of $MAPbI_3$-d103 under illumination, except $0.5V$ and $0.7V$, are compliant if outlier datapoints and low frequencies are removed. It curiously also means that deleting low frequency data leads to KK compliance in the high frequency region as well. These observations can be summarised by stating that both deleting outlier datapoints and removing low frequencies lead to more compliance, and low frequency time-variance influences high frequency residuals.

Summary of conditions under which the spectra are KK-compliant for $MaPbI_3$-d103
In the dark: spectra show less time-variance in mid- and low frequency range. In the light: spectra show more compliance when both outlier datapoints and low frequencies are removed.

B.3.2 MAPI2

KK-analysis results for $MAPI2$ under dark condition
In the tables below, the residual plots obtained by performing the Kramers-Kronig compliance test were assessed. The attributes *time-variance* and *level of noise* >2% of the residual plots were evaluated. High, Mid and Low frequencies are defined as $10^6 - 10^4 Hz$, $10^4 - 10^2 Hz$, $10^2 - 10^0 Hz$ respectively.

TABLE B.6: **MAPI2 DARK** analysis of presence of time-variance across High, Mid and Low Frequency Range (FR). "X" indicates strong time-variance (>0.4%), "x" indicates weak time-variance (>0.2%). When a cell is empty, this means no time-variance is present.

	0.7V	0.8V	0.9V	0.9V rpt1
High FR			x	
Mid FR		X	x	x
Low FR		x	x	X
	compliant			

TABLE B.7: Low frequencies <100Hz removed analysis of presence of time-variance across High, Mid and Low Frequency Range (FR). "X" indicates strong time-variance (>0.4%), "x" indicates weak time-variance (>0.2%). When a cell is empty, this means no time-variance is present.

	0.7V	0.8V	0.9V	0.9V rpt1	0.9V rpt2	0.9V rpt3
High FR					x	
Mid FR					x	
	compliant	*compliant*	*compliant*	*compliant*		*compliant*

From comparing the tables above, the following can be observed: removing low frequency data lead to more compliance and also influences high-frequency residuals. Additionally, repeated measurements at 0.9V shows some measurements are compliant whilst another is not.

KK-analysis results for $MAPI2$ under illumination condition

TABLE B.8: Full frequency range and low frequency removed analysis of presence of time-variance across High, Mid and Low Frequency Range (FR). "X" indicates strong time-variance (>0.4%), "x" indicates weak time-variance (>0.2%). When a cell is empty, this means no time-variance is present.

	0.0V 100Hz	0.7V 100Hz	0.9V 1Hz	0.9V cut 100Hz	0.9V 100Hz rpt
High FR					
Mid FR			X	X	
Low FR	-	-	X	-	-
	compliant	*compliant*			*compliant*

An important observation from this table is that 0.9V repeated measurement is compliant, whilst the cut spectrum of 0.9V to 100Hz is not compliant.

Summary of conditions under which the spectra are KK-compliant for $MaPI2$
IS spectra of MAPI2 are more often compliant for higher frequencies, and repeated measurements result in some cases in incompliance, and in some cases in compliance.

Appendix C

Demonstrations

KK-incompliant data can be fit
The spectrum below is incompliant, yet equivalent circuit modelling results in a good quality fit (see Figure C.1). The model is "Rs - R1Cpe1 - R2Cpe2" - by definition a KK-compliant model at all frequencies. The spectrum also shows a loop in the Nyquist plot, see figure C.3.

TABLE C.1: Fitting of incompliant impedance spectrum of MAPI2 0.9V Dark pixel 'Green' with two Equivalent Circuit Models. Fit is of sufficient quality if Chi-sqr is smaller than 0,001.

Model: Rs-R1C1-R2C2	**Chi-Sqr**	**Rs(+)**	**R1(+)**	**C1(+)**	**R2(+)**	**C2(+)**		
MAPI 0.9V Dark	**0,0016043**	38,23	4866	2,87E-09	1176	1,60E-05		
Model: Rs-R1Cpe1-R2Cpe2	**Chi-Sqr**	**Rs(+)**	**R1(+)**	**CPE1-T(+)**	**CPE1-P(+)**	**R2(+)**	**CPE2-T(+)**	**CPE2-P(+)**
MAPI 0.9V Dark	**0,00025548**	33,07	4900	3,6586E-09	0,98137	1189	1,9454E-05	0,96594

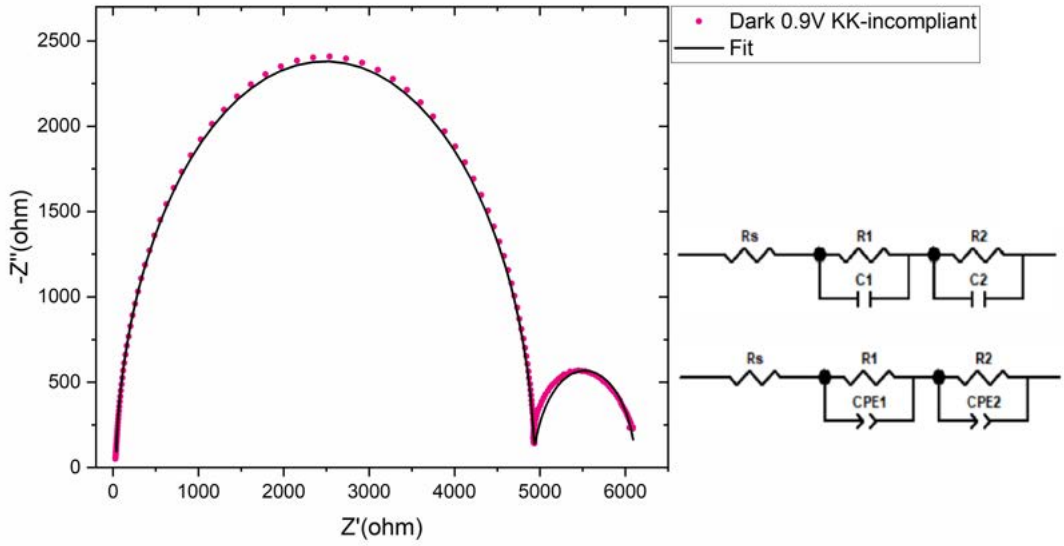

FIGURE C.1: KK-incompliant data can be fit with a KK-compliant equivalent circuit model (Rs-R1Cpe1-R2Cpe2) and result in good quality of fit.

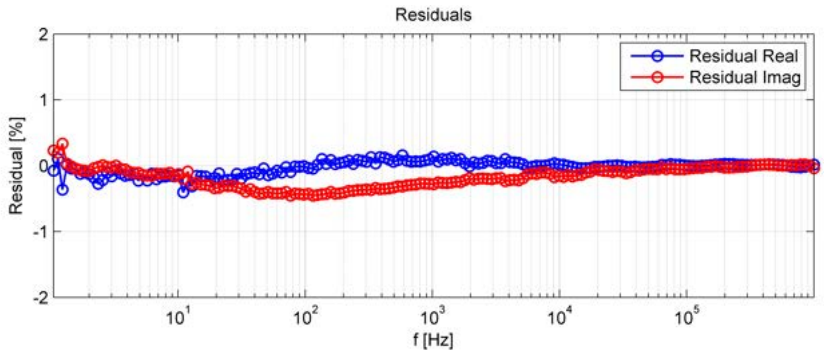

FIGURE C.2: KK-residual plot of MAPI2 Dark pixel 'Green' displaying clear time-variance by biased residuals in the mid-frequency range.

Spectra with mid-frequency loop in the Nyquist plots shows clear mid-frequency time-variance MAPI at 0.9V bias under dark conditions. Frequency range 1MHz - 1Hz. The second (bottom) spectrum is taken 15 minutes after the first (top) spectrum (see Figure C.3). The bottom spectrum can also be fit with ECM and result in a good quality of fit, though it is an KK incompliant spectrum. See Figure C.1.

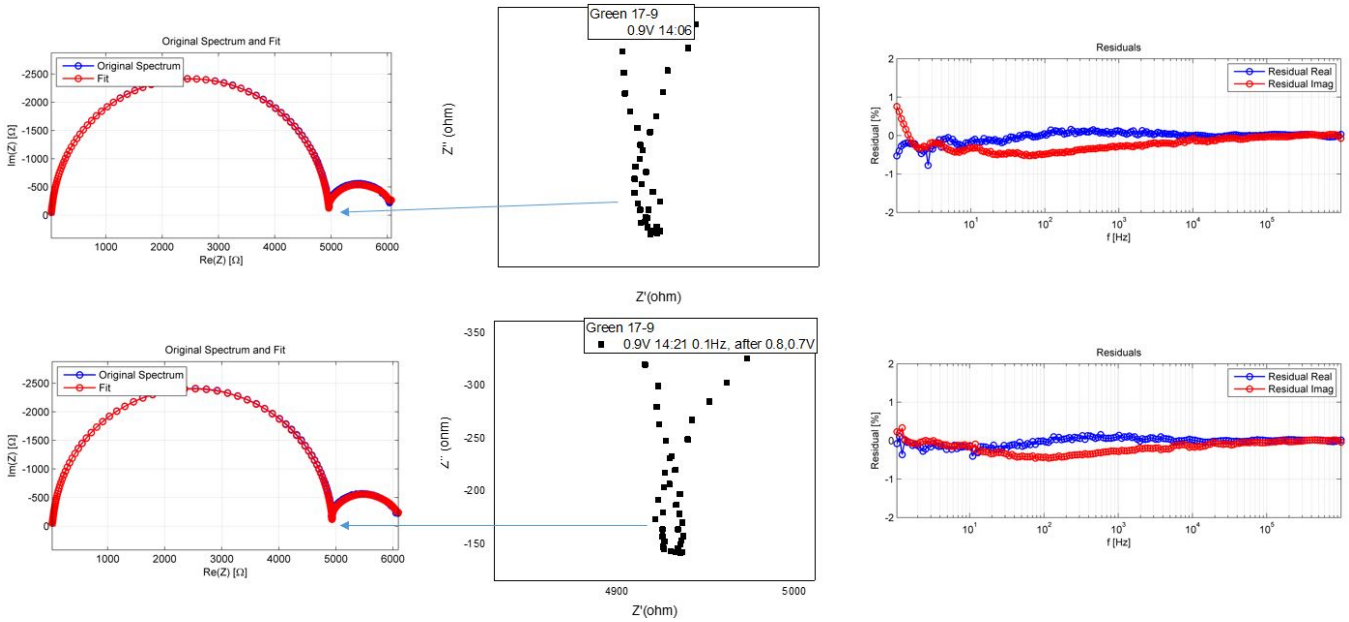

FIGURE C.3: Spectra showing both a loop in the Nyquist plot and mid-frequency time-variance in the KK-residuals.

Warburg mass transport is compliant in the frequency range 10^6Hz to 1Hz
Below a spectrum from MAPI2 under illumination condition at 0V from 10^6Hz to 100Hz is fit with a simple Randles model plus added linear Warburg-open element. Then, the Warburg tail is simulated to 1Hz and the KK-compliance assessed with the Lin-KK tool. The simulated Warburg tool is KK-compliant over the frequency range of 10^6Hz to 1Hz. Therefore, the Warburg-open element is not time-dependent in this frequency region.

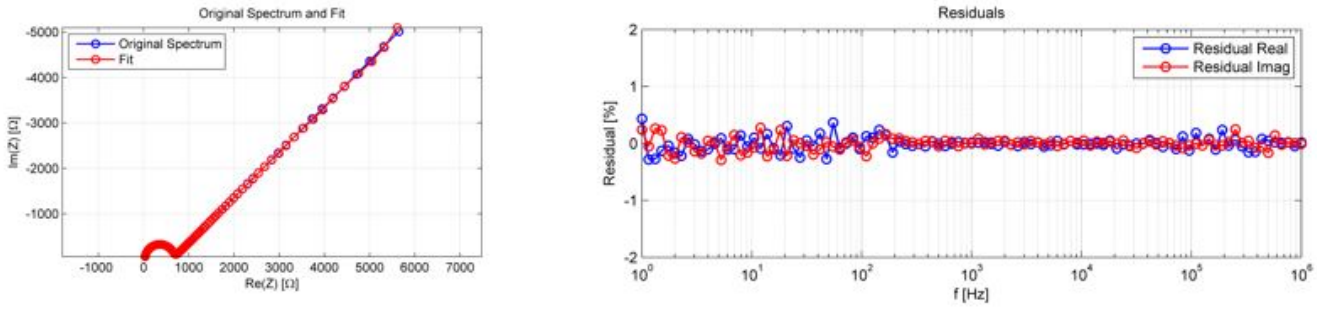

FIGURE C.4: Simulated warburg tail to 1Hz based on a spectrum of MAPI2 0V under illumination condition measured to 100Hz. No time-variance is shown and the residuals stay within the 0.5 border, leading to KK compliance of the Warburg-open element on the frequency range of 10^6Hz to 1Hz.

Silicon based reference solar cell shows one semi-circle in the Nyquist plot at dark 0V

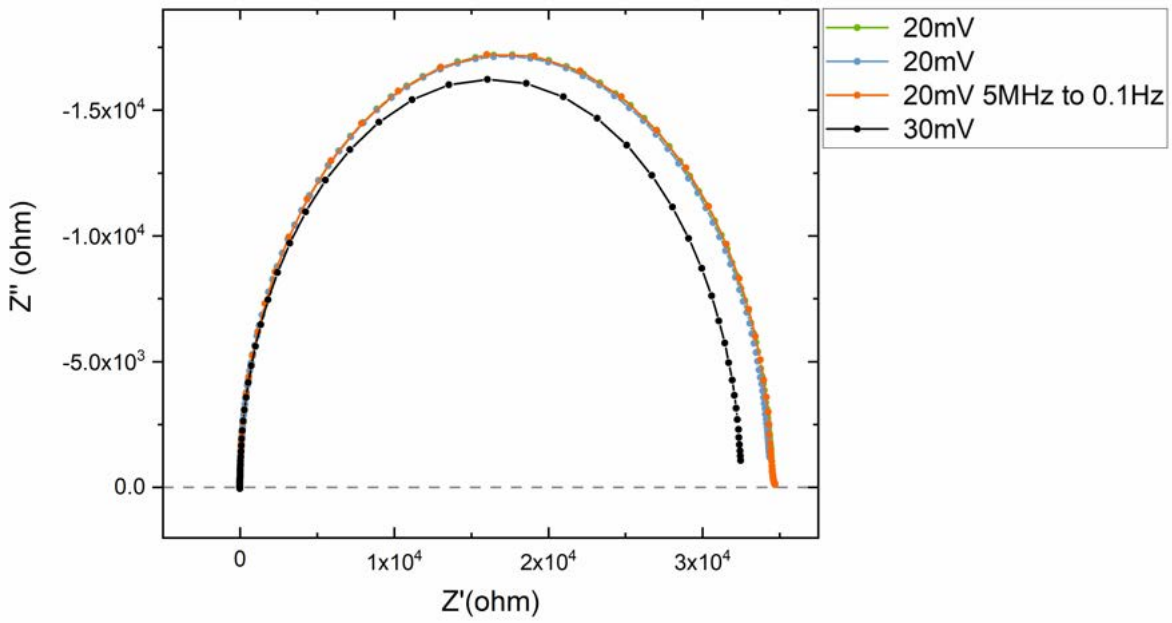

FIGURE C.5: Impedance measurement of silicon based reference solar cell at both 20mV and 30mV V_{ac} perturbation signal in the dark at 0V bias. Measurements were carried out using 200datapoints on a logarithmic scale in frequency on a range of 5MHz to 1Hz. One of the measurements at 20mV V_{ac} has been carried out unto 0.1Hz. The measurement at 30mV V_{AC} was not taken in the linear (Ohmic) regime of the solar cell, since the measurement result is not the same as when measured at a smaller excitation signal of 20mV.

Appendix D

Mixed cation perovskites

Apart from pure $MAPbI_3$ solar cells, also two multi-cation perovskite solar cells have been measured. The cells both have 5% added of respectively Guanidinium (GA) and Formamindium (FA) added in the $MaPbI_3$ precursor solutions. The solar cell parameters and JV-curves are presented below.

D.1 Solar cell performance

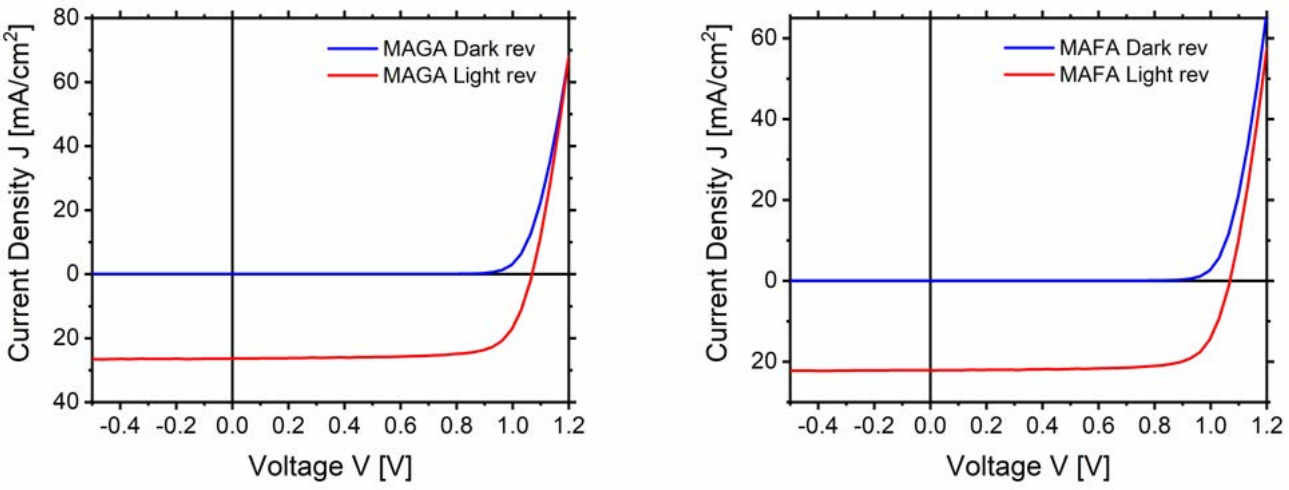

(A) *MAGA* (B) *MAFA*

FIGURE D.1: Current-voltage characteristics of multi cation perovskite solar cells $Ma_{0.95}Ga_{0.05}PbI_3$ and $Ma_{0.95}Fa_{0.05}PbI_3$ (*MAGA* and *MAFA*) under dark and under illumination condition.

TABLE D.1: Solar cell performance parameters of the two multi-cation devices MAGA and MAFA. The devices show similar performance.

Device	Jsc (mA/cm2)	Voc (V)	FF	MPP (V)	PCE (%)
MAGA	23.1	1.06	0.79	0.89	19.3
MAFA	23.0	1.07	0.76	0.86	19.1

D.2 IS data representation and equivalent circuit modelling

Below, the impedance data of $MAGA$ and $MAFA$ is compared to each other. The impedance data of $MAPI2$ is added as reference and representative for the pure $MaPbI_3$ cells, to allow for comparison of mixed cation perovskites with pure $MaPbI_3$. See Figure 4.1d and Table 4.1 for the solar cell performance of $MAPI2$. First, the impedance data in the dark will be presented and analysed, then the impedance data under illumination will be discussed.

Dark condition

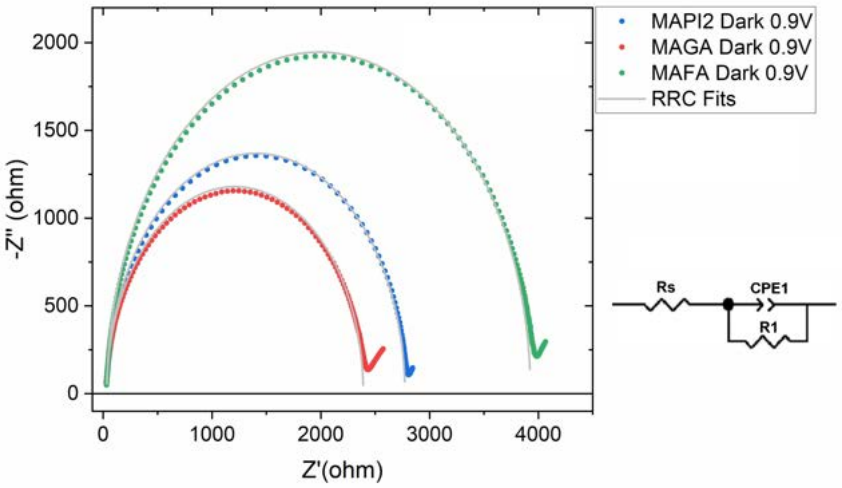

FIGURE D.2: Comparison of Nyquist plots of mixed cation perovskite solar cells MAGA and MAFA in the dark at 0.9V bias voltage, with MAPI2 0.9V as reference. Frequency range is from $10^6 Hz$ to $100 Hz$.

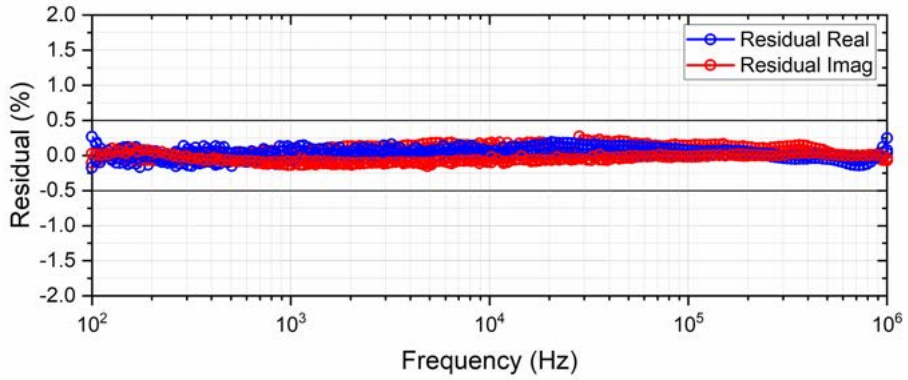

FIGURE D.3: Kramers-Kronig residual plots of impedance spectra of MAGA, MAFA and MAPI2 at 0.9V under dark conditions. The residuals lie within the 0.5% border and show no apparent systematic bias, and the spectra are evaluated KK-compliant.

TABLE D.2: Fitting of spectra taken in the dark at 0.9V of MAGA, MAFA, MAPI2 with a Randles model containing a constant phase element (CPE). Only the chi-squared value of the fit of MAGA is smaller than 10^{-3}, indicating a fit of sufficient quality with this circuit model.

	Chi-sqr	**Rs (Ω)**	**CPE1-T (F)**	**CPE1-P**	**R1 (Ω)**
MAGA	0,000742	27,96	3,26E-09	0,98709	2380
MAFA	*0,001047*	*31,98*	*3,26E-09*	*0,9912*	*3919*
MAPI2	*0,001045*	*32,35*	*3,14E-09*	*0,99148*	*2755*

Illumination condition

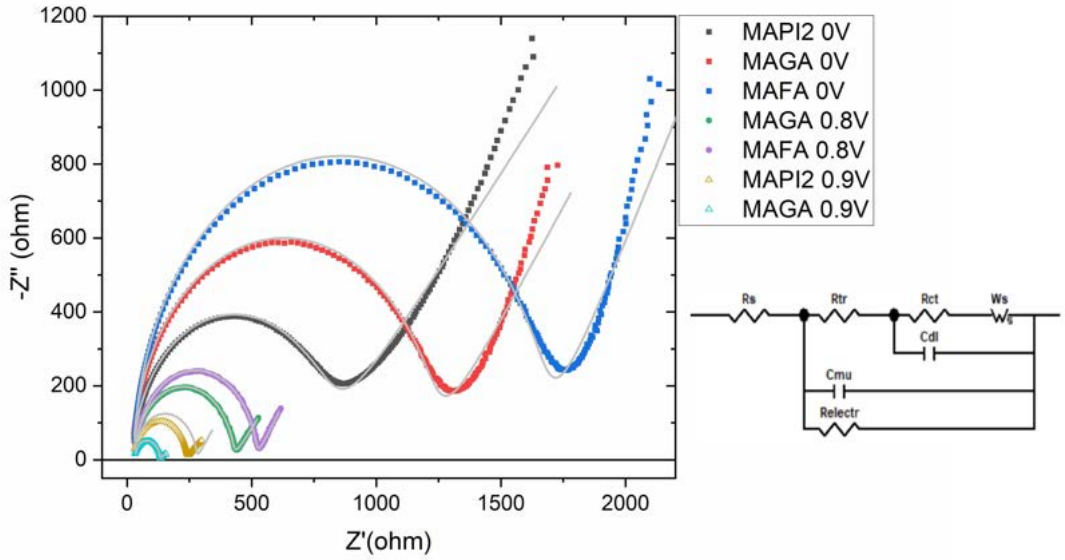

FIGURE D.4: Comparison of Nyquist plots of mixed cation perovskite solar cells MAGA and MAFA under illumination at 0, 0.8V and 0.9V bias voltage, with MAPI as reference. Frequency range is from $10^6 Hz$ to $100 Hz$.

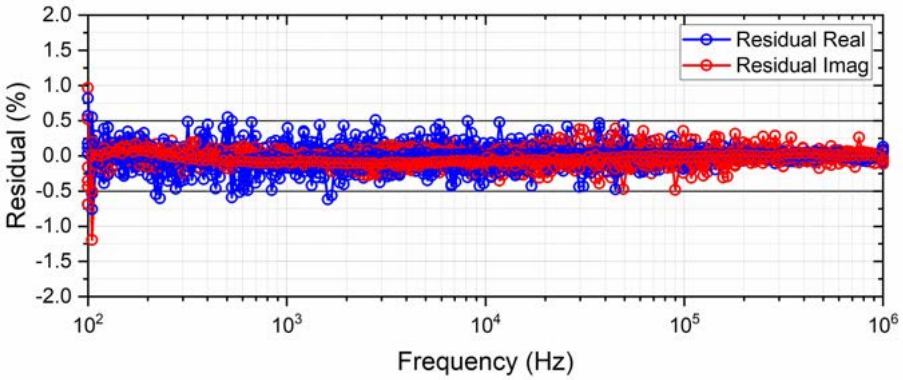

FIGURE D.5: Kramers-Kronig residual plots of impedance spectra of MAGA, MAFA and MAPI2 at 0V, 0.8V and 0.9V bias under illumination conditions. The residuals lie within the 0.5% border and the Residual Real en Residual Imaginary for every individual spectrum show no apparent systematic bias. The spectra are evaluated KK-compliant.

The spectra were fit with the fitting model described in Figure 2.16c. The fitting model has physical parameters attributed to the components which are described in the caption of the before mentioned Figure. The fits are of sufficient quality, though negative values for R_{tr} and C_{μ} are physically not expected.

TABLE D.3: Fitting values from fitting the spectra of MAGA, MAPI2 and MAFA under illumination at 0.9V, 0.8V and 0V bias to the model of 2.16c. Large differences are shown for R_{ct}, $Ws - T$ and R_{electr} between cells and per bias voltage.

	Chi-Sqr	**Rs (Ω)**	**Rtr (Ω)**	**Rct (Ω)**	**Ws-R**	**Ws-T**	**Ws-P**	**Cdl (F)**	**Cμ (F)**	**R$_{electr}$ (Ω)**
MAPI2 0.9V	0,000196	17763	-17733	251	7,68E+04	184	0,5653	4,06E-09	-4,72E-15	8,42E+07
MAGA 0.9V	*0,001059*	*43,43*	*-3,26E-05*	*87,23*	*44,66*	*0,004513*	*0,43136*	*-5,01E-06*	*5,02E-06*	*2,13E+18*
MAGA 0.8V	0,000122	17762	-17734	394,2	7,09E+04	192,1	0,5261	3,07E-09	-2,90E-15	1,36E+13
MAFA 0.8V	0,000175	17763	-17732	484,2	1,19E+05	100,2	0,59631	3,16E-09	-4,48E-15	8,58E+09
MAPI2 0V	0,000544	17422	-17394	754,2	1,22E+05	8,608	0,51841	2,57E-09	-4,78E-15	1,38E+08
MAGA 0V	0,000608	17452	-17363	1176	1,30E+05	9,026	0,57033	2,27E-09	-3,37E-15	4,73E+06
MAFA 0V	0,000602	17555	-17263	1587	2,37E+05	5,551	0,65882	2,49E-09	-4,84E-15	1,15E+06

Appendix E

Accuracy chart of MFIA Impedance Analyser

The MFIA Impedance Analyser from Zurich Instruments is delivered with an accuracy chart for impedance measurements. The measurements performed on $MaPbI_3$ device fall within 0.05% accuracy, except for frequencies from $6{\cdot}10^4$Hz to 10^6Hz. Here the accuracy is 0.1 to 1%. See the black polygon in Figure E.1, based on measurements of $MaPbI_3$ using a 20mV excitation signal under dark/illumination conditions from 0V-0.9V DC bias voltage.

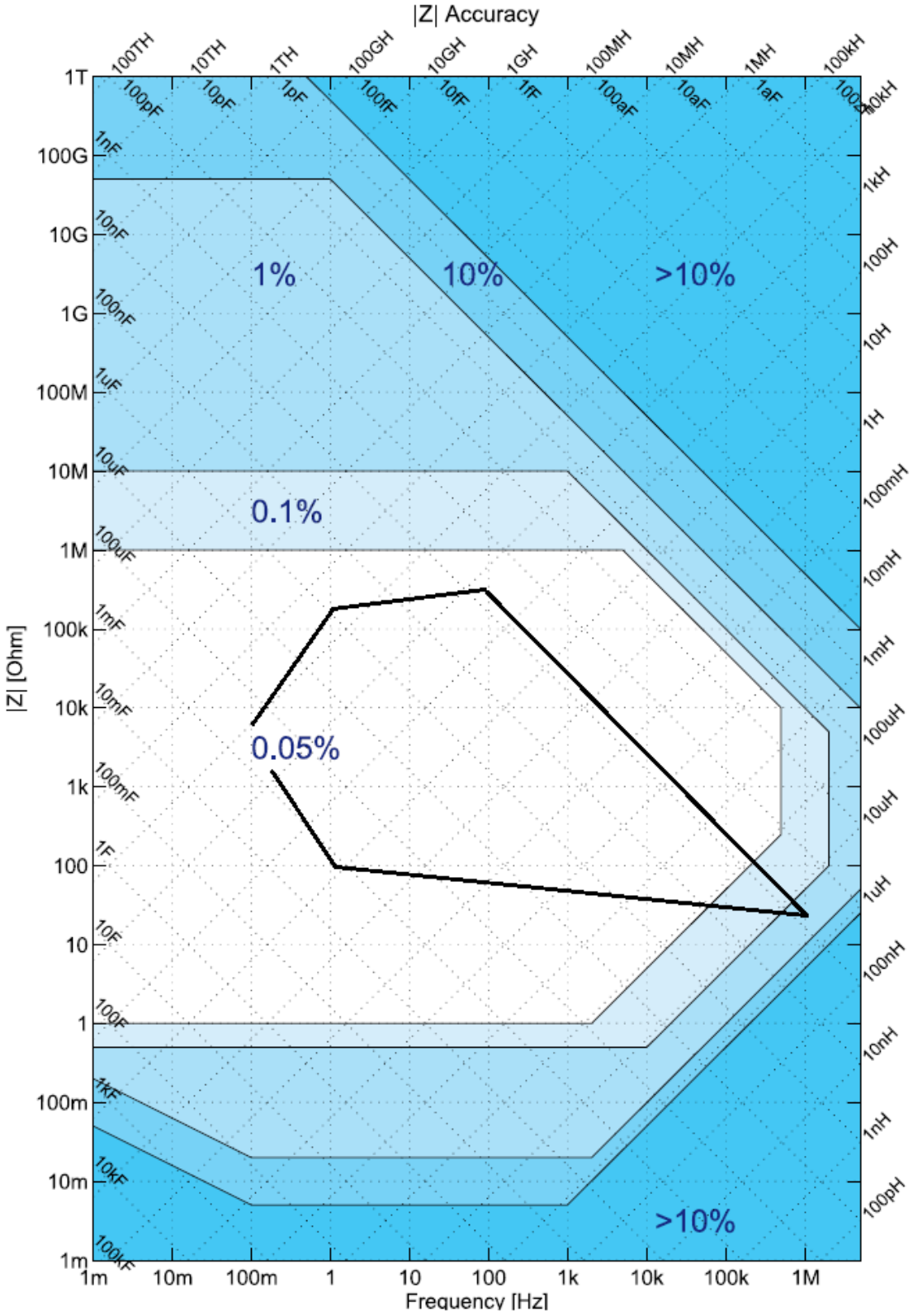

FIGURE E.1: MFIA Impedance Analyser accuracy chart [78]. The black polygon indicates the |Z| values for measurements on a $MaPbI_3$ perovskite solar cell using a 20mV excitation signal under dark/illumination conditions from 0V-0.9V DC bias voltage.